

# **Growth and Characterization of NiMnSb-based Heterostructures**

Dissertation zur Erlangung des  
naturwissenschaftlichen Doktorgrades der  
Bayerischen Julius-Maximilians-Universität  
Würzburg

vorgelegt von  
PETER BACH  
aus Tauberbischofsheim

Würzburg  
Februar 2006

Eingereicht am:

bei der Fakultät für Physik und Astronomie

1. Gutachter: Prof. L.W. Molenkamp
2. Gutachter: Prof. R. Neder

1. Prüfer: Prof. L.W. Molenkamp
2. Prüfer: Prof. R. Neder
3. Prüfer: Prof. R. Oppermann

Tag der mündlichen Prüfung: 05.05.2006

Doktorurkunde ausgehändigt am:

# Contents

<b>1</b>	<b>Introduction</b>	<b>1</b>
<b>2</b>	<b>Heusler Compounds</b>	<b>3</b>
2.1	Historical Overview . . . . .	3
2.2	Properties of NiMnSb . . . . .	4
<b>3</b>	<b>Basic Physical and Technological Principles</b>	<b>9</b>
3.1	Molecular Beam Epitaxy . . . . .	9
3.1.1	Principles of MBE . . . . .	9
3.1.2	MBE Setup . . . . .	11
3.2	X-Ray Diffraction . . . . .	13
3.2.1	Reciprocal Space Maps . . . . .	14
3.2.2	Thickness Fringes . . . . .	17
3.2.3	Intensity of Reflections . . . . .	18
3.3	Reflective High Energy Electron Diffraction . . . . .	21
3.3.1	RHEED Oscillations . . . . .	23
<b>4</b>	<b>Growth of NiMnSb on (001) Oriented Materials</b>	<b>25</b>
4.1	Substrate and Buffer Materials . . . . .	25
4.2	Substrate Preparation . . . . .	25
4.3	Growth (In,Ga)As on InP(001) . . . . .	26
4.4	Growth of NiMnSb on InP(001) . . . . .	31
4.4.1	Flux Ratios . . . . .	33
4.4.2	Substrate Temperature . . . . .	37
<b>5</b>	<b>Structural Properties of NiMnSb (001)</b>	<b>41</b>
5.1	Surface Properties . . . . .	41
5.1.1	RHEED Oscillations . . . . .	41
5.1.2	Spot Profile Analysis of Low-Energy Electron Diffraction . . . . .	43
5.1.3	HRXRD Thickness Fringes . . . . .	43
5.2	Crystalline Properties . . . . .	46

5.2.1	Relaxation in NiMnSb Layers . . . . .	46
5.2.2	Crystalline Defects in NiMnSb . . . . .	52
<b>6</b>	<b>Magnetic Properties of NiMnSb(001)</b>	<b>61</b>
6.1	Magnetic Anisotropies . . . . .	63
6.2	Magnetic Damping . . . . .	66
6.3	Hysteresis Curves . . . . .	69
6.4	Exchange Bias in NiMnSb/NiMn Bilayers . . . . .	71
<b>7</b>	<b>NiMnSb/ZnTe/NiMnSb Multilayers</b>	<b>75</b>
7.1	Introduction . . . . .	75
7.2	Growth of ZnTe on NiMnSb(001) . . . . .	76
7.3	Structural Properties of NiMnSb/ZnTe/NiMnSb Heterostructures . . . . .	79
7.4	Magnetic Properties of NiMnSb/ZnTe/NiMnSb Heterostructures . . . . .	81
7.5	Exchange Bias in NiMnSb/ZnTe/NiMnSb/NiMn Heterostructures	82
7.6	Alternative Semiconductors . . . . .	84
<b>8</b>	<b>Growth of NiMnSb on (111) Oriented Materials</b>	<b>87</b>
8.1	Introduction . . . . .	87
8.2	Growth on InP(111)A . . . . .	90
8.2.1	Growth of (In,Ga)As on InP(111)A . . . . .	90
8.2.2	Growth of NiMnSb on InP(111)A . . . . .	94
8.3	Growth on InP(111)B . . . . .	96
8.3.1	Growth of (In,Ga)As on InP(111)B . . . . .	96
8.3.2	Growth of NiMnSb on InP(111)B . . . . .	102
8.4	Structural Properties . . . . .	104
8.4.1	Structural Properties of NiMnSb(111)A . . . . .	104
8.4.2	Structural Properties of NiMnSb(111)B . . . . .	105
8.5	Magnetic Properties . . . . .	106
8.5.1	Magnetic Properties of NiMnSb(111)A . . . . .	108
8.5.2	Magnetic Properties of NiMnSb(111)B . . . . .	108
	<b>Summary</b>	<b>111</b>
	<b>Zusammenfassung</b>	<b>113</b>
<b>A</b>	<b>Material Constants</b>	<b>115</b>
A.1	Atomic Scattering Factors . . . . .	115
A.2	Lattice Constants . . . . .	116

<b>Liste eigener Veröffentlichungen</b>	<b>121</b>
<b>Lebenslauf</b>	<b>123</b>
<b>Danksagung</b>	<b>125</b>
<b>Erklärung an Eides statt</b>	<b>127</b>



# List of Figures

2.1	Crystal lattice of the full-Heusler $L2_1$ structure. . . . .	4
2.2	Crystal lattice of the half-Heusler $C1_b$ structure. . . . .	4
2.3	Crystal lattice of the zinblende B3 structure. . . . .	5
2.4	Band-structure for majority and minority spin direction of NiMnSb. . . . .	6
2.5	Schematic of the half-metallic NiMnSb/InP(111) interface . . . . .	7
3.1	Surface processes during MBE growth. . . . .	10
3.2	Schematic illustration of the three growth modes occurring during MBE growth. . . . .	11
3.3	Schematic illustration of the MBE cluster at Würzburg . . . . .	12
3.4	Two dimensional cut through the reciprocal lattice of a cubic heterostructure. . . . .	15
3.5	Reciprocal space map of an asymmetric reflection of a heterostructure. . . . .	16
3.6	Ewald sphere construction and diffraction geometry of RHEED . . . . .	22
3.7	Schematic of RHEED patterns . . . . .	23
3.8	Phase of RHEED oscillations . . . . .	24
4.1	Nomarski microscopy image of a (In,Ga)As buffer on InP(001) . . . . .	27
4.2	SIMS measurement of a sample consisting of a NiMnSb layer on an (In,Ga)As buffer layer. . . . .	28
4.3	RHEED measurement of the (4x2) reconstruction of an InP wafer covered with an oxide layer at a temperature of 500°C. . . . .	29
4.4	RHEED measurement of the (2x4) reconstruction of As stabilized InP at 530°C. . . . .	29
4.5	RHEED measurement of a suboptimal growth-start of (In,Ga)As on InP. . . . .	30
4.6	RHEED measurement of the (2x4) reconstruction of (In,Ga)As on InP during growth at 520°C. . . . .	30
4.7	RHEED measurement of the (4x3) reconstruction of (In,Ga)As on InP during cooldown under As background pressure. . . . .	31

4.8	LEED measurement of (In,Ga)As on InP at room temperature taken with an electron energy of 50 eV. . . . .	32
4.9	Overview of the samples and flux ratios. . . . .	34
4.10	HRXRD $\theta - 2\theta$ scans of the (002) reflection of the samples H124, H125 and H126. . . . .	35
4.11	HRXRD $\theta - 2\theta$ scans of the (002) reflection of the samples H121, H122 and H123. . . . .	35
4.12	HRXRD $\theta - 2\theta$ scans of the (002) reflection of the samples H127, H128 and H129. . . . .	37
4.13	RHEED measurement of a NiMnSb(001) surface after growth of 10 ML along [110]. . . . .	38
4.14	HRXRD $\theta - 2\theta$ -scan of the (002) reflection of H279 and H280. . . . .	38
5.1	Intensity of the specular spot during the growth of NiMnSb. . . . .	42
5.2	Illustration of the terrace size $d$ and step-height $h$ on a surface during or after growth. . . . .	43
5.3	Two-dimensional LEED pattern of the NiMnSb-(2x1) surface taken at an electron energy of 75 eV. . . . .	44
5.4	Line-scans of the specular spot of the NiMnSb-(2x1) surface. . . . .	44
5.5	SPA-LEED spot-profiles of the NiMnSb-(2x1) surface. . . . .	45
5.6	HRXRD $\theta - 2\theta$ scan of the (004) reflection of a smooth sample with 70 nm NiMnSb layer on a 150 nm thick (In,Ga)As buffer and the according fit. . . . .	46
5.7	HRXRD $\theta - 2\theta$ scan of the (004) reflection of a rough sample with 70 nm NiMnSb layer on a 150 nm thick (In,Ga)As buffer and the according fit . . . . .	47
5.8	GIXRD reciprocal space map of the (353) reflection of H66, a 40 nm thick NiMnSb layer on (In,Ga)As/InP. . . . .	49
5.9	GIXRD reciprocal space map of the (353) reflection of H80, a 70 nm thick NiMnSb layer on (In,Ga)As/InP. . . . .	50
5.10	GIXRD reciprocal space map of the (353) reflection of H76, a 120 nm thick NiMnSb layer on (In,Ga)As/InP. . . . .	50
5.11	GIXRD reciprocal space map of H111, a 15 nm thick NiMnSb layer on (In,Ga)As/InP. . . . .	51
5.12	Intensity ratio of the NiMnSb pseudomorphic/relaxed peak from multiple reciprocal space maps measured with different x-ray penetration depths. . . . .	52
5.13	Principle measurement setup for plan-view TEM geometry (a) and cross-section TEM geometry (b). . . . .	53
5.14	TEM bright field images and SAD patterns of NiMnSb/(In,Ga)As(001) films. . . . .	54



5.15	Magnification of the SAD pattern of Fig. 5.14. . . . .	55
5.16	TEM bright field images of a NiMnSb(001) film (40 nm). . . . .	56
5.17	The same film as in Fig. 5.16 imaged in plan view. . . . .	57
5.18	Plan view and cross sectional view of an 85 nm thick NiMnSb/ (In,Ga)As film . . . . .	58
5.19	Diagram showing an antiphase boundary plane. . . . .	59
6.1	Longitudinal MOKE geometry . . . . .	61
6.2	Typical FMR setup (from [Blu01]) . . . . .	62
6.3	Angular dependence of the maximum FMR field at 23.92 GHz for a sample with 5 nm NiMnSb. . . . .	64
6.4	FMR measurement of a sample with 10 nm NiMnSb. . . . .	64
6.5	FMR measurement of a sample with 20 nm NiMnSb. . . . .	65
6.6	FMR measurement of a sample with 40 nm NiMnSb. . . . .	65
6.7	The in-plane uniaxial anisotropy field $2K_U/M_s$ as a function of the inverse NiMnSb film thickness $1/d$ . . . . .	66
6.8	$4\pi M_{eff}$ as a function of the NiMnSb film thickness $d$ . . . . .	67
6.9	The in-plane fourfold anisotropy field $2K_1/M_s$ as a function of the NiMnSb film thickness $d$ . . . . .	67
6.10	The FMR linewidth at 24 GHz versus the angle $\varphi_m$ between the magnetization and the in-plane [100] crystalline axis. . . . .	68
6.11	Hysteresis curve of a sample with 5 nm NiMnSb along $[1\bar{1}0]$ mea- sured by MOKE. . . . .	69
6.12	Hysteresis curve of a sample with 5 nm NiMnSb along [100] mea- sured by MOKE. . . . .	70
6.13	Hysteresis curve of a sample with 5 nm NiMnSb along [110] mea- sured by MOKE. . . . .	70
6.14	Hysteresis curves obtained by SQUID measurements of three sam- ples with different thicknesses of the NiMnSb layer. . . . .	71
6.15	Magnetization of a 40 nm thick NiMnSb layer versus temperature. . . . .	72
6.16	Hysteresis curves taken by SQUID of a sample consisting of 5 nm NiMn on top of a 10 nm NiMnSb layer along $[1\bar{1}0]$ at different tem- peratures. . . . .	73
7.1	RHEED measurement along the [110] direction of a 1ML thick ZnTe layer on NiMnSb. . . . .	76
7.2	RHEED measurement along the [100] direction of a 1ML thick ZnTe layer on NiMnSb. . . . .	77
7.3	RHEED image along the $[1\bar{1}0]$ direction of a 10 ML thick ZnTe layer on NiMnSb. . . . .	78
7.4	RHEED image along the $[1\bar{1}0]$ direction of a 10 nm thick ZnTe layer on NiMnSb. . . . .	79

7.5	HRXRD reciprocal space map of the (115) reflection of a sample consisting of InP substrate, 150 nm (In,Ga)As buffer layer, 200 nm NiMnSb and 500 nm ZnTe. . . . .	80
7.6	Sample design of the NiMnSb/ZnTe/NiMnSb multilayer structure investigated by XRR. . . . .	81
7.7	Measured XRR data and corresponding best fit. The fit parameters are listed in Table 7.1. . . . .	82
7.8	Sample design of a tri-layer structure used for double switching experiments. . . . .	83
7.9	SQUID measurement of a sample consisting of a NiMnSb/ZnTe/NiMnSb structure taken at room temperature with the magnetic field aligned along [100]. . . . .	83
7.10	Sample design of a TMR stack which utilizes exchange biasing of the top ferromagnetic layer. . . . .	85
7.11	SQUID measurement of a sample consisting of a NiMnSb/ZnTe/NiMnSb/NiMn structure taken at 4K with the magnetic field aligned along $[1\bar{1}0]$ . . . . .	86
8.1	Schematic of an InP crystal with a (111)A surface orientation, terminated by In atoms. . . . .	88
8.2	Schematic of an InP crystal with a (111)A surface orientation, terminated by P atoms. . . . .	89
8.3	Schematic of an InP crystal with a (111)B surface orientation, terminated by P atoms. . . . .	90
8.4	Schematic of an InP crystal with a (111)B surface orientation, terminated by In atoms. . . . .	91
8.5	Schematic of a rotation twin defect. . . . .	92
8.6	RHEED pattern of an (In,Ga)As layer on an InP (111)A surface during growth at 530°C . . . . .	93
8.7	RHEED pattern of an (In,Ga)As layer on an InP (111)A surface after growth at 250°C . . . . .	94
8.8	Nomarski microscopy image of an (In,Ga)As buffer on InP(111)A grown with a III/V ratio of 0.07. . . . .	95
8.9	Nomarski microscopy image of an (In,Ga)As buffer on InP(111)A grown with a III/V ratio of 0.03. . . . .	96
8.10	RHEED pattern of a NiMnSb surface on InP (111)A during growth at 250°C after 5 nm . . . . .	97
8.11	RHEED pattern of a NiMnSb surface on InP (111)A after 120 nm . . . . .	97
8.12	RHEED pattern of the epi-ready oxide layer on top of InP(111)B along $[1\bar{1}0]$ and $[11\bar{2}]$ at 400°C. . . . .	98

---

8.13 RHEED pattern of the epi-ready oxide layer on top of InP(111)B along $[\bar{1}\bar{1}0]$ and $[11\bar{2}]$ at 500°C. . . . .	99
8.14 RHEED pattern of 15 nm thick (In,Ga)As on InP(111)B during growth at 530°C. . . . .	100
8.15 RHEED pattern of a 200 nm thick (In,Ga)As layer on InP(111)B at 250°C. . . . .	100
8.16 Nomarski microscopy image of an (In,Ga)As layer on InP(111)B grown with a III/V ratio of 0.03. . . . .	101
8.17 Nomarski microscopy image of an (In,Ga)As layer on InP(111)B grown with a III/V ratio of 0.12. . . . .	101
8.18 Nomarski microscopy image of an (In,Ga)As layer on InP(111)B grown with a III/V ratio of 0.12 and optimized degassing. . . . .	102
8.19 RHEED pattern of a 10 nm thick NiMnSb layer grown on (In,Ga)As/ InP(111)B . . . . .	103
8.20 HRXRD $\theta - 2\theta$ -scan of the (222) reflection of a sample consisting of NiMnSb and (In,Ga)As layer on InP(111)A. . . . .	104
8.21 HRXRD $\theta - 2\theta$ -scan of the (222) reflection of a sample consisting of NiMnSb and (In,Ga)As layer on InP(111)B. . . . .	106
8.22 HRXRD $\theta - 2\theta$ -scan of an off-stoichiometric sample ranging from the InP(111) to the (222) reflection. . . . .	107
8.23 HRXRD $\theta - 2\theta$ -scan of a stoichiometric NiMnSb/InP(111)B sample ranging from the NiMnSb(111) to the InP (222) reflection. . . . .	107
8.24 FMR measurement of a 40 nm NiMnSb layer on InP(111)A . . . . .	108
8.25 FMR measurement of a 40 nm NiMnSb layer on InP(111)B with a miscut along $[1\bar{1}0]$ . . . . .	109
8.26 FMR measurement of a 40 nm NiMnSb layer on InP(111)B with a miscut along $[11\bar{2}]$ . . . . .	110



# List of Tables

3.1	X-ray intensity ratios of different crystals . . . . .	21
4.1	RHEED observations during the growth of NiMnSb with different flux ratios . . . . .	36
7.1	Fitting parameters for the x-ray reflectivity data shown in Fig. 7.6. .	84
A.1	Atomic scattering factors . . . . .	115
A.2	Lattice constants . . . . .	116



# Chapter 1

## Introduction

Since the invention of the transistor by J. Bardeen, W.H. Brattain and W.B. Shockley in 1947 the world of computers and integrated circuits was dominated by semiconductor-based electronics. Information is transported using the charge of the electrons, with the presence or absence of electrons at a specific location indicating the binary states 1 and 0.

In recent years, however, magnetoelectronic devices have found an enormous interest, which use the spin of the electrons rather than the charge. In these devices the spin-up and spin-down states of the electron are used to specify the two binary states. Because of this feature the term “spin electronics” or shorter “spintronics” was developed.

Due to their advantages over standard electronics like the on-the-fly reprogramming capability, low power consumption and non-volatile built-in memory, these spintronic devices promise to revolutionize microprocessor and computation hardware. Already today modern computers rely on magnetoresistive elements in the read sensors of their hard-disks, which are based on the giant magnetoresistance (GMR) effect. In the near future, also spintronic replacements of the volatile random access memory (RAM), the magnetic random access memory (MRAM) which are based on the tunnelling magnetoresistance (TMR) will be available. Information stored in these MRAM cells can be held indefinitely without power and switching speeds are comparable to conventional memories.

The two magnetoresistance effects used in these devices have various similarities. A GMR or TMR device consists of two ferromagnets, separated by a very thin non-magnetic spacer which consists of a metal for GMR or an insulator for TMR. The resistance of these devices depends on the relative magnetization orientation of the ferromagnets, which can be parallel or antiparallel. Whereas GMR and TMR devices have the same basic functionality, the underlying physics is fundamentally different. However, in both cases the spin-polarization in the ferromagnetic layers influence the resistance change between the parallel and

the anti-parallel state. It is therefore of crucial importance to have highly spin-polarized materials for these applications.

Furthermore, a connection between the reliable semiconductor technology and the new spintronics field would be very desirable. However, for this purpose spin-polarized electrons inside the semiconductor have to be generated. Whereas this “spin-injection” has been achieved using magnetic semiconductors, this technique suffers from the necessity of very low temperatures, which make an application impossible. Spin-injection using room-temperature ferromagnets has been proven to be highly inefficient, since the spin-polarization of the ferromagnet has to be very close to 1 in order to achieve efficient spin-injection at room-temperature in this setup [Sch00].

Whereas the need for highly spin-polarized materials is evident, the fabrication of these materials and their integration into existing semiconductor technology is still under heavy investigation.

In this work the fabrication of the half-Heusler alloy NiMnSb, which is a member of the half-metallic ferromagnets with a spin-polarization of 100%, and its magnetic and structural properties have been investigated.

Chapter 2 gives an overview of the previous work on NiMnSb and illustrates its basic properties, while chapter 3 addresses experimental details and theoretical principles used in the investigation of NiMnSb.

In chapter 4 the growth of (001) oriented NiMnSb films using molecular beam epitaxy is described. Details about the different parameters during the growth are given as well as their implications on the quality of the resulting NiMnSb layer.

Chapter 5 addresses the structural properties of these films. Different imaging and diffraction methods have been used in order to characterize the surface as well as the bulk structure and details about the defects forming in these layers during growth are given.

Chapter 6 focuses on the magnetic characteristics of these thin NiMnSb films. Magnetic anisotropies, hysteresis curves and the interaction of NiMnSb with antiferromagnetic layers are discussed.

The fabrication of TMR structures consisting of NiMnSb layers separated by ZnTe spacer layers and their characterization are illustrated in chapter 7. Details on the fabrication technique as well as structural and magnetic properties of these heterostructures will be given.

NiMnSb films on (111) oriented substrates are the subject of chapter 8. In this part the growth by molecular beam epitaxy as well as the structural and magnetic properties of NiMnSb(111) layers are described.



# Chapter 2

## Heusler Compounds

### 2.1 Historical Overview

In the early 20th century, Fritz Heusler investigated a number of magnetic materials based on the  $L2_1$  and  $C1_b$  crystallographic phases. These materials caught his interest since they showed strong ferromagnetism despite the fact that they consisted of elements which at that time were considered to be nonmagnetic. This class of materials, which was later on called “Heusler alloys” to honor their discoverer, has attracted much interest from theorists as well as experimentalists.

The Heusler alloys can be divided into two groups: The full-Heusler alloys having the  $L2_1$  and the half-Heusler alloys having the  $C1_b$  crystal structure. These two crystallographic phases are closely related. They both typically consist of three different elements, which are ordered in a fcc lattice. The full-Heusler structure has a four-atomic basis with the atoms at the positions X:(0,0,0), Y:( $\frac{1}{4}, \frac{1}{4}, \frac{1}{4}$ ), X:( $\frac{1}{2}, \frac{1}{2}, \frac{1}{2}$ ) and Z:( $\frac{3}{4}, \frac{3}{4}, \frac{3}{4}$ )(Fig. 2.1). For the half-Heusler alloys the position at ( $\frac{1}{2}, \frac{1}{2}, \frac{1}{2}$ ) remains empty (Fig. 2.2). These two crystal structures are also very similar to the zincblende structure of many conventional semiconductors, which consists of a fcc lattice with a two-atomic basis at the positions X:(0,0,0), Y:( $\frac{1}{4}, \frac{1}{4}, \frac{1}{4}$ ) (Fig. 2.3).

NiMnSb is a member of the half-Heusler alloys. Its structural and magnetic properties were first described in detail by Lore Castelliz in 1955 [Cas55]. In this paper the first glimpse of half-metallicity of NiMnSb was observed: The magnetization per unit cell of stoichiometric NiMnSb was  $4.0 \mu_B$ , which suggests that the conducting electrons in this material all have the same spin orientation. In 1983 the group of R.A. de Groot discovered by band-structure calculations that the bandstructure of NiMnSb has some unique features which lead to a band gap at the Fermi-level for the minority electrons whereas for the majority electrons the Fermi-level lies in the band [dG83] (Fig. 2.4). This means that the conduction electrons are fully spin polarized and therefore NiMnSb would be a perfect

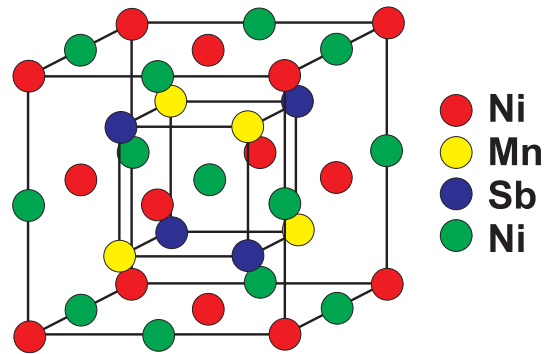


Figure 2.1: Crystal lattice of the full-Heusler  $L2_1$  structure, e.g.  $\text{Ni}_2\text{MnSb}$ , with Ni at  $(0,0,0)$ , Mn at  $(\frac{1}{4}, \frac{1}{4}, \frac{1}{4})$ , Ni at  $(\frac{1}{2}, \frac{1}{2}, \frac{1}{2})$  and Sb at  $(\frac{3}{4}, \frac{3}{4}, \frac{3}{4})$ .

spin filter. Since the experimentally determined Curie-temperature is rather large with 730 K, this half-Heusler material has a large potential for devices using spin-polarized currents.

## 2.2 Properties of NiMnSb

The half-metallic character of NiMnSb was under heavy investigation after the discovery of de Groot and much experimental effort was devoted to NiMnSb. However, first experiments probing the spin-polarization of NiMnSb like spin-polarized photoelectron spectroscopy [Bon85], spin-polarized tunnelling [Tan99] and Andreev-reflection [Sou98] show a spin polarization far below 100%. Nevertheless, some experiments like spin-resolved positron annihilation [Han86, Han90] and infrared reflectance spectroscopy [Man99] support the half-metallic

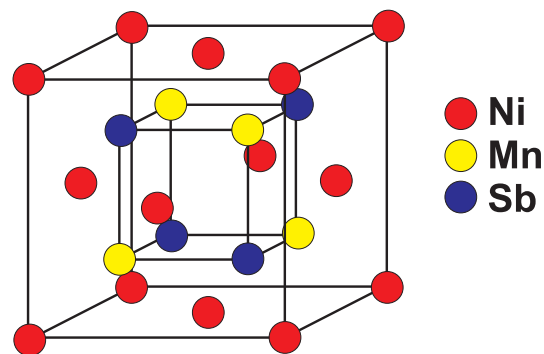


Figure 2.2: Crystal lattice of the half-Heusler  $C1_b$  structure, e.g.  $\text{NiMnSb}$ , with Ni at  $(0,0,0)$ , Mn at  $(\frac{1}{4}, \frac{1}{4}, \frac{1}{4})$  and Sb at  $(\frac{3}{4}, \frac{3}{4}, \frac{3}{4})$ .

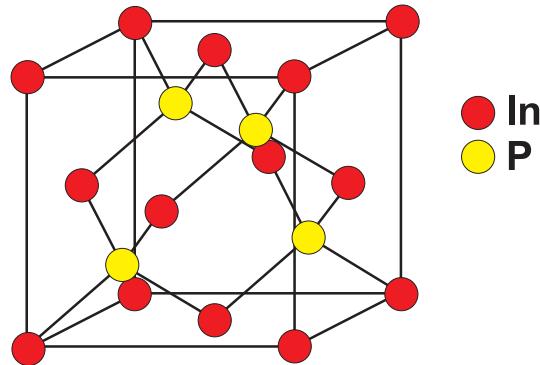


Figure 2.3: Crystal lattice of the zincblende B3 structure, e.g. InP, with In at  $(0,0,0)$  and P at  $(\frac{1}{4}, \frac{1}{4}, \frac{1}{4})$ .

nature of NiMnSb. The main difference between these experiments is that the second set probe the NiMnSb bulk, whereas the first set is, at least to some extent, surface or interface sensitive. This means the high spin-polarization of bulk NiMnSb is lost at its surfaces and interfaces. Studies of the surface composition of NiMnSb by angle-resolved x-ray photoemission spectroscopy report Sb and Mn surface segregation in NiMnSb [Ris00], which is an indication of a difference of the chemical potential between the bulk and the surface [Dow90]. This difference can be related to the creation of a surface electronic structure quite different from the bulk. Furthermore also the surface lattice structure may be different from the bulk.

However, theoretical calculations of several interface compositions of NiMnSb with a number of semiconductor materials revealed that half-metallic interfaces of NiMnSb can exist [dW01]. The NiMnSb(111)/CdS(111) and the NiMnSb(111)/InP(111) interface with a Sb-S or Sb-P bond show a restored half-metallic character of NiMnSb across these interfaces. The loss of the spin-polarization in most interface configurations is attributed to the symmetry breaking at these interfaces. Fig. 2.5 shows the NiMnSb/InP(111) interface for which a half-metallic character was calculated. Due to the Sb-P bond, the bulk configuration of the Mn atoms, which have the most important contribution to the band structure, is not changed at this interface. Calculations of the band structure of other (111) and (001) oriented interfaces showed no half-metallicity for these interfaces.

Since the discovery of the half-metallic character of NiMnSb many different fabrication techniques have been used. The first NiMnSb materials were produced by melting of the three elements [Cas55, Ott89]. This resulted in mainly polycrystalline bulk material. From these samples later on single-crystalline material was synthesized [Hor96]. However, these techniques allowed only for the production of bulk material. To study NiMnSb thin films, at first sputtering tech-

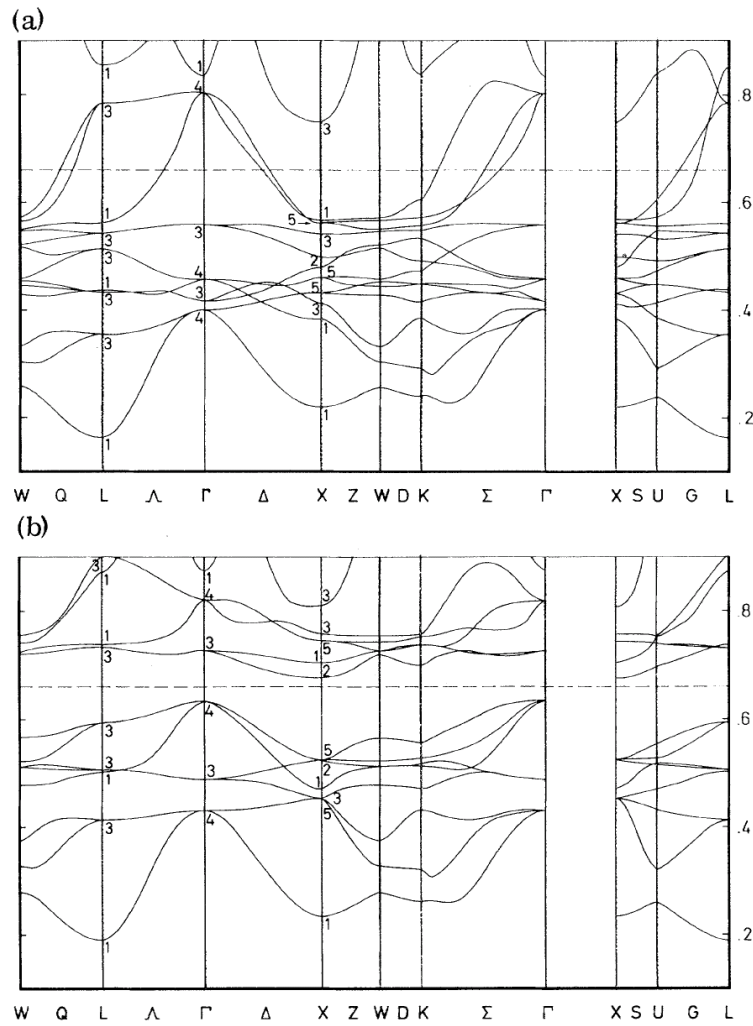


Figure 2.4: Band-structure for majority spin direction (a) and minority spin direction (b) of NiMnSb, calculated by de Groot and coworkers [dG83]. The bandgap at the Fermi-energy (dotted line) for the minority spin direction is recognizable, leading to the half-metallic character of NiMnSb.

niques were applied [Cab97]. As sputtering targets also polycrystalline NiMnSb was used. In recent years, however, epitaxial techniques allowed for the deposition of single-crystal NiMnSb thin films on isolators [Tur02] and semiconductors [Roy00]. Nevertheless, the substrate crystals used for these growth experiments had a large lattice mismatch to NiMnSb, causing the NiMnSb film to relax during growth and thereby introduce a large number of misfit dislocations.

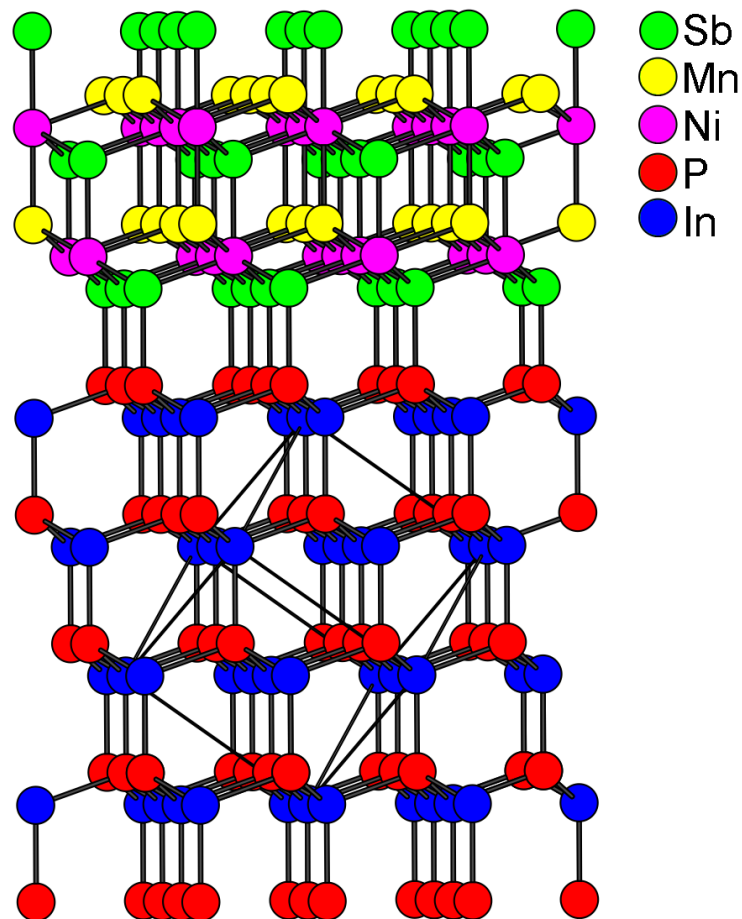


Figure 2.5: Schematic of the half-metallic NiMnSb/InP(111) interface. Note the Sb-P bond at the interface. The bonding configuration of the Mn atoms at the interface, which play the most important role for the bandstructure, is unchanged in comparison to the bulk structure. For clarity, the simple cubic unit cell of the InP zincblende lattice is marked with thin lines.



# Chapter 3

## Basic Physical and Technological Principles

### 3.1 Molecular Beam Epitaxy

Molecular Beam Epitaxy (MBE) has evolved into a powerful and variable tool for producing tailored structures of the most diverse materials. Whereas in the early days of MBE its application was mainly limited to semiconductors, today a wide variety of materials ranging from pure insulators to magnetic metals are within its potential. One of the main advantages of MBE is that it is not limited to the deposition of identical or isovalent materials but very different types of materials can be grown on top of each other. This so called “heteroepitaxy” creates the opportunity to combine various material systems and its unique properties in one structure.

This chapter will give an overview of the principles of MBE and the experimental setup at the Universität Würzburg.

#### 3.1.1 Principles of MBE

The principle of MBE is straight forward. In an ultra-high vacuum (UHV) system thermal-energy molecular or atomic beams of different elements react at the surface of a substrate and form a thin film. The composition of the grown epilayer mainly depends on the arrival rate of the different elements. This rate depends on the evaporation rate of the according sources which can be controlled by the temperature of the materials inside these sources.

To block the molecular beams simple mechanical shutters in front of the evaporation sources are used. Since the growth rates are typically of the magnitude of 1ML/s, interruptions of the beam fluxes can be abrupt in the range of atomic

layers.

Since the reaction of the impinging atoms or molecules on the surface is not in thermodynamic equilibrium a theoretical description of the processes is very complex. The reaction of the evaporated materials at the surface of the substrate can be divided into four parts:

- i) adsorption of the incoming molecules on the substrate surface
- ii) migration and dissociation of the adsorbed molecules
- iii) incorporation of the adsorbed molecules into the bulk crystal lattice
- iv) thermal desorption of the molecules not incorporated into the crystal

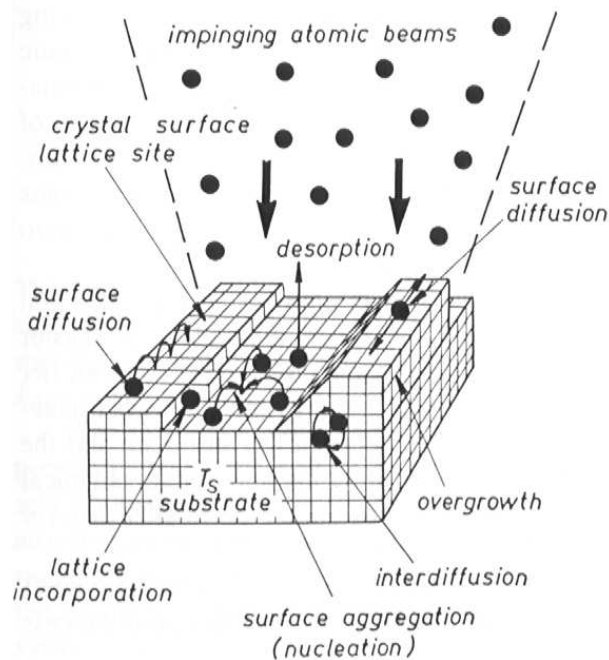


Figure 3.1: Schematic illustration of the surface processes occurring during MBE growth [Her96].

A schematic illustration of these processes is shown in Fig. 3.1. A theoretical description of the growth is difficult due to the large number of non-equilibrium processes involved. All these processes are depending on numerous parameters. Most easily accessible during the MBE process are the temperature of the substrate surface and the composition of the impinging molecular beam.

In general three growth modes on surfaces can be distinguished (Fig. 3.2):



- i) Layer-by-layer or Frank-van der Merwe mode
- ii) Layer plus island or Stranski-Krastanov mode
- iii) Island or Volmer-Weber mode

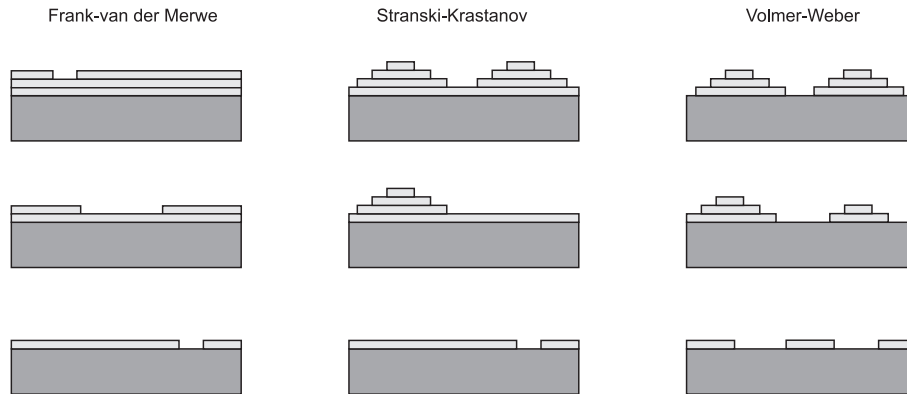


Figure 3.2: Schematic illustration of the three growth modes occurring during MBE growth.

In the Volmer-Weber growth mode the atoms on the surface directly nucleate to small clusters and then grow into islands of the condensed phase. This happens when the atoms of the evaporated sources are more tightly bound to each other than to the substrate surface. In Frank-van der Merwe mode opposite characteristics are shown. In this case the impinging atoms are more strongly bound to the substrate than to each other. Thus the first arriving atoms on the surface condense into a complete monolayer which then becomes covered with a second monolayer and so on. The Stranski-Krastanov mode is a mixture between Frank-van der Merwe and Volmer-Weber. In this mode a few monolayers are grown in the layer-by-layer regime until islands are formed on top of these wetting layers. Whereas the Stranski-Krastanov and Volmer-Weber modes have their importance for the growth of quantum-dots, for standard thin film growth the Frank-van der Merwe mode is preferred. A more detailed analysis of the principles of MBE growth can be found in [Her96].

### 3.1.2 MBE Setup

The MBE-cluster at the Universität Würzburg (Fig. 3.3), which consists of 6 interconnected MBE-chambers and various in-situ characterization methods, provides an ideal environment for development and preparation of novel structures. Two chambers are devoted to the growth of As and Sb based III-V materials, two

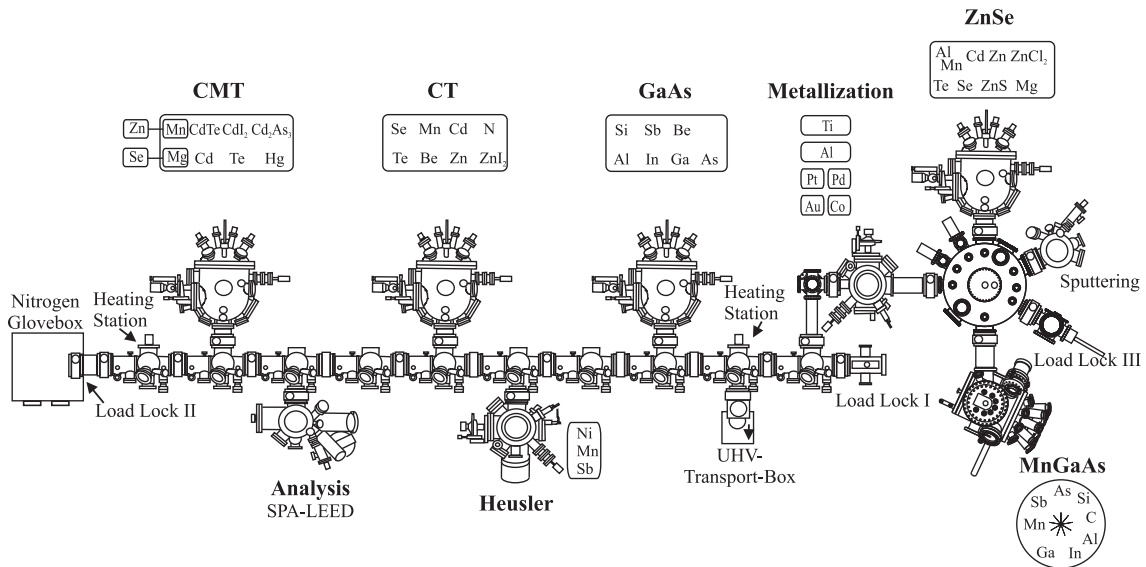


Figure 3.3: Schematic illustration of the MBE cluster at the Universität Würzburg. There are six MBE chambers equipped with different materials interconnected via UHV transport modules. A sample grown in any of these six chambers can be transported to any other chamber without breaking the UHV.

chambers are used for the growth of wide bandgap Se and Te containing II-VI materials, in one chamber the growth of Hg-containing narrow bandgap II-VI materials are studied and one chamber is solely dedicated to the growth of the half-Heusler material NiMnSb. The largest advantage of this unique setup is the wide variety of different material combinations for the growth of epitaxial heterostructures.

In this work three MBE-chambers have been used: The GaAs chamber for the growth of (In,Ga)As and InP substrate preparation, the Heusler chamber for the growth of NiMnSb ferromagnets and NiMn antiferromagnets and the CT chamber for the overgrowth of NiMnSb by ZnTe layers. The GaAs and the CT growth chambers are both Riber 2300 machines, equipped with liquid nitrogen cooled shrouds as well as an ion-getter and a cryo-pump to achieve background pressures in the range of  $6 \times 10^{-11}$  mbar. The evaporation cells used in both chambers are mainly Knudsen cells. The Ga and the As evaporation sources in the GaAs chamber, however, have a different design. The Ga cell takes advantage of the SUMO-cell design, developed by VEECO. In this design the orifice of the cell is small compared to the diameter of the container holding the Ga-material. The orifice and container are heated separately, thus the top of the cell can be held at higher temperature than the material. This leads to a reduction of oval defects during growth [VEE96]. Additionally, the large size of the container and

the therefore large amount of Ga-material inside the cell allows for long operating times. For As evaporation a valved cracker cell is used. The cell is operated in the non-cracking mode, thus evaporating  $\text{As}_4$  molecules. The big advantage of this design is that the  $\text{As}_4$ -flux can be changed almost instantly by changing the opening of the valve of this cell. Furthermore, a very large amount of As-material, about 10 times as much as for standard effusion cells, can be filled into this valved cracker cell, allowing for a long operation time without the need of refilling the cell.

The design of the Heusler chamber built by MBE-Komponenten needed for the growth of NiMnSb, however, is different. In contrast to the Riber MBE chambers, which use vertical substrate alignment during growth, this design includes a horizontal substrate alignment. This setup has the advantage that this chamber needs less space in the lab. However, the drawback is that at some point the substrate has to be turned inside the UHV during transport between one of the Riber chambers and the Heusler chamber, which creates an additional error potential for the sample transfer. The Heusler chamber is equipped with only one cryo-pump and the cooling shrouds are filled with a cooling liquid held at  $-20^\circ\text{C}$ , giving a background pressure of typically  $1 \times 10^{-10}$  mbar. The effusion cells of the Heusler chamber are solely standard Knudsen cells. The Ni cell, which has to be able to reach very high temperatures in the range of  $1500^\circ\text{C}$ , needs a special crucible design to withstand both the high temperature and the aggressive liquid Ni material. In this case a Tantalum crucible with an  $\text{Al}_2\text{O}_3$  insert is employed. Since  $\text{Al}_2\text{O}_3$  is a very brittle material, special care has to be taken to ensure that the stress introduced by the heating and cooling of the Ni-material is not causing the  $\text{Al}_2\text{O}_3$  insert to break. The consequence would be an alloy of Ni and the Ta crucible which causes the Ni to leak into the filament parts of the cell resulting in permanent and irreversible damage. The Mn and Sb cells on the other hand can utilize standard Pyrolytic Boron Nitride (PBN) crucibles due to their lower operating temperature.

## 3.2 X-Ray Diffraction

In this work several x-ray diffraction techniques for the characterization of MBE-grown layers have been used. For a basic introduction on x-ray diffraction see a textbook on solid-state physics, like [Kit96].

Two basic experimental setups have been used for the x-ray measurements in this work. A Philips X'Pert diffractometer capable of high resolution x-ray diffraction (HRXRD) has been used for the standard  $\theta - 2\theta$ -scans, rocking curves and reciprocal space maps of asymmetric reflections. Thickness dependent reciprocal space maps have been measured at the BW2 beamline at the synchrotron

facility in Hamburg using grazing incidence x-ray diffraction (GIXRD). In the following sections an introduction into the basic principles of these measurement techniques is given. Whereas for the HRXRD measurements the x-rays are penetrating the sample in an angle far from the critical angle, GIXRD measurements actually can take advantage of x-rays penetrating the sample below or close to the critical angle. In this way the penetration depth of the probing x-rays can be controlled. Thereby different parts of the sample in different depths can be examined.

### 3.2.1 Reciprocal Space Maps

The Ewald-construction offers a descriptive foundation for the understanding of x-ray diffraction of heterostructures. In this picture the diffraction is described in the momentum or reciprocal space. The wave-vectors of the incoming and diffracted x-rays,  $\mathbf{k}_i$  and  $\mathbf{k}_e$ , define the diffraction plane. Since the diffraction is elastic, both vectors have the same length  $\frac{1}{\lambda}$ . The difference between  $\mathbf{k}_e$  and  $\mathbf{k}_i$  is called the diffraction vector  $\mathbf{q} = \mathbf{k}_e - \mathbf{k}_i$ . The reciprocal vectors  $\mathbf{b}_1$ ,  $\mathbf{b}_2$  and  $\mathbf{b}_3$  are defined in the following way:

$$\mathbf{b}_1 = \frac{2\pi}{V}(\mathbf{a}_2 \times \mathbf{a}_3) \quad \mathbf{b}_2 = \frac{2\pi}{V}(\mathbf{a}_3 \times \mathbf{a}_1) \quad \mathbf{b}_3 = \frac{2\pi}{V}(\mathbf{a}_1 \times \mathbf{a}_2)$$

with  $\mathbf{a}_1$ ,  $\mathbf{a}_2$  and  $\mathbf{a}_3$  the unit vectors of the real space lattice and  $V$  the volume of the unit cell. According to the Laue-equations, constructive interference can only be achieved if the diffraction vector  $\mathbf{q}$  can be expressed as a linear combination of the three reciprocal vectors:

$$\mathbf{q} = \mathbf{G} \tag{3.1}$$

$$\mathbf{G} = h\mathbf{b}_1 + k\mathbf{b}_2 + l\mathbf{b}_3 \tag{3.2}$$

$\mathbf{G}$  is the reciprocal lattice vector and  $h$ ,  $k$  and  $l$  are the Miller-indices.

In the following a cubic substrate with lattice constant  $a_S$  is assumed. Fig. 3.4 shows a 2-dimensional cut through the reciprocal lattice of a cubic heterostructure. The materials which are deposited by heteroepitaxy on semiconductor substrates in general differ in their lattice constants  $a_L$ . If this difference, the so called lattice mismatch, is sufficiently small, the epitaxial layer grows strained at first. The epitaxial layer takes on the lateral lattice constant of the substrate  $a_{\parallel} = a_S$ . This state of the layer is called "pseudomorphic". The distortion is compensated by a change of the vertical lattice constant in growth direction  $a_{\perp}$ . The cubic unit cell is then tetragonal distorted. The energy of this distortion rises with the thickness of the epitaxial layer. How much the lattice of a pseudomorphic layer is distorted can be described by the Poisson ratio  $\nu$ . It can be expressed as follows:

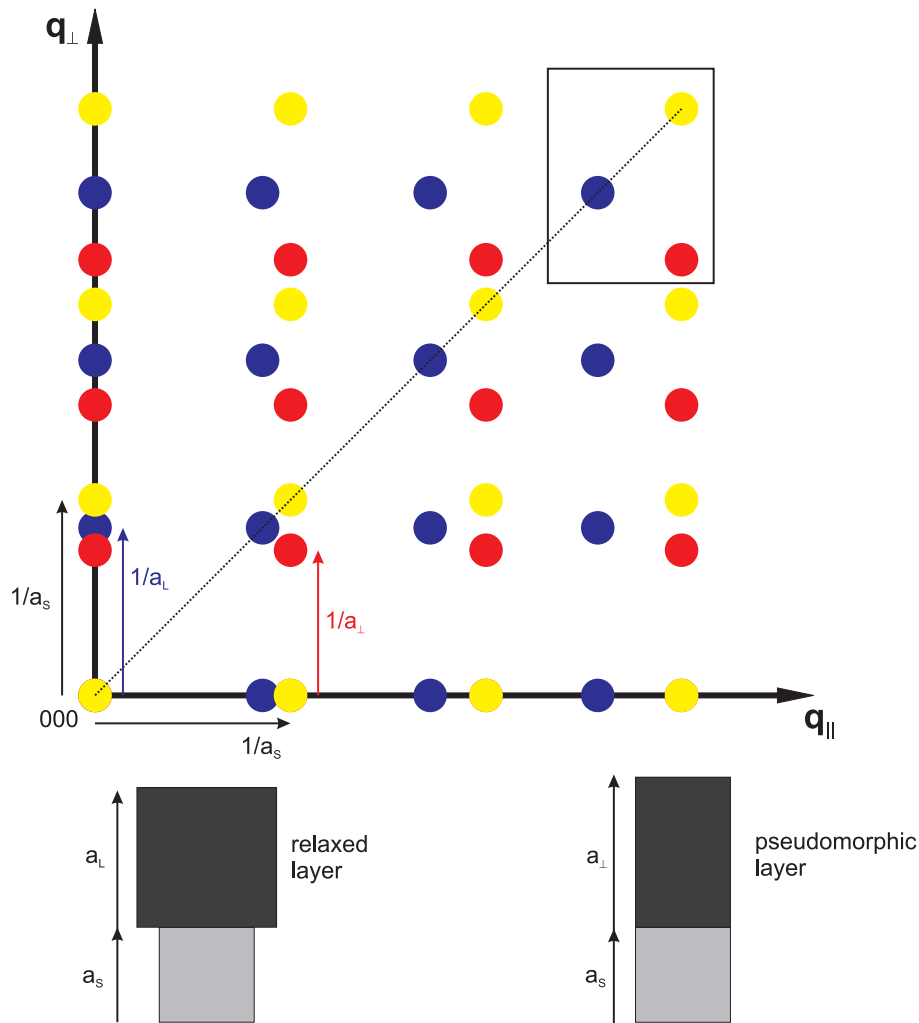


Figure 3.4: Two dimensional cut through the reciprocal lattice of a cubic heterostructure. The rectangle indicated in the upper right part of the figure is magnified in Fig. 3.5.

$$\nu = \frac{a_L - a_{\perp}}{2a_S - a_{\perp} - a_L} \quad (3.3)$$

The Poisson ratio of almost all semiconductor materials is in the neighborhood of 0.3. If the distortion energy is large enough, a dislocation is formed. At this point the critical thickness of the epitaxial layer is reached, the difference of the lattice constants will then be compensated by insertions of mismatch dislocations. The beginning of the relaxation process can be seen by the different intensity distribution in the reciprocal space. At the end of this process the epitaxial layer has a cubic unit cell with the lattice constant  $a_L$ .

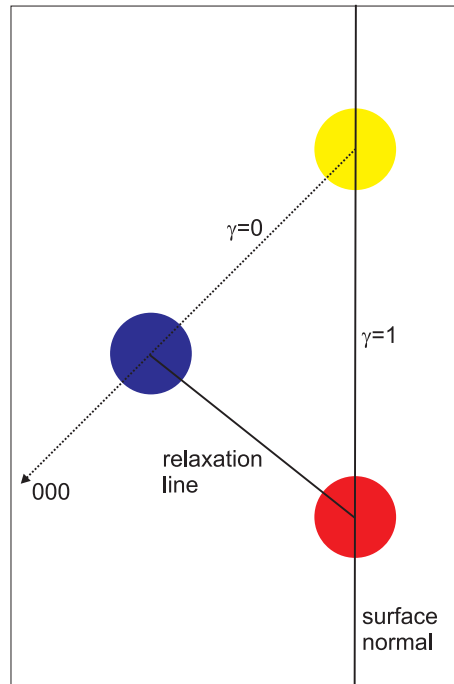


Figure 3.5: Reciprocal space map of an asymmetric reflection of a heterostructure.

For the characterization of partly relaxed layers the distortion parameter  $\gamma$  is used, which describes a linear displacement along the relaxation line (Fig. 3.5). It is defined by

$$\gamma = 1 - \frac{\frac{a_{\parallel} - a_S}{a_S}}{\frac{a_L - a_S}{a_S}} \quad (3.4)$$

All pseudomorphic layers have  $\gamma = 1$ , fully relaxed layers have  $\gamma = 0$ .

To record reciprocal space maps with a standard 4-circle diffractometer<sup>1</sup>, several  $\theta - 2\theta$ -scans with varying  $\omega$ -offset have to be measured. In reciprocal space,  $\theta - 2\theta$ -scans give information along a straight line going through the origin. Varying the angle  $\omega$  results in a circle with the origin as the center. Therefore the set of  $\theta - 2\theta$ -scans under different  $\omega$ -angles gives a picture of a 2-dimensional cut through the reciprocal space.

<sup>1</sup>4-circle diffractometer: 4 degrees of freedom,  $\omega, \theta, \phi, \psi$ . For direct mapping of the reciprocal space to diffractometer-angles, 6 degrees of freedom are necessary.

### 3.2.2 Thickness Fringes

The diffraction pattern of an infinite crystal shows infinitely sharp peaks. However, the crystal measured by an experiment is always limited by its boundaries or by the penetration depth of the probing x-rays. Especially epitaxial layers are of limited thickness, while the size of the sample and the thickness of the substrate can be assumed to be infinite in good approximation. The calculation of the diffraction pattern is analog to a Fourier transform of the real space crystal. The Fourier transform of an infinite lattice is a reciprocal lattice with infinite sharp peaks at locations with integer Miller indices  $h$ ,  $k$  and  $l$  without any subsidiary maxima. To adjust for the finite size of the epi-layer the infinite lattice is multiplied by a box-shaped function, which is 1 inside and 0 outside the box. For simplicity, the following consideration will be held to one dimension.

An infinite one-dimensional lattice with distance  $a$  can be described as:

$$g(x) = \sum_{n=-\infty}^{\infty} \delta(x - na). \quad (3.5)$$

To obtain a finite lattice we can multiply this function by a box-shaped function  $s(x)$  with width  $d$ :

$$s(x) = \begin{cases} 0 & : |x| > d/2 \\ 1 & : |x| \leq d/2 \end{cases} \quad (3.6)$$

$$f(x) = s(x) \cdot g(x) = s(x) \sum_{n=-\infty}^{\infty} \delta(x - na). \quad (3.7)$$

The Fourier transform of the box-function can be calculated to:

$$F_s(q) = \int_{-d/2}^{d/2} e^{2\pi i q x} dx = \frac{\sin \pi d q}{\pi q}. \quad (3.8)$$

The Fourier transform of  $g(x)$  can be written as

$$F_g(q) = \sum_{n=-\infty}^{\infty} e^{2\pi i q n a}. \quad (3.9)$$

Considering that

$$\sum_0^{\infty} x^n = (1 - x)^{-1} \quad (3.10)$$

we can write

$$\begin{aligned}
F_g(q) &= \sum_0^{\infty} (e^{2\pi iqa})^n + \sum_0^{\infty} (e^{-2\pi iqa})^n - 1 \\
&= (1 - e^{2\pi iqa})^{-1} + (1 - e^{-2\pi iqa})^{-1} - 1 \\
&= 0
\end{aligned} \tag{3.11}$$

except that

$$F_g(q) = \infty \quad \text{for} \quad e^{2\pi iqa} = 1. \tag{3.12}$$

Therefore if  $2\pi iqa = 2h\pi$  where  $h$  is an integer or  $q = h/a$ , then

$$F_g(q) = a^{-1} \sum_h \delta(q - h/a). \tag{3.13}$$

Thus the Fourier transform of an infinite lattice is a set of equally spaced delta functions of distance  $a^{-1}$  in reciprocal space.

Considering the multiplication theorem we can write the Fourier transform of  $f(x)$  as:

$$\begin{aligned}
F_f(q) &= F_s(q) * F_g(q) \\
&= d \frac{\sin(\pi dq)}{\pi dq} * \sum_h \delta(q - h/a).
\end{aligned} \tag{3.14}$$

The reciprocal space of a limited lattice therefore consists of sharp peaks at intervals  $q = 1/a$  with side ripples of the form of  $\frac{\sin(x)}{x}$ . The period of these side peaks is solely depending on the length  $d$  of the limited lattice, which corresponds to the thickness of an epitaxial layer in a heterostructure. Therefore the measurement of the reciprocal space along the  $q_{\perp}$ -direction gives additional information about the thicknesses of the different layers in this sample.

This calculation assumes perfect surfaces and interfaces. If a surface and interface roughness is introduced, the analytical calculation gets very complicated. A detailed description of different theories for the similar effect of x-ray reflectivity can be found in [Hol99]. Basically rough interfaces cause a larger damping of the thickness fringes than expected by the  $\frac{\sin(x)}{x}$ -behavior up to an extend where no thickness fringes can be observed at all.

### 3.2.3 Intensity of Reflections

In the calculations above we assumed infinitely sharp concentrations of electrons for our imaginary scattering experiment. The scattered intensity of a reflection



$hkl$  from a real crystal, however, can be described by the structure factor  $F_{hkl}$ . The intensity is proportional to the squared absolute value of the structure factor  $I_{hkl} \propto |F_{hkl}|^2$ . The structure factor can be calculated by the Fourier transform of the electron density  $\rho(\mathbf{r})$  inside the unit cell:

$$F(\mathbf{q}) = \int_V \rho(\mathbf{r}) e^{i\mathbf{q}\cdot\mathbf{r}} dV \quad (3.15)$$

The unit cell is built up of atoms, therefore we can replace the electron density of the unit cell by a sum over the electron density of all atoms inside this cell:

$$\begin{aligned} F(\mathbf{q}) &= \sum_j \int_{V'} \rho(\mathbf{r}_j + \mathbf{r}'_j) \cdot e^{i(\mathbf{r}_j + \mathbf{r}'_j) \cdot \mathbf{G}} dV' \\ &= \sum_j e^{i\mathbf{r}_j \cdot \mathbf{G}} \cdot \int_{V'} \rho(\mathbf{r}_j + \mathbf{r}'_j) \cdot e^{i\mathbf{r}'_j \cdot \mathbf{G}} dV'. \end{aligned} \quad (3.16)$$

The integral

$$f_j = \int_{V'} \rho(\mathbf{r}_j + \mathbf{r}'_j) \cdot e^{i\mathbf{r}'_j \cdot \mathbf{G}} dV' \quad (3.17)$$

is known as the atomic scattering factor.

The structure factor  $F(\mathbf{q})$  can therefore be expressed as

$$F(\mathbf{q}) = \sum_j f_j \cdot e^{i\mathbf{r}_j \cdot \mathbf{G}} \quad (3.18)$$

The structure factor and accordingly the intensity of the different reflections therefore depend on the atomic scattering factor of the different atoms in the unit cell as well as the positions of the atoms in the unit cell, which is the crystal structure. This property can be utilized during x-ray measurements of heterostructures, especially if the heterostructures contain materials with different crystal structures.

In the case of heterostructures containing the zincblende InP and (In,Ga)As as well as the half-Heusler NiMnSb materials, it is possible for certain reflections to attenuate the peaks of one layer, giving a clearer picture of the properties of the other layers.

The positions of atoms A and B in the zincblende unit cell is A:  $(0,0,0)$ ,  $(0, \frac{1}{2}, \frac{1}{2})$ ,  $(\frac{1}{2}, 0, \frac{1}{2})$  and  $(\frac{1}{2}, \frac{1}{2}, 0)$ , B:  $(\frac{1}{4}, \frac{1}{4}, \frac{1}{4})$ ,  $(\frac{1}{4}, \frac{3}{4}, \frac{3}{4})$ ,  $(\frac{3}{4}, \frac{1}{4}, \frac{3}{4})$  and  $(\frac{3}{4}, \frac{3}{4}, \frac{1}{4})$ . Together with equation 3.2 the structure factor of zincblende material can be calculated as:

$$\begin{aligned} F_{hkl} &= f_A \left( 1 + e^{-2\pi i(1/2k+1/2l)} + e^{-2\pi i(1/2h+1/2l)} + e^{-2\pi i(1/2h+1/2k)} \right) \\ &\quad + f_B \left( e^{-2\pi i(1/4h+1/4k+1/4l)} + e^{-2\pi i(1/4h+3/4k+3/4l)} \right) \\ &\quad + f_B \left( e^{-2\pi i(3/4h+1/4k+3/4l)} + e^{-2\pi i(3/4h+3/4k+1/4l)} \right) \end{aligned} \quad (3.19)$$

Due to the symmetry of  $F_{hkl}$ , there are only 4 different reflection types: 1. If  $(h,k,l)$  are not all either even or odd,  $F_{hkl}$  vanishes. The remaining 3 types are:

$$\begin{aligned}
2. \quad & (h+k+l) \bmod 4 = 0 \quad : \quad F_{hkl} = 4f_A + 4f_B; \\
3. \quad & (h+k+l) \bmod 2 = 0 \\
& (h+k+l) \bmod 4 \neq 0 \quad : \quad F_{hkl} = 4f_A - 4f_B; \\
4. \quad & (h+k+l) \bmod 2 \neq 0 \quad : \quad F_{hkl} = 4f_A + 4if_B;
\end{aligned} \tag{3.20}$$

Therefore independent of the atomic scattering factors of atom A and B, the reflections of type 2 and 4 will always be detectable. In case 3, however, if  $f_A = f_B$  like in the diamond-structure, these reflections cannot be measured. Even if  $f_A$  and  $f_B$  are very similar, like in the case of GaAs (see Table A.1), the intensity of a reflection of this type is very weak.

For the half-Heusler structure with atoms A, B and C at A:  $(0,0,0), (0, \frac{1}{2}, \frac{1}{2}), (\frac{1}{2}, 0, \frac{1}{2})$  and  $(\frac{1}{2}, \frac{1}{2}, 0)$ , B:  $(\frac{1}{4}, \frac{1}{4}, \frac{1}{4}), (\frac{1}{4}, \frac{3}{4}, \frac{3}{4}), (\frac{3}{4}, \frac{1}{4}, \frac{3}{4})$  and  $(\frac{3}{4}, \frac{3}{4}, \frac{1}{4})$  and C:  $(\frac{3}{4}, \frac{3}{4}, \frac{3}{4}), (\frac{3}{4}, \frac{1}{4}, \frac{1}{4}), (\frac{1}{4}, \frac{3}{4}, \frac{1}{4})$  and  $(\frac{1}{4}, \frac{1}{4}, \frac{3}{4})$  the structure factor calculates to:

$$\begin{aligned}
F_{hkl} = & f_A \left( 1 + e^{-2\pi i(1/2k+1/2l)} + e^{-2\pi i(1/2h+1/2l)} + e^{-2\pi i(1/2h+1/2k)} \right) \\
& + f_B \left( e^{-2\pi i(1/4h+1/4k+1/4l)} + e^{-2\pi i(1/4h+3/4k+3/4l)} \right) \\
& + f_B \left( e^{-2\pi i(3/4h+1/4k+3/4l)} + e^{-2\pi i(3/4h+3/4k+1/4l)} \right) \\
& + f_C \left( e^{-2\pi i(3/4h+3/4k+3/4l)} + e^{-2\pi i(3/4h+1/4k+1/4l)} \right) \\
& + f_C \left( e^{-2\pi i(1/4h+3/4k+1/4l)} + e^{-2\pi i(1/4h+1/4k+3/4l)} \right)
\end{aligned} \tag{3.21}$$

The structure factors and intensities for the half-Heusler crystal for the four different reflection types are then:

$$\begin{aligned}
1. \quad & F_{hkl} = 0; \\
2. \quad & F_{hkl} = 4f_A + 4f_B + 4f_C \\
3. \quad & F_{hkl} = 4f_A - 4(f_B + f_C) \\
4. \quad & F_{hkl} = 4f_A - 4i(f_B + f_C)
\end{aligned} \tag{3.22}$$

The intensity of the three different reflection types for InP, (In,Ga)As and NiMnSb, calculated with the atomic scattering factors from Table A.1, are shown in Table 3.1.

The intensity for the same reflection of type 3, like the (002) or (024) reflection, is a factor of 40 higher for NiMnSb than for  $\text{In}_{0.53}\text{Ga}_{0.47}\text{As}$ . Considering that the thickness of the (In,Ga)As layer is usually much larger than the one of the NiMnSb layer, the diffraction signal would be dominated by the (In,Ga)As layer if using reflections of type 2, like the (004) or type 4, like the (115) reflection. Thus, for experiments where information about the (In,Ga)As buffer is irrelevant or even disturbing the detection of the NiMnSb signal, reflections of type 3 are very useful.

Material	Intensity ratio		
	2	3	4
InP	0.80	18.10	1.00
In <sub>0.53</sub> Ga <sub>0.47</sub> As	1	1	1
NiMnSb	1.94	40.22	2.40

Table 3.1: Intensity ratios of the reflection types 2,3 and 4 of different crystals. The intensity of In<sub>0.53</sub>Ga<sub>0.47</sub>As is set to 1.

### 3.3 Reflective High Energy Electron Diffraction

The glancing-incidence-angle geometry of reflective high energy electron diffraction (RHEED) offers many advantages, since it is surface sensitive and allows for in-situ measurements during crystal growth. However, the glancing-incidence-angle requires special adaptations of the theoretical models to account for the symmetry breaking introduced by this geometry. For the diffraction of electrons in general the same rules as for the diffraction of photons mentioned in section 3.2 from crystals apply. For the case of RHEED, the electrons have a high kinetic energy in the range of 10 - 30 keV. Therefore the electrons have to be treated relativistically. The magnitude of the incident wave vector  $k_i$  is

$$k_i = \frac{1}{\hbar} \sqrt{2m_0E + \frac{E^2}{c^2}}. \quad (3.23)$$

The radius of the Ewald sphere of electrons with a typical energy is around  $800 \text{ nm}^{-1}$ , which is about 75 times larger than the reciprocal lattice of InP. This means that the Ewald sphere produces an almost planar cut through the first Brillouin zones of the reciprocal lattice. The surface component  $k_{i,z}$  of the incident wave vector lies in the neighborhood of 1000 eV, which is comparable to the values used for low energy electron diffraction (LEED) experiments. The sampling depth of RHEED is therefore very small. The periodic part of the crystal beneath the surface can thus be usually neglected and the reciprocal lattice becomes a set of one-dimensional rods along the z-direction perpendicular to the surface. Using this reciprocal lattice, the Ewald construction is shown in Fig. 3.6.

The reciprocal lattice consists of continuous rods, therefore every rod has an intersection with the Ewald sphere and thus producing a reflection in the diffraction pattern, which lie on so called Laue circles of radius  $L_n$  centered at H. The specular spot lies at the intersection of the zeroth-order Laue circle with the (00) rod. If a surface reconstruction is present, which produces a super-period, additional rods and therefore additional reflections in the diffraction pattern appear.

As shown above, the diffraction pattern of a perfect crystal obtained by a perfectly aligned electron beam consists of spots arranged in a circle. The electron

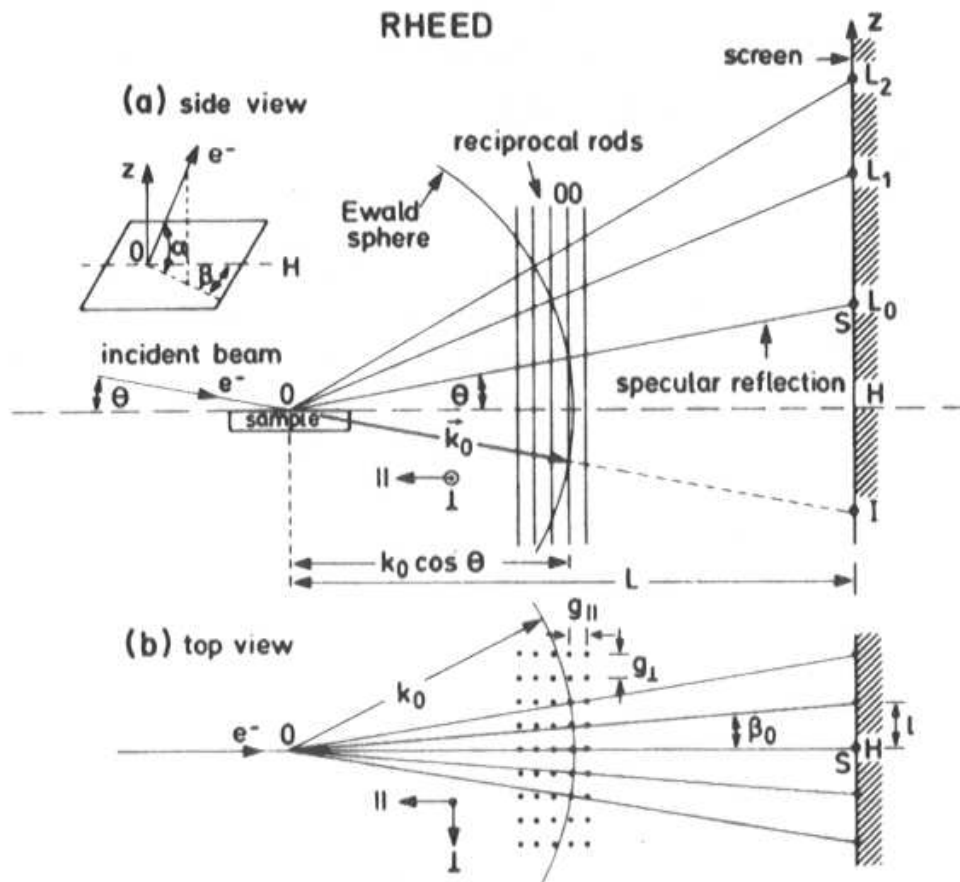


Figure 3.6: Ewald sphere construction and diffraction geometry of RHEED. Intensity maxima on the screen correspond to projected intersections of the Ewald sphere with the reciprocal lattice (from [Bra99]).

beam of a real experiment, however, always has some divergence and real crystals show some extent of steps at the surface. This results in an elongation of the spots along the direction of the rods. This pattern is often addressed as the “streaky” RHEED pattern observed during 2-dimensional MBE-growth. However, if there are some elevated structures on the surface, some electrons are transmitted through this material. The diffraction pattern shows then the 3-dimensional reciprocal lattice, consisting of spots which do not lie on the Laue circles any more, but are equidistant to each other (Fig. 3.7). Often the obtained RHEED pattern is a mixture between Fig. 3.7 b) and c).

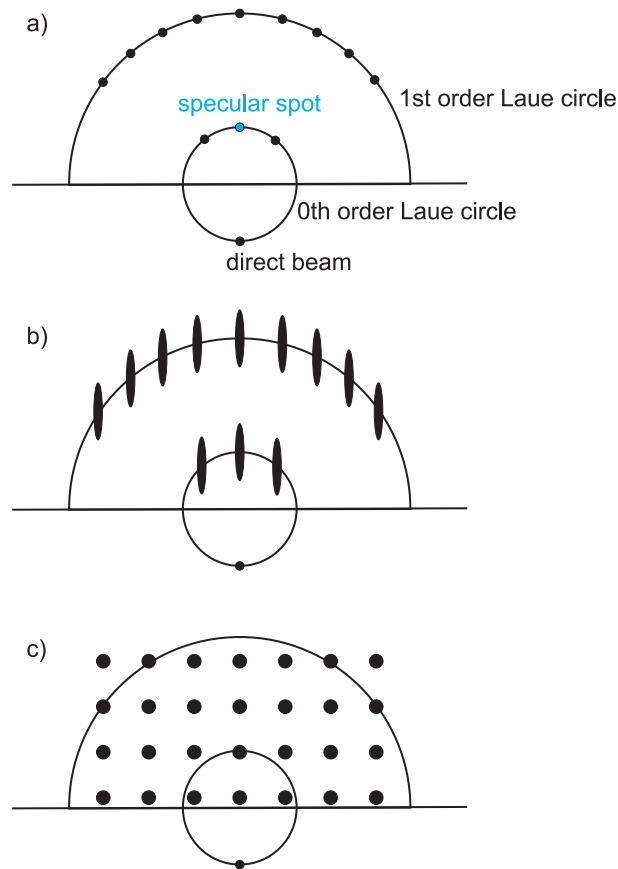


Figure 3.7: Schematic of RHEED patterns of different surface roughnesses. Part a) shows the pattern obtained by a perfect experiment for a perfectly flat surface, b) shows the RHEED pattern of a flat surface obtained by a realistic experiment, c) shows the RHEED pattern of a rough surface, caused by transmission of the electrons through parts of the crystal.

### 3.3.1 RHEED Oscillations

If the intensity of the specular spot during MBE-growth is monitored, often oscillations can be recognized. These RHEED oscillations can only be seen during the layer-by-layer growth mode. In this growth mode, the Frank-van der Merwe mode, one layer is essentially completed before material is added to the following layer. Therefore the appearance of the oscillations is often used for the determination of the growth mode. From RHEED oscillations several growth-parameters can be extracted. The period of the oscillations gives access to the growth rate, while the damping provides information about the roughness of the layer. The damping can be interpreted as an increase of long-range roughness that approaches a steady state in the limit of totally damped oscillations. In con-

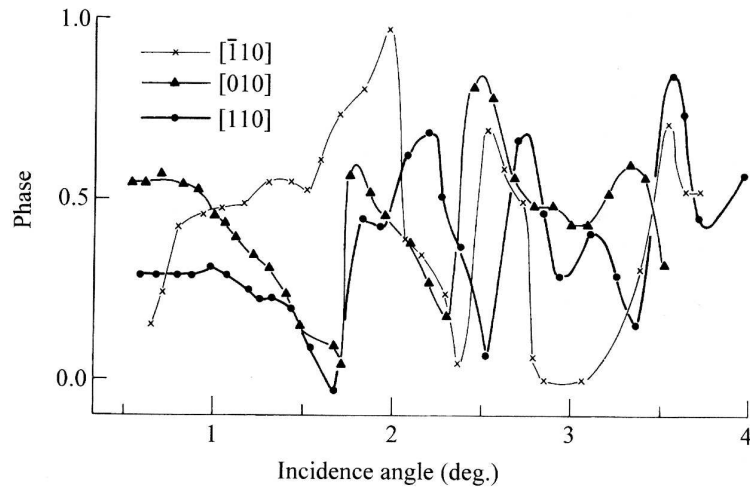


Figure 3.8: Phase of RHEED oscillations during GaAs-growth as a function of incidence angle and azimuth. The phase is defined by the position of the second minimum, measured from the growth start (from [Zha87]).

trast, the roughness variation responsible for the RHEED oscillations constitute a high-frequency component that depends on the position within a ML growth cycle [Bra99]. Factors influencing the long-range roughness are for example the flux-homogeneity over the sample and the sample temperature.

Whereas the correlation of the period of RHEED oscillations with the growth of one ML is experimentally well established, a direct connection between the surface roughness and the RHEED intensity cannot be found. Fig. 3.8 shows an example of the phase of RHEED oscillations depending on the growth conditions. The phase is clearly a complicated function depending on the azimuth as well as the incident angle of the probing electron beam. The trivial picture, where the intensity of the RHEED specular spot is directly correlated to the roughness of the surface cannot be supported. To account for this phase variation during RHEED oscillations, various theoretical approaches were developed. A detailed description of these theories can be found in [Bra99].

# Chapter 4

## Growth of NiMnSb on (001) Oriented Materials

### 4.1 Substrate and Buffer Materials

Epitaxial growth of NiMnSb on conventional semiconductors is possible due to the strong similarity of the half-Heusler and the zincblende crystal structure. First epitaxial growth of NiMnSb films on a semiconductor (in this case GaAs) has been demonstrated by van Roy [Roy00]. The lattice constant of NiMnSb is in the range between 5.90 Å and 5.95 Å depending on the growth method and the exact stoichiometry of the NiMnSb crystal. For optimum quality of the NiMnSb layers, these layers have to grow in the absence of misfit dislocations, which evolve if the lattice constant of the substrate crystal is far off the lattice constant of NiMnSb. Hence, the substrate crystal has to have minimum lattice mismatch to NiMnSb. The best commercially available choice is InP, which has a lattice constant of 5.8687 Å. In contrast to GaAs, which was the first semiconductor NiMnSb was grown on, the lattice mismatch of NiMnSb to InP is less than 1%. This provides the possibility to grow fully strained NiMnSb layers on top of InP.

### 4.2 Substrate Preparation

Commercially available, so called *epi-ready* InP substrates come with an oxide layer to protect the sensitive semiconductor surface. This oxide layer has to be removed before growth on the substrate can take place. Furthermore, during the attaching of the substrate on the molybdenum-block and the insertion into the UHV system, the substrate surface may be covered with organic residues and water. These substances have to be removed before the sample can enter the growth chamber. This is done by heating the sample to 250°C for 10 minutes in a

closed part of the UHV system to avoid contamination of the rest of the system.

But the choice of InP as the substrate material also has a drawback. Since the surface quality of InP after desorption is bad due to the formation of In droplets at the degassing temperature, a buffer layer is needed. The element P, however, is highly reactive and has a high vapor pressure. The use of P in a standard MBE system also used for As and Sb based semiconductors is therefore not recommendable. In the available MBE-systems there is no P-source to grow the binary compound InP. Therefore a substitute has to be found which can be used to protect the sensitive InP surface after the desorption of the oxide layer.

Since we can grow As and Sb based III-V materials in this MBE-chamber, the ternary semiconductor (In,Ga)As was used. It can be grown lattice matched to InP with a ratio of  $\text{In}_{0.53}\text{Ga}_{0.47}\text{As}$ . The standard procedure therefore consists of 3 main parts: First, desorption of the InP oxide layer, second, growth of the (In,Ga)As buffer layer and finally the growth of the NiMnSb layer.

For the last part a separate growth chamber is used, since remaining As from the buffer growth can induce MnAs inclusions into the NiMnSb layer which act as centers where defects can nucleate [Roy00].

### 4.3 Growth (In,Ga)As on InP(001)

The growth on InP substrates has several challenges. The standard desorption technique for epi-ready III-V substrates involves group V stabilization with the element used in the substrate. Since in our MBE-system a Phosphorous source is not available, a different element has to supply the desired group V stabilization pressure. This is done most easily using Arsenic since this element is closest to Phosphorous in the periodic table. The problem using As during the desorption is that forming a thin coverage of InAs due to a replacement of P with As cannot be ruled out easily. A further problem occurs if the As background pressure is not efficient enough to suppress P evaporation. In this case liquid In droplets form at the surface, which act as defect nucleation centers during the growth of the buffer layer. This kind of defects can be observed as oval defects (Fig. 4.1). Secondary Ion Mass Spectroscopy (SIMS) measurements of samples with a too long desorption time show a significant increase of the In content in the sample at the interface between (In,Ga)As buffer and NiMnSb layer (Fig. 4.2).

Since the evaporation rate of P strongly depends on the surface temperature, a very good control of the desorption temperature and desorption time has to be achieved in order to avoid evaporation of P. One particular property of the epi-ready InP substrates helps to control these parameters: In contrast to As-containing III-V substrates, the oxide layer forming on InP is not amorphous but shows crystalline ordering at the surface. This ordering can be detected by *in situ*



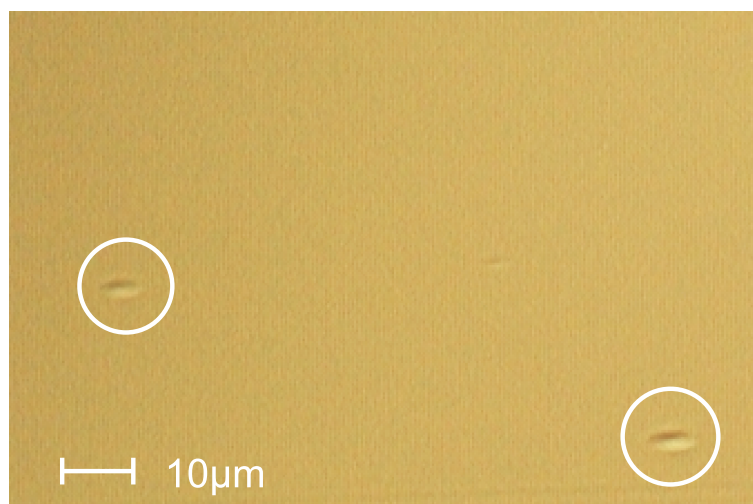


Figure 4.1: Image of the surface of a lattice matched (In,Ga)As buffer on InP taken by a Nomarski interference contrast microscope. Two oval defects are marked.

RHEED measurements (Fig. 4.3) and can be clearly distinguished from the group V rich InP RHEED pattern (Fig. 4.4).

Thus, the appearance of the uncovered InP RHEED pattern is an indication that the desorption of the oxide layer is almost completed. This effect can be used to calibrate the readings of the pyrometer and the thermoelement at the backside of the Mo-block. These readings usually fluctuate from growth to growth due to changes in the heat flow from the filament to the substrate. This is mainly influenced by the amount of In used for attaching the substrate to the Mo-block and by the thickness and surface roughness of the Mo-block itself. Since after each growth process the Mo-blocks are cleaned by etching and degassing, over time some Mo is carried off and the Mo-layer underneath the substrate gets thinner and rougher.

The best recipe to desorb the oxide layer from the substrate is as follows (temperatures mentioned are thermocouple readings):

- heat the substrate at 20K/min to 10K above the InP desorption temperature (typically 540°C)
- above 350°C deploy an  $\text{As}_4$  flux of  $1\text{-}2 \times 10^{-5}$  torr
- immediately cool down to 10K below InP desorption temperature (typically 520°C) at 15K/min
- wait at this temperature for 30 s to let the substrate temperature stabilize
- open In and Ga Shutter simultaneously to start the growth of (In,Ga)As

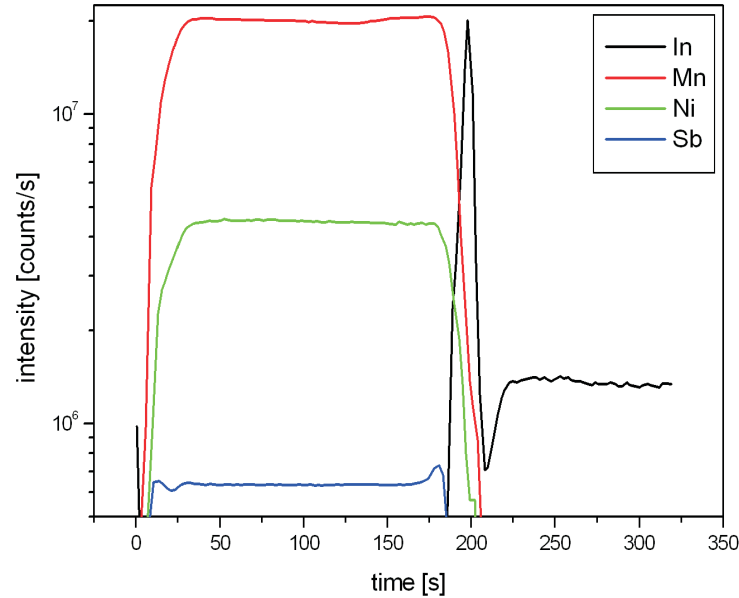


Figure 4.2: SIMS measurement of a sample consisting of a NiMnSb layer on an (In,Ga)As buffer layer. The materials Ni, Mn, Sb and In were monitored. Note that at the time corresponding to the interface between these layers (200s) the In content in the sample shows a sharp peak, indicating that an excess amount of In is incorporated in this part of the sample.

Usually 5 to 10 s after the growth start the (2x4) InP RHEED reconstruction disappears. Since the growth start is very sensitive on the desorption temperature, in the first 2 or 3 minutes of (In,Ga)As growth RHEED measurements can show signs of surface roughness (Fig. 4.5). But after this time a 2D (4x2) reconstruction with a weak fourfold pattern should have been appeared (Fig. 4.6). Signs of too high growth temperature are times above 20 s before the (In,Ga)As reconstruction appears, sign of too low growth temperature is a very pronounced 3D pattern directly after the opening of the In and Ga shutters.

Since the main goal for the (In,Ga)As layer is the protection of the InP, the buffer layer should have the same lattice constant as InP which ensures minimum influence of the (In,Ga)As on successive growth procedures. With 53% of In and 47% of Ga atoms in the (In,Ga)As layer this can be achieved. In the corresponding flux ratio the different ionization probabilities of In and Ga have to be taken into account as well as the different sticking probabilities on the substrate surface. In the case of (In,Ga)As growth, the substrate temperature is high enough that the In sticking probability can drop below 1. Therefore not only the flux ratio of In/Ga but also the substrate temperature during growth affects the composition

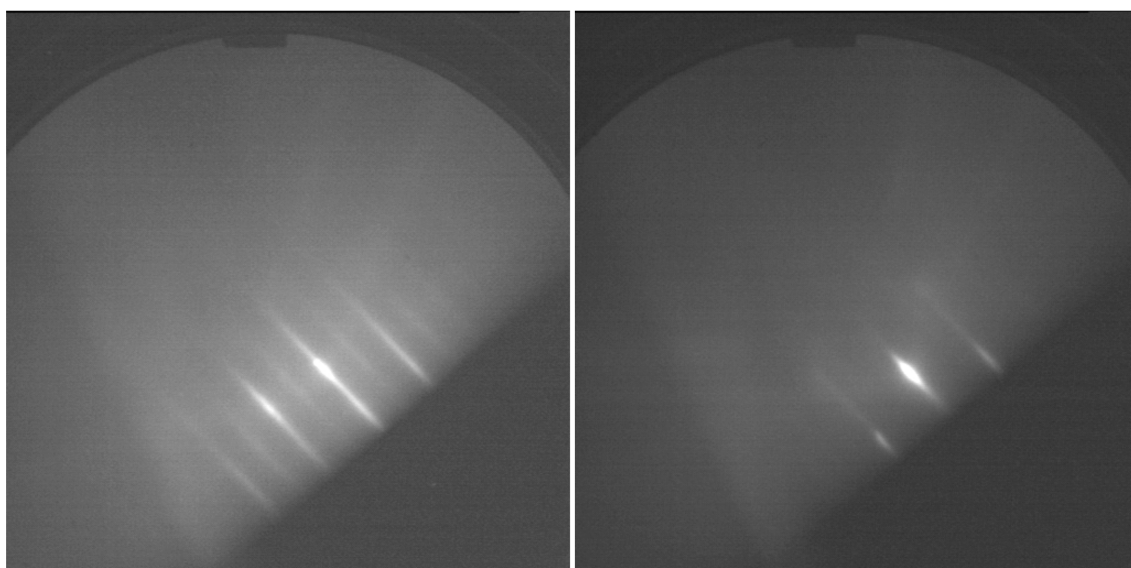


Figure 4.3: RHEED measurement of the (4x2) reconstruction of an InP wafer covered with an oxide layer at a temperature of 500°C. The left picture along [110] shows a very pronounced d/2 streak while in the right picture along [1 $\bar{1}$ 0] the d/4 streaks are very weak.

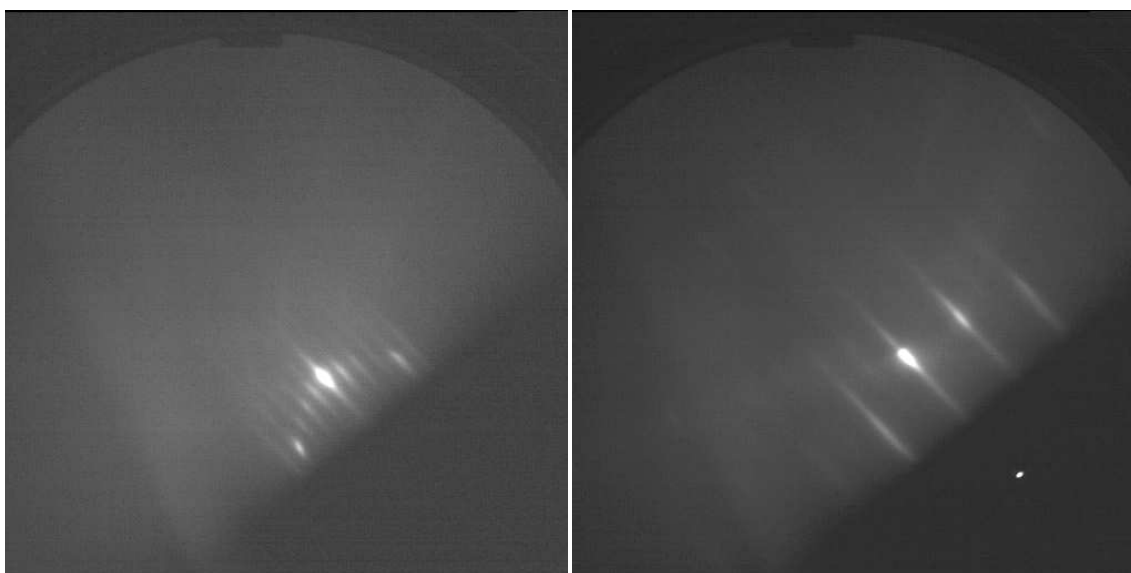


Figure 4.4: RHEED measurement of the (2x4) reconstruction of As stabilized InP at 530°C. The left picture along [110] shows very clear d/4 streaks. In the right picture along [1 $\bar{1}$ 0] the d/2 streak is also easily visible.

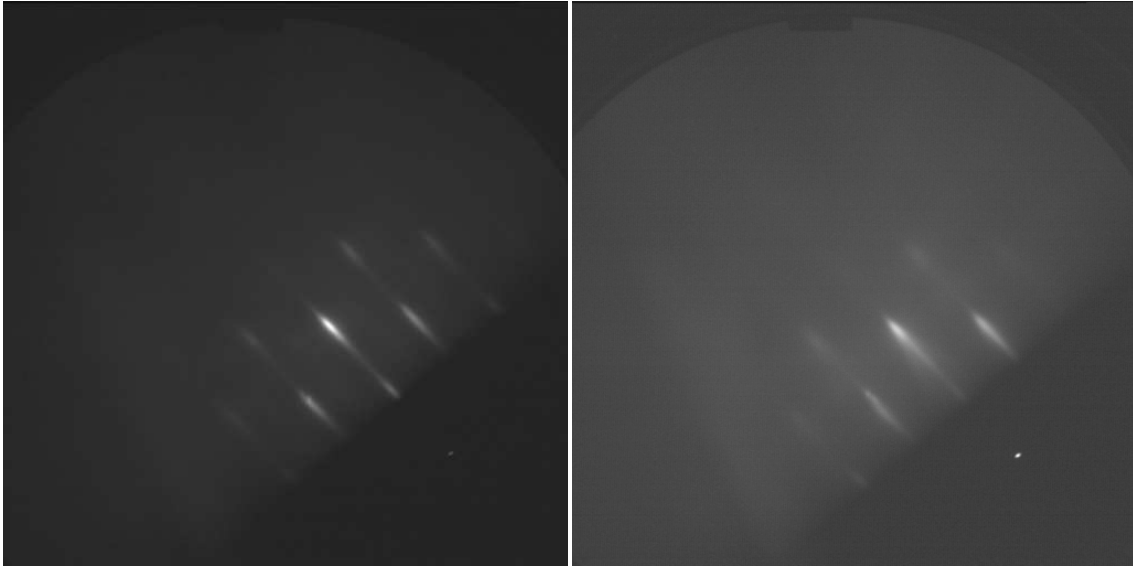


Figure 4.5: RHEED measurement of a suboptimal growth-start of (In,Ga)As on InP. In  $[110]$ (left) as well as in  $[1\bar{1}0]$  pronounced surface roughness is visible.

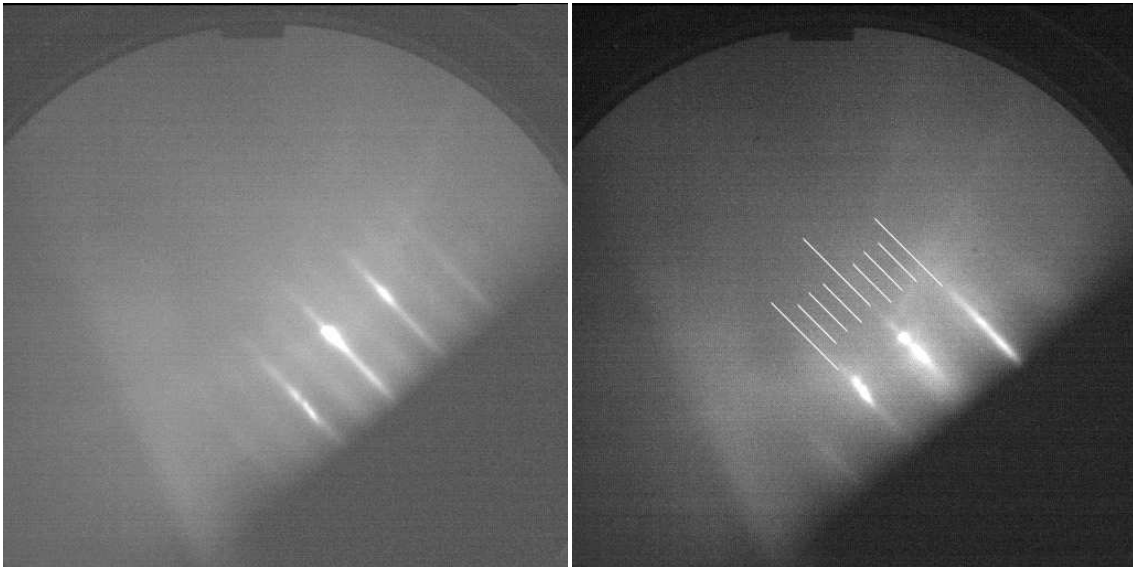


Figure 4.6: RHEED measurement of the  $(2\times 4)$  reconstruction of (In,Ga)As on InP during growth at  $520^\circ\text{C}$ . In  $[110]$ (left) the  $d/2$  streaks are clearly visible, in  $[1\bar{1}0]$  the positions of the very weak  $d/4$  streaks are marked.

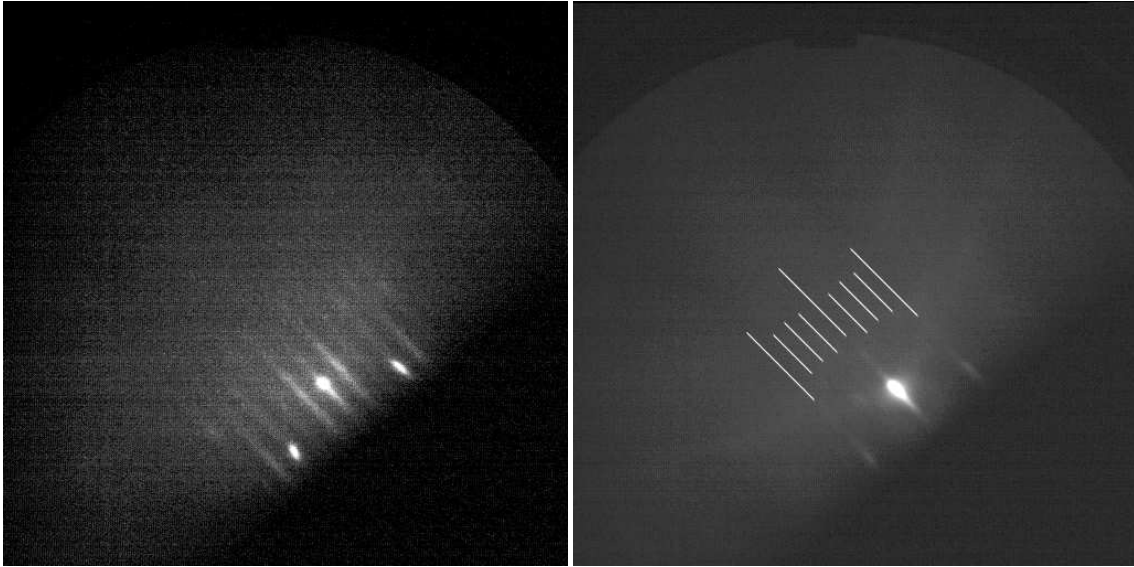


Figure 4.7: RHEED measurement of the (4x3) reconstruction of (In,Ga)As on InP during cooldown under As background pressure. Along  $[1\bar{1}0]$ (left) the d/3 streaks are clearly visible, along  $[110]$ (right) the positions of the weak d/4 streaks are marked.

of the buffer layer. Usually a In/Ga ratio of 2.8/1 is necessary to achieve lattice matched growth of (In,Ga)As on InP. The group III/V flux ratio for the (In,Ga)As growth is not crucial, as long as the As flux is high enough to stay in the As-rich regime. Since for the desorption of the InP oxide a very high As flux is needed, it is convenient to use this high As overpressure (III/V ratio:  $\sim 0.04$ ) for the growth, too.

During the cooling process after the growth the As supply has to be sustained above a temperature of  $350^\circ\text{C}$  to prevent P and As desorption from substrate and buffer. Below  $480^\circ\text{C}$  the (2x4) reconstruction changes to a (4x3) reconstruction (Fig. 4.7). LEED measurements prove the (4x3) reconstruction (Fig. 4.8).

#### 4.4 Growth of NiMnSb on InP(001)

As mentioned in section 4.3 the growth of the NiMnSb layer has to take place in a different growth chamber as the III/V buffer. For this task a MBE-system built by MBE-Komponenten GmbH was used. Since both chambers are connected by a UHV transfer system, transport of the samples between the different chambers without breaking the UHV is possible.

One challenge in growing NiMnSb is due to the fact that stoichiometric

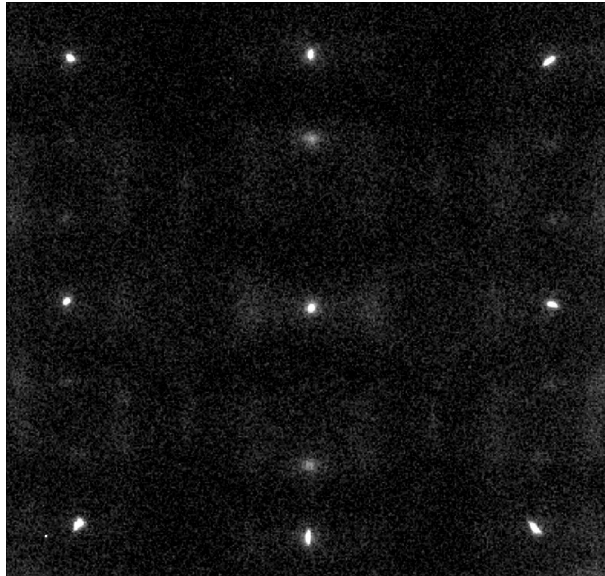


Figure 4.8: LEED measurement of (In,Ga)As on InP at room temperature taken with an electron energy of 50 eV.

growth is very difficult. Many materials like most widely used III-V and II-VI semiconductors have the behavior of growing in a self-limiting mode. This means that for example in III/V semiconductors the flux ratio of the supplied atoms does not affect the ratio of III/V atoms in the grown crystal. If an excess of group V is supplied, only a fraction of this material is built into the crystal. The rest is desorbed from the substrate surface. The same applies if an excess of group III material is supplied. In this case only a part of the group III atoms at the surface is incorporated. Therefore no matter what flux ratio is supplied the III/V ratio in the crystal is always 1/1.

Unfortunately NiMnSb does not show this feature. Hence, a very good control over the fluxes of the different materials is necessary. Since the stoichiometry of the grown layer has to stay constant during growth it is indispensable that the fluxes of the three materials are constant during growth. Due to the chamber geometry the evaporation rate depends on the shutter position directly in front of the orifice of the effusion cell. If the shutter is closed, the temperature inside the cell tends to be slightly higher than if the shutter is in the opened position. This means that for a straight forward growth procedure the stoichiometry will change during the growth process. To ensure that all cells provide a time independent flux during growth, the cell shutters are opened well before growth takes place. The main-shutter, which sits directly in front of the substrate, is close enough to the substrate surface to efficiently shield the sample surface from any incoming molecules from the effusion cells. Typically after a time of 3 minutes all cells

exhibit a constant flux and the growth can be started by opening the main-shutter.

This behavior of the effusion cell makes growth starts where the interface is controlled by successive opening of the different material shutters difficult. Experiments where the exact crystal stoichiometry was secondary and attention was paid to the growth start showed that a sole Sb flux onto the (In,Ga)As buffer has no effect, a sole Ni flux leads to a decay of the surface quality after some seconds and a sole Mn flux immediately leads to a pronounced surface roughening on which subsequent growth shows earlier relaxation and lower crystal quality. A growth start where all three elements are opened simultaneously gives best results in terms of crystal quality and critical thickness.

Furthermore, the sticking coefficient of the Ni, Mn and Sb have to be taken into account. In general, these coefficients are dependent on the temperature of the sample surface. In our case in a large temperature range between room temperature and 400°C the sticking coefficient of Mn and Ni are very close to 1. In the case of Sb this is different. Sb is evaporated in  $Sb_4$  molecules which have to dissociate on the sample surface before they can be incorporated into the NiMnSb lattice. The reevaporation rate of undissociated  $Sb_4$  molecules rises with higher substrate temperature. Therefore with higher substrate temperature the amount of Sb in the grown NiMnSb crystal gets less. To compensate for this effect a larger Sb flux at higher substrate temperatures is needed.

To check for optimum growth several parameters have to be taken into account. Of course the flux ratios of the three materials but also substrate temperature and in a somewhat lesser extend the growth rate influences the stoichiometry and crystalline quality of the samples. All of these parameters are highly correlated so a four-dimensional parameter field has to be examined to find the optimum growth conditions.

#### 4.4.1 Flux Ratios

Several structural properties of NiMnSb depend on the exact concentration of the different materials inside its lattice. To examine the best growth conditions a set of 9 samples with different Mn/Ni and Sb/Ni flux ratios have been grown. The substrate temperature is set constant at 250°C and the Ni flux is not changed to get nearly the same growth rate for each NiMnSb crystal. Fig. 4.9 gives an overview of the grown samples for this experiment.

During growth different reconstructions and surface qualities are measured by RHEED. Table 4.1 describes the observed RHEED measurements for the different samples.

From the RHEED observations sample H124 shows the best growth characteristics, with 2-dimensional surface during the whole growth time and no signs

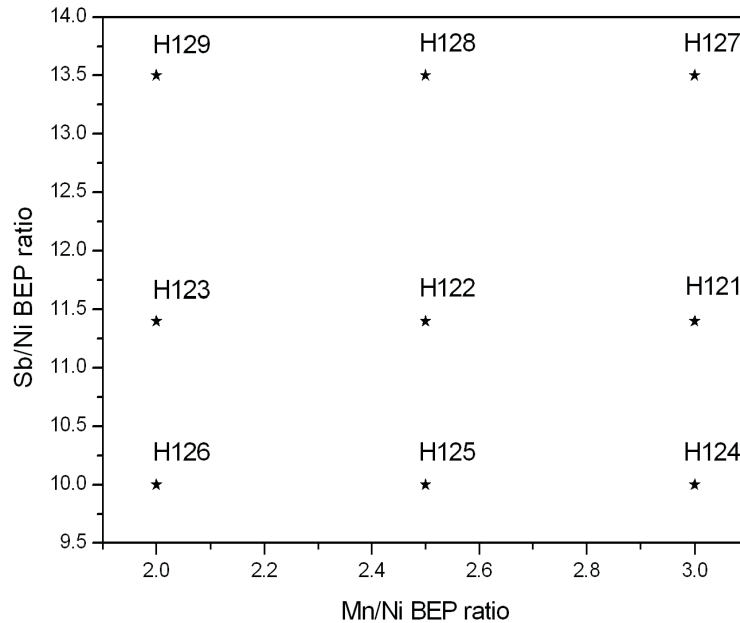


Figure 4.9: Overview of the samples and flux ratios.

of relaxation in the layer.

To check for the crystalline quality of the NiMnSb layer, all samples are characterized by HRXRD  $\theta - 2\theta$  measurements. To characterize the NiMnSb crystal the (002) reflection is used. As pointed out in section 3.2.3, this reflection has a low scattering factor for the (In,Ga)As buffer. This is useful in this case since the prominent (In,Ga)As peak and thickness oscillations make the analysis of the weaker NiMnSb signals difficult. This is especially true for NiMnSb with suboptimal structural quality.

Figs. 4.10, 4.11 and 4.12 show the HRXRD  $\theta - 2\theta$  scans of the samples in this series. It is apparent that the different stoichiometries result in different vertical lattice constants for each sample. The general tendency is that with increasing Mn/Ni and decreasing Sb/Ni ratio the lattice constant gets larger.

To check for the crystalline quality the mosaicity of the different NiMnSb samples has been determined by measuring the rocking curves of the NiMnSb peak. Surprisingly all samples show a very low mosaicity, which lies in the same range as the one of the substrate, varying from 12 to 15 arcsec. Since relaxation of the stressed NiMnSb layer would definitely increase the mosaicity, this process can be excluded.

Since the different NiMnSb layers all have the same mosaicity and the approximate same thickness, the ratio of the intensities in the  $\theta - 2\theta$  scans of NiMnSb layer to substrate should be the same. As can be seen clearly in the scans this is



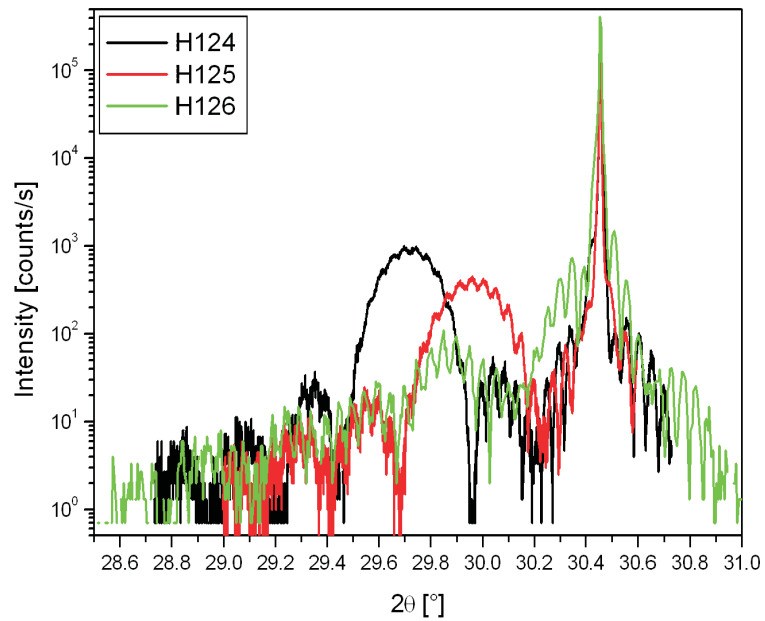


Figure 4.10: HRXRD  $\theta - 2\theta$  scans of the (002) reflection of the samples H124, H125 and H126.

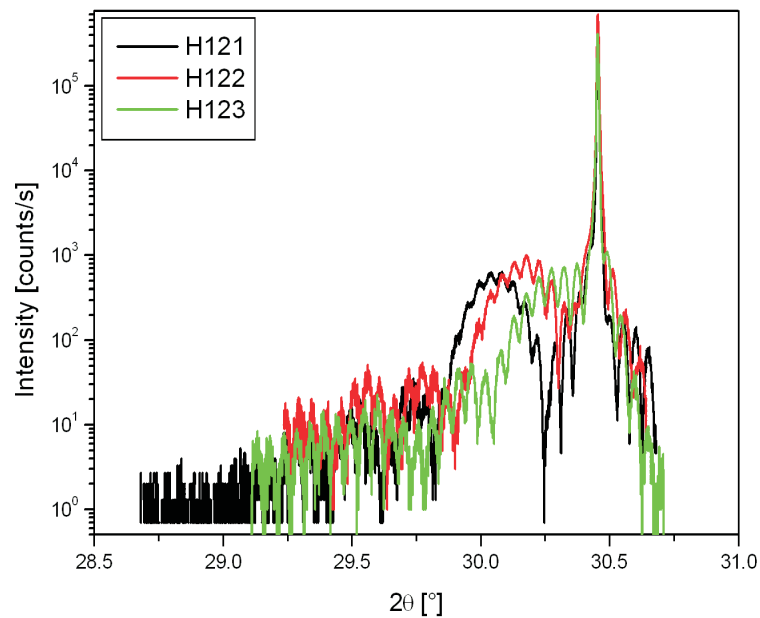


Figure 4.11: HRXRD  $\theta - 2\theta$  scans of the (002) reflection of the samples H121, H122 and H123.

sample	flux ratios		RHEED observation
	Mn/Ni	Sb/Ni	
H121	3.0	11.4	(5x5) reconstruction and rough surface
H122	2.5	11.4	(1x5) reconstruction, very rough surface
H123	2.0	11.4	(5x5) reconstruction, very rough surface
H124	3.0	10.0	(2x1) reconstruction, no signs of surface roughness or relaxation
H125	2.5	10.0	(2x2) reconstruction, slight surface roughening
H126	2.0	10.0	(2x1) reconstruction, signs of atomic disorder
H127	3.0	13.5	(5x5) reconstruction, rough surface
H128	2.5	13.5	unreconstructed, rough surface
H129	2.0	13.5	unreconstructed, very rough surface

Table 4.1: RHEED observations during the growth of NiMnSb with different flux ratios

not the case. The highest intensity for the NiMnSb peak can be found for H124, the sample which also showed the best growth behavior as measured by RHEED. All other samples show a reduced intensity. Since the amount of material and the mosaicity is the same for all samples this means that suboptimal growth results in chemical disorder in the lattice. The disordered atoms do not take part in the x-ray scattering process. This means that these atoms are either randomly distributed or form some other crystal structure that does not have lattice plains parallel to the (001) plains in the NiMnSb crystal. Candidates for these types of crystalline inclusions are NiSb, NiMn and MnSb which all crystallize in a hexagonal structure with the c-axis parallel to the [111] direction of NiMnSb [Roy00]. These inclusions can easily be seen by measuring  $\theta - 2\theta$  scans of NiMnSb grown on (111) oriented substrates. The absence of these inclusions for the used growth conditions will be shown in section 8.3.2.

Further criteria for the quality of the crystal growth are the number and intensity of the thickness oscillations since they are directly depending on the uniformity of the crystal and smoothness of the interfaces and surface. The most prominent oscillations can again be detected for H124. The oscillations tend to get weaker for an increased Sb/Ni ratio, while the Mn/Ni ratio only plays a minor role for this feature. For the samples of the maximum Sb/Ni ratio (H127, H128 and H129) the thickness oscillations can only be guessed at.

The surface reconstruction during growth is depending on the exact stoichiometry of the grown material. Directly after the growth start independent of the flux ratios a (2x1) reconstruction is arising. After typically 2 nm this can change into a different reconstruction ranging from (1x1) to (5x5). Notably only

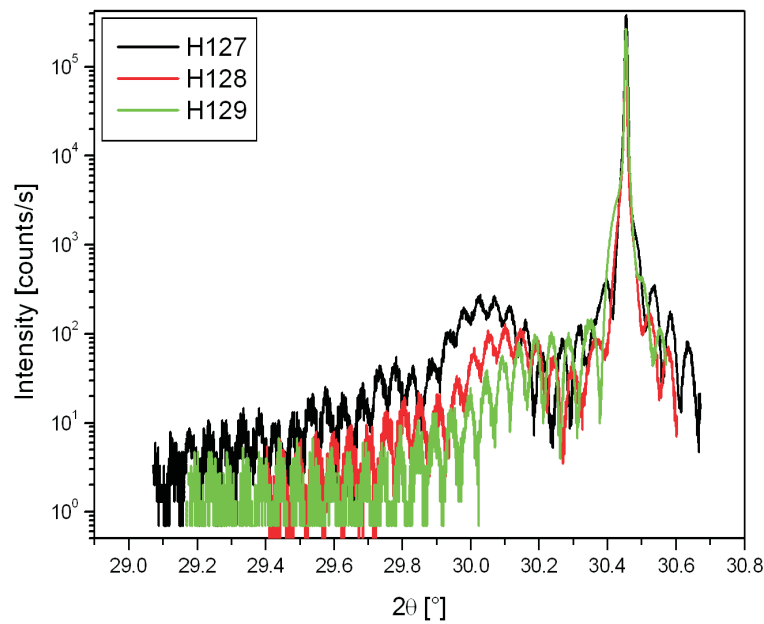


Figure 4.12: HRXRD  $\theta - 2\theta$  scans of the (002) reflection of the samples H127, H128 and H129.

the (2x1) and in a lesser extend the (3x1) reconstruction seem to be stable. All other reconstructions change during growth and end up with a very rough unreconstructed surface after 15-20 nm. Best crystalline quality is achieved if the samples grow with a (2x1) reconstruction during the whole growth (Fig. 4.13).

#### 4.4.2 Substrate Temperature

In contrast to many other full- or half-Heusler compounds [Her03] for NiMnSb there is a fairly large substrate temperature range where epitaxial growth occurs. From room temperature to 400°C NiMnSb is growing in a 2-dimensional growth mode but with different surface and crystal qualities.

At room temperature, RHEED measurements show a broadening of the reconstruction streaks, which indicates a large atomic disorder at the surface. HRXRD measurements confirm the reduced crystal quality in comparison to samples grown at 250°C. Samples grown at 400°C show inclusions of some other crystalline phase in RHEED measurements. Since the Sb integration is drastically decreased at higher substrate temperature these inclusions may well be NiMn crystallites which crystallize in a hexagonal structure. Increased Sb supply at these higher temperatures decrease the amount of inclusion formation but can not prevent this effect entirely. From 200°C to 300°C NiMnSb can grow in a nearly

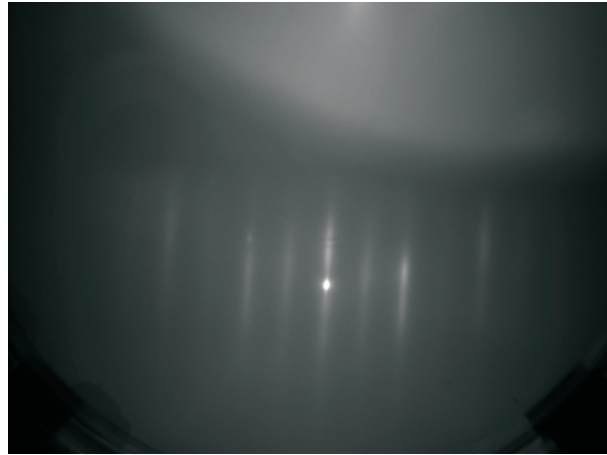


Figure 4.13: RHEED measurement of a NiMnSb(001) surface after growth of 10 ML along [110]. The  $d/2$  streaks are well defined and the specular spot is very sharp.

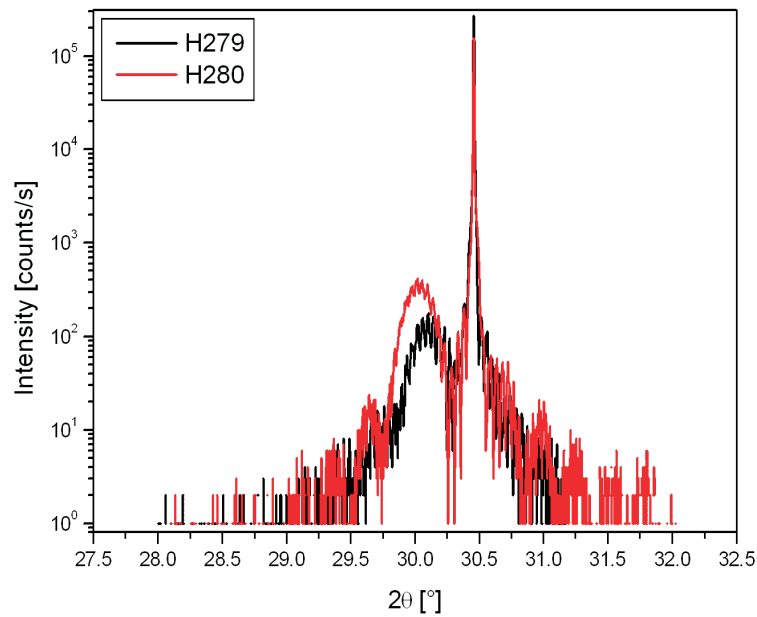


Figure 4.14: HRXRD  $\theta-2\theta$ -scan of the (002) reflection of H279 and H280. Whereas both samples were grown with identical flux ratios, the substrate temperature of H279 was 300°C and of H280 200°C. Both samples show high crystalline quality with numerous thickness oscillations.

optimum quality (Fig. 4.14) if the Sb content is adjusted to the respective substrate temperature. The substrate temperature used for standard growth was set in the middle of this range, at 250°C.



# Chapter 5

## Structural Properties of NiMnSb (001)

The structural properties of a material drastically influence its behavior in electric or magnetic experiments. Structural properties can be divided into two parts, the properties of the bulk structure or crystalline properties and the properties of the surface. The surface properties during the growth process, however, have an effect on the bulk properties of the grown sample and on the growth process and quality of any successive layer.

### 5.1 Surface Properties

The surface of NiMnSb layers was characterized using RHEED oscillations, spot-profile analysis low-energy electron diffraction (SPA-LEED) measurements and by examining the thickness fringes measured in HRXRD  $\theta - 2\theta$  scans.

#### 5.1.1 RHEED Oscillations

For the growth of homogeneous and smooth layers on direct (001) substrates, 2-dimensional growth modes are optimal for the crystalline quality. To determine the growth mode, measuring the intensity of the RHEED specular spot is essential since the 2-dimensional Frank-Van der Merwe mode manifests itself in intensity oscillations of the specular spot.

Fig. 5.1 shows the obtained intensities for NiMnSb growth. From these oscillations the growth mode can be determined to be Frank-Van der Merwe. The growth rate can be directly calculated from the frequency of the oscillations. The value of 0.073 ML/s or 0.216 Å/s is in good agreement with the HRXRD thickness calibrations. Remarkably, the intensity and amplitude of the oscillations critically

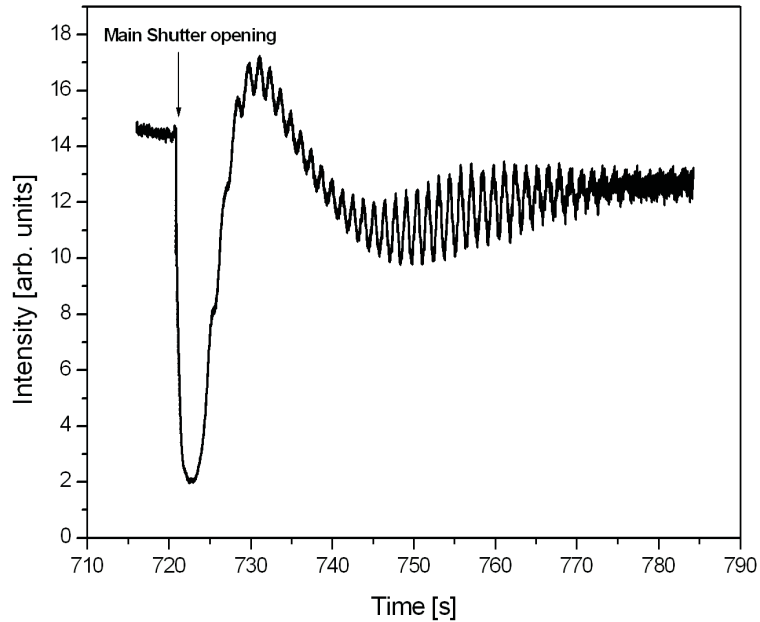


Figure 5.1: Intensity of the specular spot in  $[1\bar{1}0]$  direction during the growth of NiMnSb. The oscillations appear directly after the beginning of the growth. At first they are superposed by a weakening of total intensity caused by the initial roughening of the surface due to interface reactions. The oscillations are very stable, 42 ML ( $\sim 12$  nm) can be counted until the oscillations disappear, which is a good value comparable with those of standard III-V semiconductors [Bra99]. Note that the thickness at which the oscillations are blurring is coinciding with the start of relaxation processes in NiMnSb as shown in section 5.2.1.

depend on the direction of the electron beam. Best results are obtained in the  $[1\bar{1}0]$  direction, whereas in the  $[110]$  direction the oscillations are weaker and are blurring earlier.

To measure RHEED oscillations the rotation of the substrate during growth has to be stopped. Therefore not only the growth characteristics of the material but also the homogeneity of the fluxes over the area of the substrate determine the quality and number of oscillations. In our growth chamber we obtain excellent numbers for these values. This means that not only the growth of NiMnSb is very good but also the homogeneity of the three different material fluxes is good. This is especially noteworthy since the orifice of the Ni cell is small compared to the other standard effusion cells and therefore the homogeneity of Ni flux on the sample can be expected to be reduced.



### 5.1.2 Spot Profile Analysis of Low-Energy Electron Diffraction

SPA-LEED measurements give access to several properties of the NiMnSb surface which cannot be obtained by RHEED measurements. If the surface is well defined, the profile of the specular spot can show characteristic features from which terrace size and step-height on the surface can be extracted (Fig. 5.2). Details on the principles and methods used for SPA-LEED measurements can be found in [Hor99].

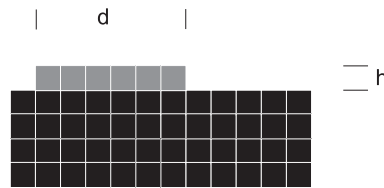


Figure 5.2: Illustration of the terrace size  $d$  and step-height  $h$  on a surface during or after growth.

The typical (2x1) reconstructed surface was examined by SPA-LEED after the growth of 10 ML of NiMnSb. The diffraction pattern shows sharp diffraction spots from the (2x1) reconstruction (Fig. 5.3). Fig. 5.4 shows the energy dependence of the specular spot profile. [110]-line-scans were measured at different energies, background corrected and normalized to their maximum individually. A step-induced broadening of the specular spot is clearly visible at 53 eV, 88 eV and approximately 130 eV (just outside of the investigated energy range). These values correspond to  $k$ -vectors of  $7.4 \text{ \AA}^{-1}$ ,  $9.6 \text{ \AA}^{-1}$  and  $11.7 \text{ \AA}^{-1}$ , respectively, and represent anti-phase conditions for a surface with steps of a height of  $2.94 \text{ \AA} = a_0/2$ . At  $k$ -vectors corresponding to the  $a_0/4$  step height no broadening can be detected. The average terrace size obtained by these measurements is  $250 \text{ \AA}$ , which is a good value compared with standard II-VI materials [Neu97], which grow at the same substrate temperature.

### 5.1.3 HRXRD Thickness Fringes

As mentioned previously in section 3.2.2, the Pendellösung fringes obtained during a HRXRD  $\theta - 2\theta$  scan are solely depending on the thicknesses and uniformity of the different layers and the roughnesses of the interfaces in between. Therefore the existence and clarity of these fringes are good indicators for optimum surface quality. Especially pseudomorphic and relaxed layers can be distinguished by examining the thickness fringes, since the surface roughness caused by the defects induced by the relaxation process usually prevents the appearance of the fringes. HRXRD scans including the thickness fringes can be simulated using the dynamic

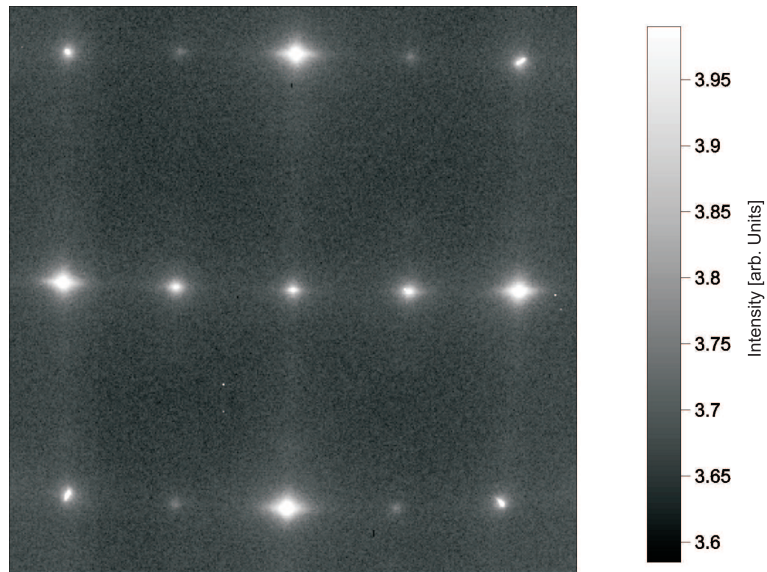


Figure 5.3: Two-dimensional LEED pattern of the NiMnSb-(2x1) surface taken at an electron energy of 75 eV.

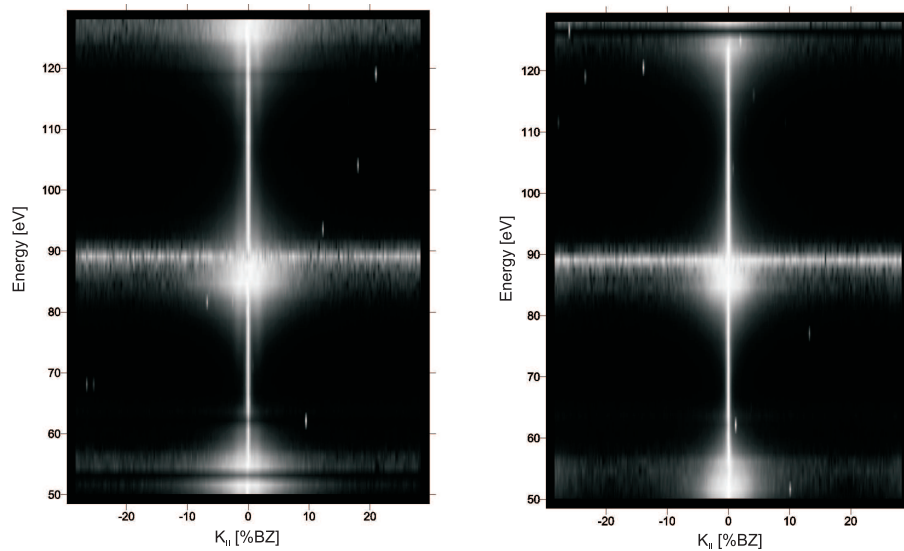


Figure 5.4: Line-scans of the specular spot of the NiMnSb-(2x1) surface, taken along the  $[110]$  (left) and  $[1\bar{1}0]$  (right) direction at different electron energies. (Note that each of the scans is normalized to its individual maximum.)

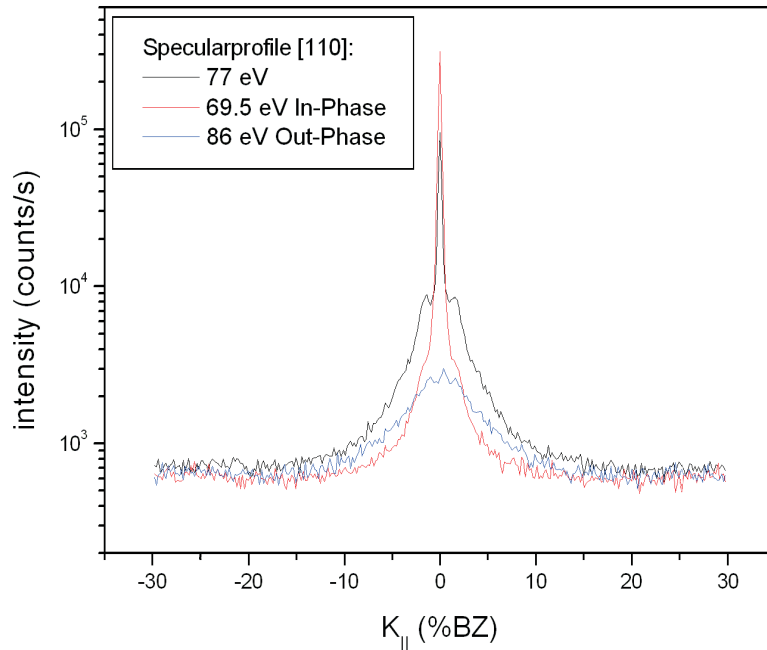


Figure 5.5: SPA-LEED spot-profiles of the NiMnSb-(2x1) surface of the specular spot taken at different electron energies along the [110] direction.

theory published in [Few87]. The fit procedure assumes perfect surfaces and interfaces, i.e. an interface and surface roughness of zero. Comparisons between the measured data and the fitted graph can give a hint on how far the sample surfaces and interfaces are from being perfect. Fig. 5.6 shows a HRXRD scan of a sample consisting of a 70 nm NiMnSb layer on a 150 nm (In,Ga)As buffer layer. For the (In,Ga)As as well as for the NiMnSb layer clear thickness fringes can be observed. Additionally, this graph is showing a very good agreement between the measured and the simulated data, indicating that the surface and interface roughnesses in this sample are very close to zero. For comparison, Fig. 5.7 shows a HRXRD scan of a sample with the same composition as the sample mentioned above. Here the fit cannot reproduce the measured data. In this case, thickness fringes can only be identified for the (In,Ga)As layer, not for the NiMnSb layer. This is a clear indication that the surface roughness of the NiMnSb layer is rather high, while the roughnesses of the (In,Ga)As buffer layer interfaces are still very small.

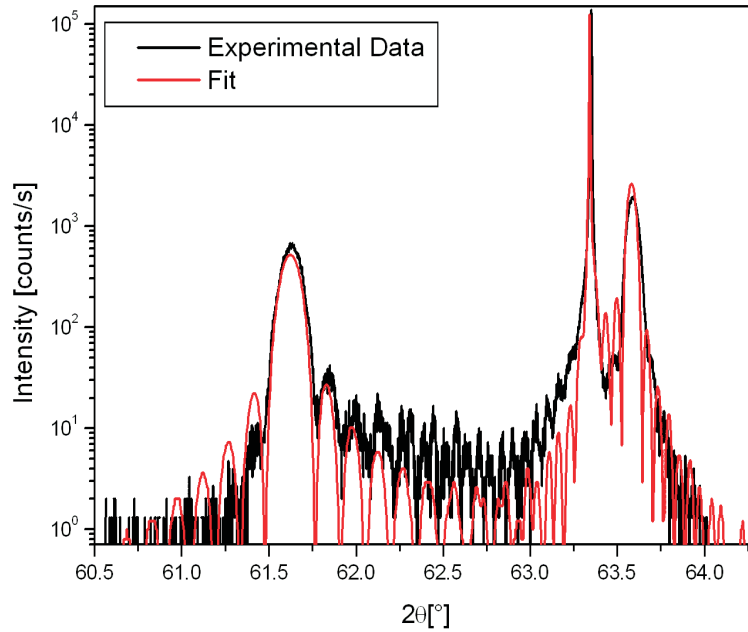


Figure 5.6: HRXRD  $\theta - 2\theta$  scan of the (004) reflection of a sample with 70 nm NiMnSb layer on a 150 nm thick (In,Ga)As buffer and the according fit. A very good agreement between the fit which is assuming ideal interfaces and the measured data is visible, indicating that all layers in this sample have interface roughnesses very close to zero.

## 5.2 Crystalline Properties

Crystalline properties of the NiMnSb crystals have been investigated using various x-ray and electron diffraction methods as well as transmission electron microscopy (TEM) and selected area diffraction (SAD). In the following sections the results of these investigations will be discussed.

### 5.2.1 Relaxation in NiMnSb Layers

NiMnSb has a lattice mismatch of 0.6% to InP and is therefore expected to show relaxation processes after a certain critical thickness. After the model of Matthews-Blakeslee [Mat74] the critical thickness  $t_{cr}$  can be expressed as:

$$t_{cr} = \frac{b(1 - \frac{\nu}{4})}{4\pi(1 + \nu)\frac{\Delta a}{a}} \ln\left(\frac{t_{cr}}{b} + 1\right) \quad (5.1)$$

where  $b$  is the magnitude of the burgers vector,  $\nu$  is the Poisson ratio and  $\frac{\Delta a}{a}$  is the lattice mismatch between layer and substrate. For NiMnSb most of these val-

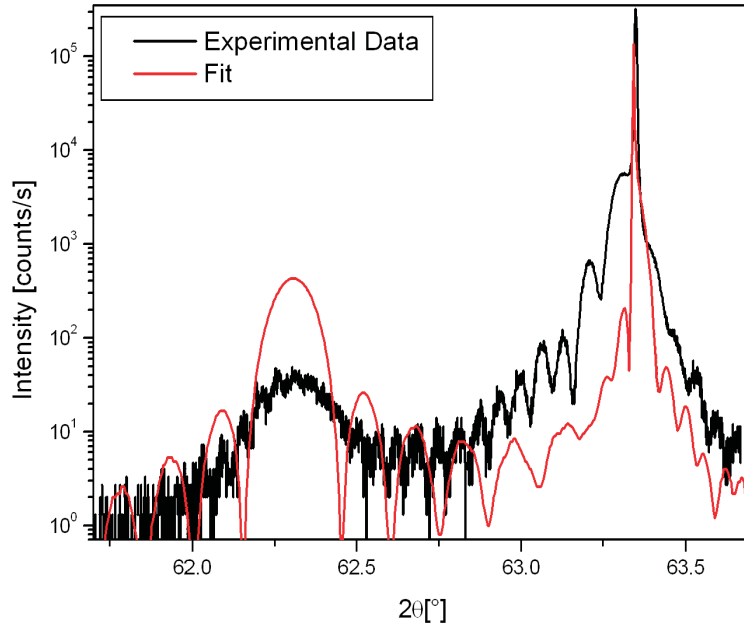


Figure 5.7: HRXRD  $\theta - 2\theta$  scan of the (004) reflection of a sample with 70 nm NiMnSb layer on a 150 nm thick (In,Ga)As buffer and the according fit. The fit which is assuming perfect interfaces does not reproduce the measured data, indicating that there is a pronounced interface roughness in this sample. Thickness fringes of the (In,Ga)As buffer can be identified but no fringes caused by the NiMnSb layer. This indicates that the interface between (In,Ga)As buffer layer and NiMnSb has a low roughness. The surface roughness, however, is far from being perfect.

ues have to be obtained from own measurements since pseudomorphic growth of this material has not been studied so far. To measure the Poisson ratio, the vertical lattice constants of a fully pseudomorphic and a fully relaxed layer of NiMnSb are needed. The fully pseudomorphic lattice constant can be calculated out of a standard  $\theta - 2\theta$  scan of a up to 40 nm thick NiMnSb layer on InP. Since totally relaxed growth of NiMnSb on InP is not easy to accomplish, NiMnSb has been grown on GaAs. The large lattice mismatch of more than 4% causes the NiMnSb to relax directly after the growth of a few ML. The Poisson ratio  $\nu$  can be calculated by

$$\nu = \frac{1 - \frac{a_{\perp}(a_{rel} - a_S)}{a_S(a_{\perp} - a_S)}}{1 + \frac{a_{\perp}(a_{rel} - a_S)}{a_S(a_{\perp} - a_S)}} \quad (5.2)$$

where  $a_S$  is the lattice constant of the substrate,  $a_{rel}$  the lattice constant of a fully relaxed NiMnSb layer and  $a_{\perp}$  the vertical lattice constant of a fully pseudomor-

phic NiMnSb layer. The obtained lattice constants are:

$$\begin{aligned} a_{\perp} &= 6.012 \text{ \AA} \\ a_{rel} &= 5.949 \text{ \AA} \\ a_S &= 5.869 \text{ \AA} \end{aligned} \quad (5.3)$$

With these values the calculation of the Poisson ratio gives:

$$\nu = 0.27 \quad (5.4)$$

Together with the magnitude of the burgers vector of the dominating defects in NiMnSb along [110] (see Sec. 5.2.2)

$$b = \frac{\sqrt{2}a_{rel}}{2} \quad (5.5)$$

an estimate of the critical thickness

$$t_{cr} \approx 12 \text{ nm} \quad (5.6)$$

can be obtained. This means layers thicker than 12 nm are expected to relax during growth.

To detect relaxation in grown layers, usually reciprocal space maps are necessary.  $\theta - 2\theta$  scans of symmetric reflections and rocking curves can give some hints whether or not the layer is fully pseudomorphic by examining the mosaicity of the different layers. However, only reciprocal space maps contain the necessary and detailed information about the status of relaxation in the layer.

For measuring reciprocal space maps grazing incident x-ray diffraction was used. As pointed out in section 3.2.1, the advantage of this method compared to standard HRXRD methods is the possibility of variation of the penetration depth of the x-rays. Thus, the measured signal is dominated by different parts of the sample and even different parts of the same layer.

Several NiMnSb layers with different thicknesses ranging from 15 to 120 nm have been investigated (Figs. 5.8-5.11). As expected, NiMnSb layers thicker than 15 nm show a relaxed signal. But at the same time all layers, even the thickest sample, also show a clear signal of pseudomorphic NiMnSb. This behavior is not easily explainable with standard relaxation processes. From these reciprocal space maps it is not clear if the detected signal is really some relaxed layer on the top of the measured sample or if it comes from some different crystallographic phase distributed equally inside the NiMnSb layer. To rule out the latter possibility, several reciprocal space maps of one sample (H66) with different penetration depths of the x-rays have been recorded. If there is a relaxed layer on top of the

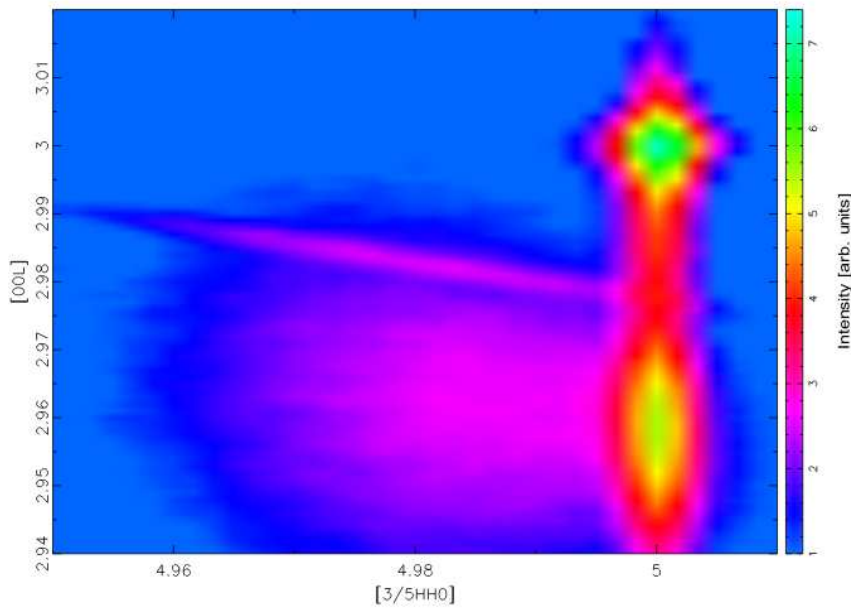


Figure 5.8: GIXRD reciprocal space map of the (353) reflection of H66, a 40 nm thick NiMnSb layer on (In,Ga)As/InP. Apart from the pseudomorphic parts in the layer which all lie on a h-value of 5, a partly relaxed signal with h-values around 4.98 can be seen. The origin of the streak going from  $l=2.99, h=4.955$  to  $l=2.98, h=5.0$  is currently not clear.

sample, the intensity ratio of the pseudomorphic/relaxed NiMnSb peak will increase with higher penetration depth since a larger part of the x-rays is scattered in the lower parts of the sample which consist of the pseudomorphic NiMnSb. Fig. 5.12 shows the intensity ratio versus penetration depth. It clearly shows the increasing intensity ratio with larger penetration depth. Therefore the sample consists of a partly relaxed NiMnSb layer on the top with a totally pseudomorphic NiMnSb layer underneath.

In these samples we therefore have both a relaxed and a pseudomorphic part in the same NiMnSb layer. In standard III-V and II-VI semiconductors the crystalline defects which evolve during the relaxation process prolong to the next interface underneath. This behavior is not found in NiMnSb. But not only has NiMnSb a relaxed and a pseudomorphic part simultaneously, with increasing total thickness both the pseudomorphic and the relaxed part get thicker. This means that there is no critical thickness from whereon the NiMnSb grows as a relaxed crystal. If this was the case, the pseudomorphic layer would have the same thickness in all samples which show relaxation. As can be seen clearly in the reciprocal space maps both the relaxed and the pseudomorphic part of NiMnSb get thicker

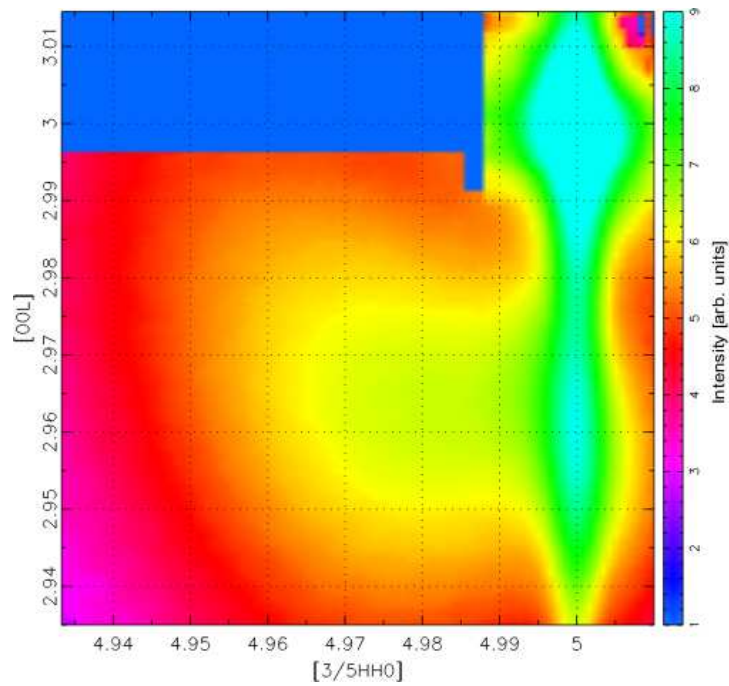


Figure 5.9: GIXRD reciprocal space map of the (353) reflection of H80, a 70 nm thick NiMnSb layer on (In,Ga)As/InP. As for H66, a pseudomorphic NiMnSb layer ( $h=5.0$ ) as well as a partly relaxed NiMnSb layer ( $h=4.98$ ) are visible.

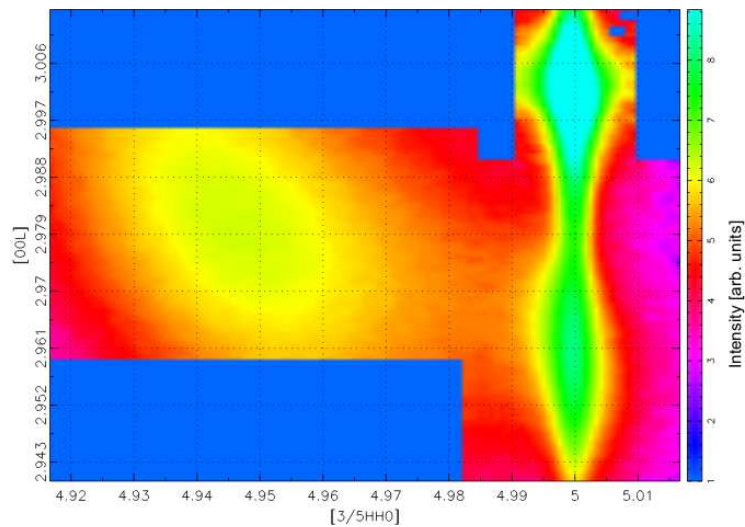


Figure 5.10: GIXRD reciprocal space map of the (353) reflection of H76, a 120 nm thick NiMnSb layer on (In,Ga)As/InP. Both a totally relaxed NiMnSb part ( $h=4.945$ ) and a pseudomorphic part ( $h=5.0$ ) can be seen.



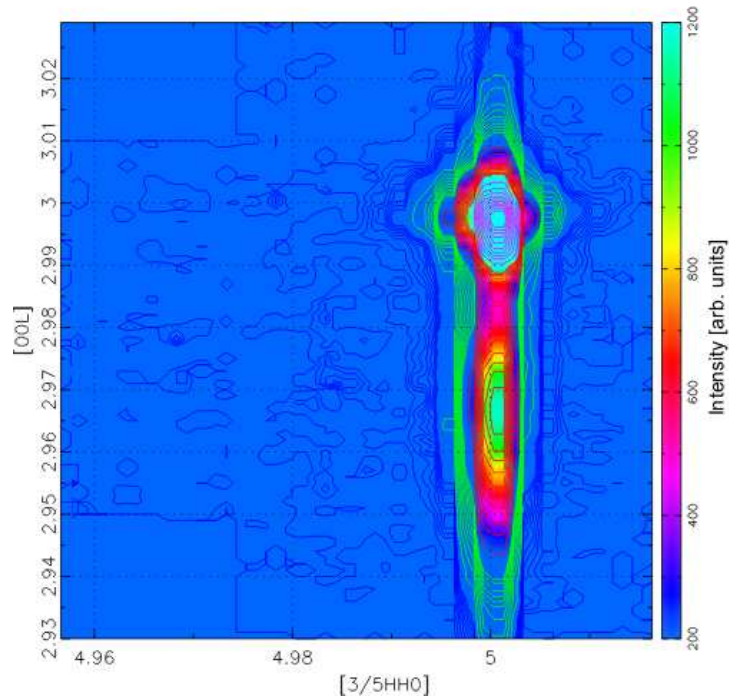


Figure 5.11: GIXRD reciprocal space map of H111, a 15 nm thick NiMnSb layer on (In,Ga)As/InP. For clarity, contour lines have been added. A relaxed part can not be detected in this layer, although a slight asymmetric broadening of the NiMnSb peak is visible.

with increasing total thickness. The ratio of relaxed to pseudomorphic thickness does increase with increasing total thickness but still the pseudomorphic part gets larger.

If we assume that the relaxation occurs directly during growth, this would imply that there are two growth processes: First the relaxed NiMnSb is grown at the top of the sample and second in a certain depth of the NiMnSb layer this relaxed part is transformed into the pseudomorphic part. Another possibility is that the whole relaxation process starts after growth during cooling down to room temperature. For this to occur the thermal expansion coefficients of NiMnSb and InP have to be that different that during the cooling process from 250°C to room temperature the stress in the NiMnSb exceeds a certain limit and parts of the NiMnSb layer start to relax. In this case it would be hard to explain why the thickness at which the layer is relaxed changes with different total thicknesses of NiMnSb. One approach would be the different degrees of relaxation in layers, varying from partly relaxed for the 40 nm sample to totally relaxed for the 120 nm sample.

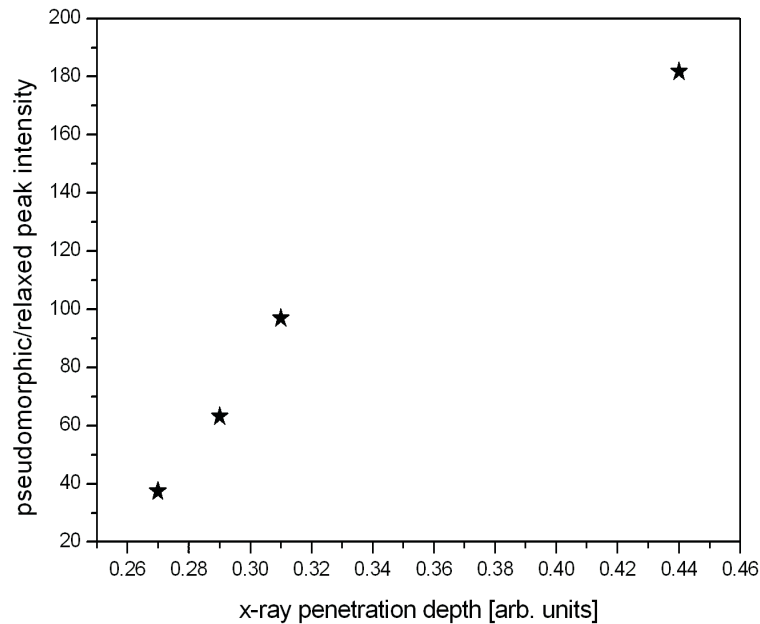


Figure 5.12: Intensity ratio of the NiMnSb pseudomorphic/relaxed peak from multiple reciprocal space maps measured with different x-ray penetration depths. With increasing penetration depth the intensity ratio gets larger, indicating that the sample really has a partly relaxed NiMnSb part on top.

## 5.2.2 Crystalline Defects in NiMnSb

To analyze defect nucleation in NiMnSb layers, plan-view and cross-section TEM and SAD studies have been performed by the group of K. Kavanagh at the Simon Fraser University, Vancouver, Canada. In plan-view TEM experiments planes parallel to the surface are examined, this gives a “top view” of the sample. Cross-section TEM, in contrast, analyzes slices with their surfaces perpendicular to the sample surface. In this case interfaces between the different materials, in particular between (In,Ga)As and NiMnSb can be examined. Fig. 5.13 shows the principle measurement geometry of these two methods. See [dG03] for more details on TEM principles and methods.

The samples for plan-view TEM were prepared by chemically dissolving the InP substrate in concentrated HCl leaving the NiMnSb/(In,Ga)As films intact. Cross-sections were prepared by focused ion beam (FIB) sectioning using a Ga ion beam of 30 keV. TEM was carried out at an electron beam accelerating voltage of 200 keV. In the SAD experiments the angular distribution of the transmitted and diffracted electrons is evaluated. The diffraction pattern represents an image of the reciprocal lattice and therefore contains information of the crystal structure.

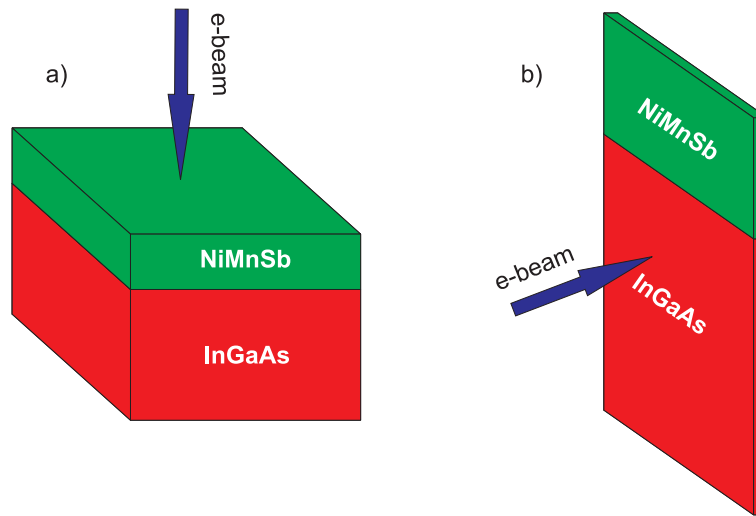


Figure 5.13: Principle measurement setup for plan-view TEM geometry (a) and cross-section TEM geometry (b).

In our case, this technique was used in plan-view geometry. More details on selected area electron diffraction can be found in [Ben01].

In agreement with the GIXRD results (section 5.2.1) the TEM measurements show that the NiMnSb films are single crystalline. However, isolated defects are found beginning in the thinnest films (10 nm) investigated. These defects increase in size with increasing film thickness until they appear to overlap at a thickness of 40 nm. Fig. 5.14 shows plan-view TEM images for 10 and 40 nm NiMnSb/(In,Ga)As films and an associated SAD pattern of the 40 nm film. These are bright field (BF) images taken with the sample tilted to a strong diffraction condition such that the diffraction vector  $g = (220)$  with the planes perpendicular to the surface. The average spacing of the visible defects is 30 nm which corresponds to a defect density of  $1 \times 10^3 \mu\text{m}^{-2}$ . It is apparent that these defects are forming early in the growth probably at the interface. During the successive growth these defects are growing larger and are overlapping at a thickness of 40 nm. The strong spots in the diffraction pattern are consistent with a NiMnSb half-Heusler crystal structure combined with the zincblende (In,Ga)As. Fig. 5.15 shows a higher magnification image of the SAD in Fig. 5.14 (b) with an indexed diagram. Weak half-order spots or streaks are apparent along each  $\langle 100 \rangle$  and  $\langle 120 \rangle$  direction, indicating that long range ordering is also occurring in the NiMnSb films.

The defects are further investigated using BF, 2-beam images for a 40 nm NiMnSb film tilted to  $g = (220)$ ,  $(\bar{2}\bar{2}0)$ ,  $(200)$ , and  $(020)$  diffraction conditions (Fig. 5.16). In each case the contrast from defects running perpendicular to  $g$  is visible.

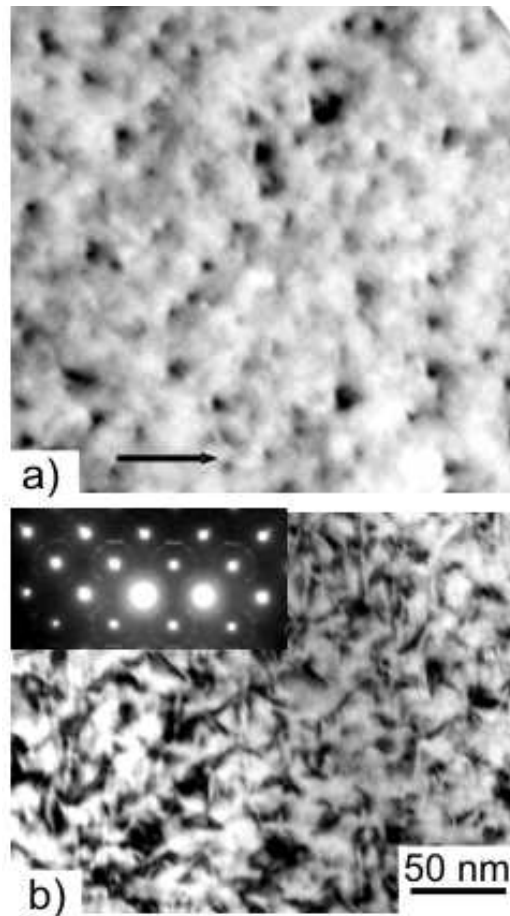


Figure 5.14: TEM bright field images of NiMnSb / (In,Ga)As(001) films obtained in plan-view geometry for two NiMnSb film thicknesses: a) 10 nm and b) 40 nm. The film has been tilted to a strong two-beam diffraction condition with the diffraction vector  $g = (220)$  as indicated by the arrow in (a) and the SAD pattern in (b).

Therefore the lattice displacement is perpendicular to the defect line direction, which is consistent with either a stacking fault or an edge dislocation [Hir77]. Depending on the degree of deviation from the exact Bragg condition, the defects in contrast appear with a black/white/black appearance or as a single black region. From their contrast behavior two sets of defects can be distinguished. The prevalent contrast is caused by defects aligned close to the  $\langle 100 \rangle$  directions. These go out of contrast for the perpendicular  $\{200\}$  condition, whereas they are still visible under  $\{220\}$  diffraction conditions. Another set of defects is aligned along  $\langle 110 \rangle$  directions and go completely out of contrast for either  $\{200\}$  diffraction conditions or the  $g = (220)$  condition perpendicular to its line direction. A tilt

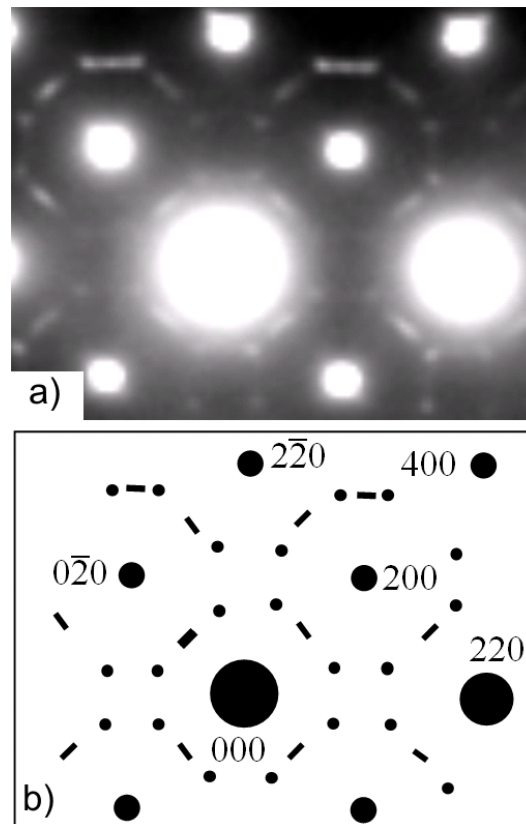


Figure 5.15: Magnification (a) and index (b) of the SAD pattern of Fig. 5.14. The major spots are regular diffraction from the expected NiMnSb/(In,Ga)As structures, while the weaker, extra streaks and spots are from NiMnSb ordering along the  $\langle 100 \rangle$  and  $\langle 110 \rangle$  directions.

of this sample by angles up to  $20^\circ$  about in-plane  $\langle 110 \rangle$  axes cause an increase in the length of the  $\langle 110 \rangle$  defects.

Along the edges of the thinned regions of the same sample, thinner patches are found where the (In,Ga)As layer has been etched away leaving only NiMnSb, which has been confirmed by scanning transmission electron microscopy-energy dispersive spectroscopy (STEM-EDS) analysis. No difference in the density of defects can be found, however, without the (In,Ga)As, the films are much more transparent and lattice images are clearer. Fig. 5.17 shows a lattice image example obtained with the beam parallel to the  $[001]$  pole. The smallest square lattice fringes, which have an average spacing of  $0.30 \pm 0.01$  nm, are therefore associated with the  $\{200\}$  NiMnSb planes. In the magnified view showing one isolated defect, the fact that there is no perpendicular edge dislocation in this area can be shown by drawing a burgers circuit around the defect [Hir77]. The surrounding

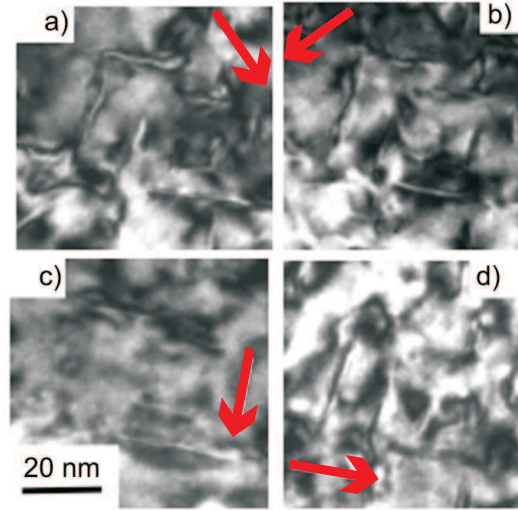


Figure 5.16: TEM bright field images of a 40 nm thick NiMnSb(001) film (same as in Fig. 5.14). All images show an identical area as a function of diffraction conditions (sample tilted) as indicated by the arrows perpendicular to the diffraction planes (a) (220), (b) ( $2\bar{2}0$ ), (c) (200) and (d) (020). The (In,Ga)As buffer has been etched away in this region.

crystal is in phase. Nevertheless, a deformation with double period fringes can clearly be seen inside the defect region which is visible along the defect length consistent with  $\{100\}$  ordering. Also a double stacking fault with many distortions appears to be there.

The thickest films investigated by TEM (85 nm) show overlapping finite size, planar defects aligned closely with in-plane  $\langle 120 \rangle$  directions (Fig. 5.18 (a)). Atomic ordering is still visible in the SAD pattern. Fig. 5.18 (b) shows a cross-sectional phase contrast TEM micrograph from the same sample, taken with the electron-beam direction aligned with a  $\langle 110 \rangle$  direction. The NiMnSb/(In,Ga)As interface is atomically smooth and abrupt. The (002) fringe spacing,  $f$ , on each side of the interface measures 2.92 Å for (In,Ga)As and 3.01 Å for NiMnSb. The lattice constant for InP is 5.868 Å ( $2 \times 2.92$  Å) so the (In,Ga)As is lattice matched to InP while the NiMnSb film is in compression. From the x-ray results the Poisson ratio,  $\nu$ , was determined to be 0.27 (see section 5.2.1). Therefore, the relaxed lattice constant  $a_{rel}$  of the NiMnSb is given by  $a_{rel} = a_{(In,Ga)As} + 2\Delta f \frac{(1-\nu)}{(1+\nu)} = 5.97$  Å. From this thinned sample it is not possible to tell whether there are any interfacial dislocations at the interface since the perpendicular fringes are unclear.

The exact nature of the defects remains unclear, however, misfit dislocations can be ruled out. There are two sets of defects identified by the TEM micrographs obtained using different diffraction conditions: one aligned approximately with

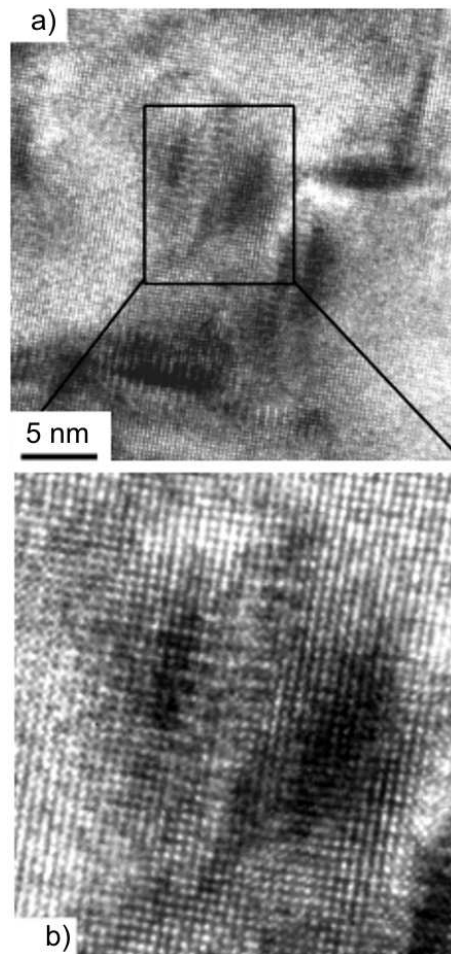


Figure 5.17: The same film as in Fig. 5.16 imaged in plan view, downpole (parallel to the [001] direction) at higher magnification. The image has been obtained using multiple beams showing interference fringes from the (002) planes in each material. Image (b) is a magnified view by a factor 3 of the square area in (a).

$\langle 100 \rangle$  and one aligned exactly with  $\langle 011 \rangle$  directions. Since there is a strong loss of contrast for each change in diffraction condition, this rules out  $60^\circ$  dislocations, a common type of misfit dislocation found in lattice mismatched semiconductor systems [Gol98, Reß98]. Pure interfacial edge misfits with slip vectors  $b = a/4\langle 100 \rangle$  or  $b = a/2\langle 011 \rangle$  and glide planes perpendicular to the film surface could explain the obtained TEM data, however, in this case the average spacing of 30 nm would cause a complete relaxation of the tetragonal strain in the film. This is not consistent with x-ray measurements (see section 5.2.1), which show little strain relaxation in the thinner films, certainly up to a thickness of 40 nm. Additionally, the comparison of images with and without the (In,Ga)As layer shows

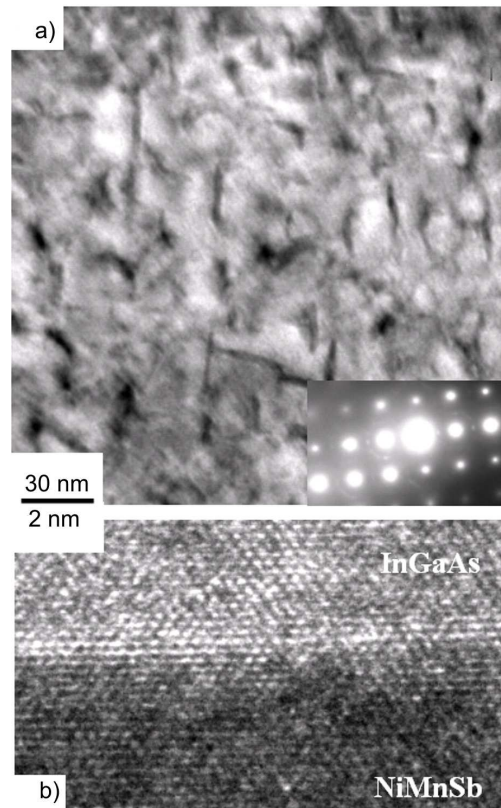


Figure 5.18: Plan view (a) and cross sectional (b) view of an 85 nm thick NiMnSb/(In,Ga)As film, obtained with TEM. The insert in (a) is a SAD pattern showing the diffraction conditions and orientation of the film. The defects appear to align closely with the  $\langle 100 \rangle$  as well as with the  $\langle 120 \rangle$  directions.

little difference in the defect densities. Furthermore, tilting the sample causes changes of the length of the  $\langle 011 \rangle$  defects indicating that they are inclined rather than fixed to the interface. The  $\langle 011 \rangle$  defects may still be dislocations but if so these thread through the film.

The  $\langle 100 \rangle$  defects are a collection of isolated planar defects running from the interface to the surface. In thicker films these defects overlap. They do not consist of  $a/3\{111\}$  stacking faults which are common in fcc cubic systems, which would have been easily identified in plan view  $\langle 100 \rangle$  images. These micrographs would show strong extinction fringes associated with these defects which were not observed in the investigated films. However, the observed features may be caused by  $a/2\{001\}$  or  $\{011\}$  stacking faults or some type of  $\{001\}$  antiphase boundary. Some indications of ordering domains can be clearly seen from the double fringes within the defect regions. These could well be associated with stacking faults



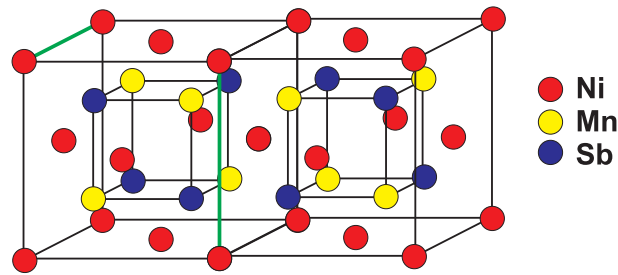


Figure 5.19: Diagram showing an antiphase boundary plane formed by a  $90^\circ$  rotation in the Mn/Sb sublattice as indicated by the green lines.

along  $a/2\{001\}$  or  $a/2\{011\}$  planes. The typical antiphase boundary often found in the growth of III-V semiconductors on group IV, e.g. GaAs/Si, or GaP/Si [Coh02, Kom94], do not seem to be present consistent with the RHEED and LEED measurements as shown in section 5.1.2. Nevertheless, antiphase boundaries associated with only one sublattice, such as errors in the Mn and Sb atomic locations, are possible in these films. Fig. 5.19 shows a drawing of one such defect running along  $\{100\}$  planes. These imperfections may influence the subsequent Ni layer and create threading dislocations which may also be an explanation for the ordering and the contrast. Additionally, if the strain relaxation is caused by this type of defects, then their effects will be greater in the thickest films, which has been observed in the x-ray measurements.



## Chapter 6

# Magnetic Properties of NiMnSb(001)

NiMnSb(001) structures were investigated for their magnetic properties using Magneto-Optical Kerr effect (MOKE), Ferromagnetic Resonance (FMR) and Scanning Quantum Interference Device (SQUID) magnetometry.

MOKE uses rotation, intensity changes and changes in ellipticity of reflected light from a magnetized layer. For our measurements the longitudinal Kerr effect was used. In this case the oscillation plane of linear polarized light reflected from the sample is rotated in the direction of the incoming light when the magnetization  $M$  is parallel to the surface and parallel to the plane of incidence of the light (Fig. 6.1). This Kerr rotation is proportional to the magnetization component in the layer. A quantum theory of the Kerr effect showing the linear dependence of the Kerr effects on the magnetization was developed by Vonsovskii and Sokolov [Von49]. MOKE is used to measure hysteresis curves of the NiMnSb layers in different in-plane directions. Details on the physics and applications of MOKE can be found in [Cra95].

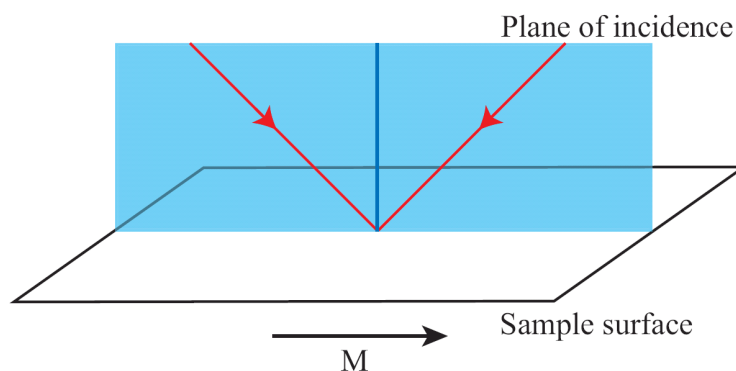


Figure 6.1: Longitudinal MOKE geometry

The spin resonance of ferromagnets, or FMR, resembles in principle the nu-

clear magnetic resonance (NMR). The basic setup consists of a static magnetic field and a perpendicular oscillating field. The total magnetic moment of a sample precesses around the direction of the static magnetic field. The energy absorption of a transversal high frequency field is at maximum, if its frequency is equal to the frequency of the precession. Since for ferromagnetic layers also internal magnetic fields inside the ferromagnet have to be taken into account, these fields give access to anisotropy effects inside the ferromagnet. Therefore, FMR is an excellent experiment for the determination of anisotropies in these materials. Solutions of the FMR resonance frequency were first calculated by Gilbert [Gil55]. For FMR experiments the resonance frequency usually lies in the microwave regime, therefore typical experimental setup consists of a waveguide and a cavity for microwaves (Fig. 6.2). The energy loss in the system is measured by monitoring the Q-factor of the cavity. An introduction into FMR and other magnetic resonance techniques can be found in [Blu01, Cra95]. Details on FMR measurement principles and methods on reduced dimension systems can be found in [Bar97]. The FMR experiments shown in this section were performed in the group of Bret Heinrich at the Simon Fraser University, Vancouver, Canada.

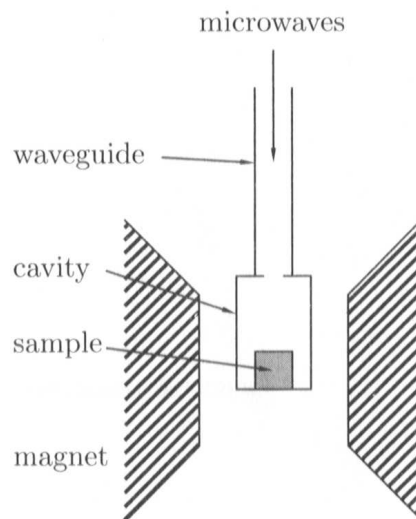


Figure 6.2: Typical FMR setup (from [Blu01])

SQUID magnetometry uses a superconducting ring which contains two parallel Josephson junctions in it. The ring is therefore able to act like a very sensitive quantum interferometer and is able of measuring magnetic fields with a detection limit of up to  $10^{-14}$  T. [vD81] gives more details on the principles of the different SQUID types and their setup.

## 6.1 Magnetic Anisotropies

The dependence of the in-plane FMR field on the angle between the applied field and the [100] crystallographic axis allows for determining the in-plane uniaxial anisotropy  $2K_U^{\parallel}/M_s$ , the fourfold in-plane anisotropy field  $2K_1^{\parallel}/M_s$  and the field  $4\pi M_{eff}$ , which is required to magnetize the sample perpendicular to the surface.  $4\pi M_{eff} = 4\pi M_s - 2K_U^{\perp}/M_s$ , where  $2K_U^{\perp}$  is the perpendicular uniaxial anisotropy and  $M_s$  the saturation magnetization. The perpendicular uniaxial anisotropy in cubic materials is caused either by interfaces or lattice strains [Hei93]. Figs. 6.3 to 6.6 show the FMR field as a function of the in-plane angle  $\varphi$  with respect to the [100] axis of NiMnSb(001). As can be clearly seen from the data, the FMR field shows a strong dependency on the thickness of the NiMnSb layer. Additionally, for the 5 nm and 40 nm thick samples there is a strong uniaxial component, which is dominating the FMR spectra. For the thin sample the easy axis was aligned along  $[1\bar{1}0]$  while for the thick sample the easy axis was along  $[110]$ . The samples with intermediate thickness show no in-plane uniaxial anisotropy, the FMR data is dominated by the fourfold anisotropy.

The FMR fields from this data were fit with a model calculation which allows for the determination of the three components of the magnetic anisotropies mentioned above (Figs. 6.7 to 6.9). The uniaxial anisotropy field shows for the samples above 20 and below 10 nm a linear dependence on  $1/d$ . This could be an indication for the presence of in-plane interface uniaxial anisotropy with  $K_{U,s}^{\parallel} = 0.08 \text{ erg/cm}^2$  along the magnetic easy axis. It is probably caused by the chemistry of the interface between the (In,Ga)As buffer layer and NiMnSb film. For  $d \rightarrow 0$  the uniaxial anisotropy field is close to -200 Oe. This anisotropy can be caused by anisotropic strain relaxation of the in-plane tetragonal strain. This effect is known for Fe/GaAs(001) [Tho03] and Fe/InAs(001) films [Xu00] where anisotropic strain relaxation along the crystallographic  $[110]$  and  $[1\bar{1}0]$  axis was found. Due to larger strain relaxation along the  $[110]$  axis the resulting shear strain caused a magnetic uniaxial anisotropy along  $[1\bar{1}0]$ . This anisotropic strain relaxation would in principle be detectable by XRD reciprocal space maps. It would manifest itself in an asymmetric NiMnSb peak in  $k$  and  $l$  direction. Measurements on the relaxed peak of a 120 nm thick sample by GIXRD showed no detectable asymmetry of the NiMnSb peak. However, the difference in strain relaxation needed to cause a magnetic uniaxial anisotropy of that extend is less than the detection limit of this experiment, which in this case is dominated by the FWHM of the relaxed NiMnSb peak.

In contrast to the uniaxial anisotropy field,  $4\pi M_{eff}$  and  $2K_1^{\parallel}/M_s$  do not show a linear dependence on  $1/d$ .  $4\pi M_{eff}$  decreases while  $2K_1^{\parallel}/M_s$  increases with increasing film thickness. For the thinnest films the fourfold anisotropy  $2K_1^{\parallel}/M_s$

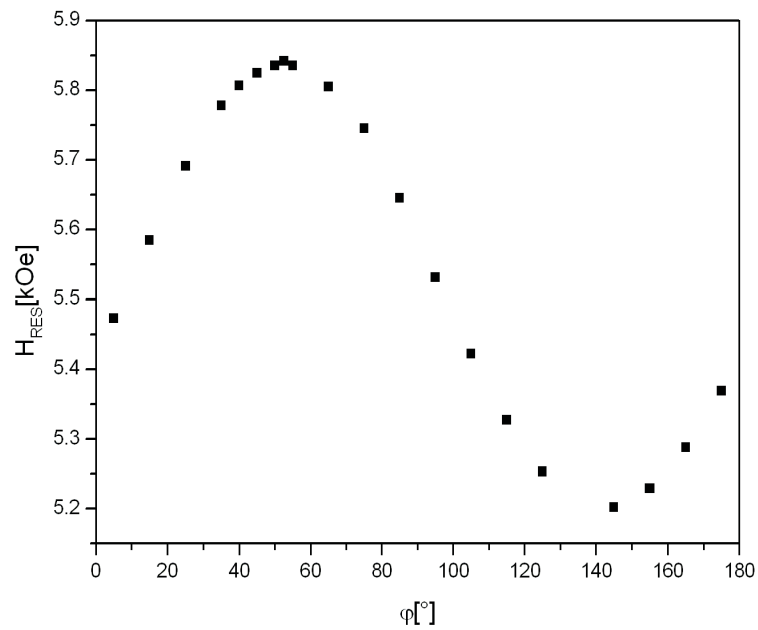


Figure 6.3: Angular dependence of the maximum FMR field at 23.92 GHz for a sample with 5 nm NiMnSb. Both the applied dc field and the saturation magnetization are in-plane. The angle  $\varphi$  is in direction of the applied field and the saturation magnetization with respect to the [100] axis of NiMnSb.

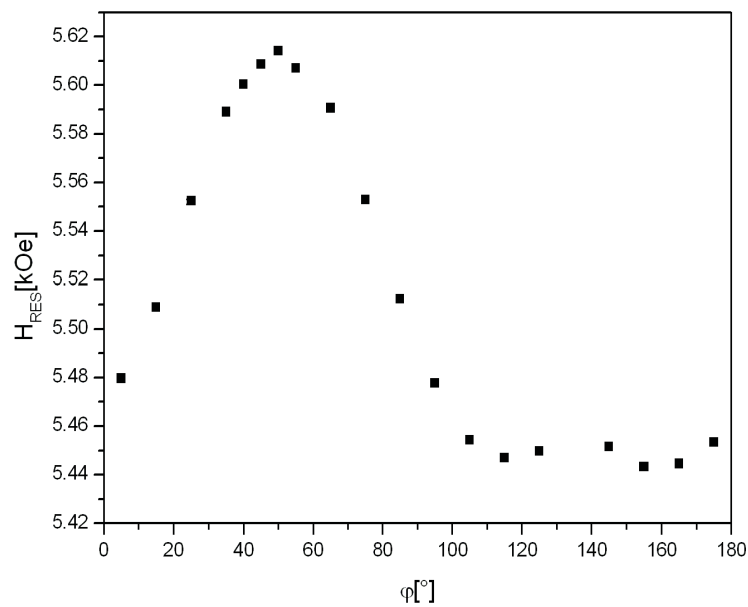


Figure 6.4: The same FMR measurement as in Fig. 6.3 but for a sample with 10 nm NiMnSb.

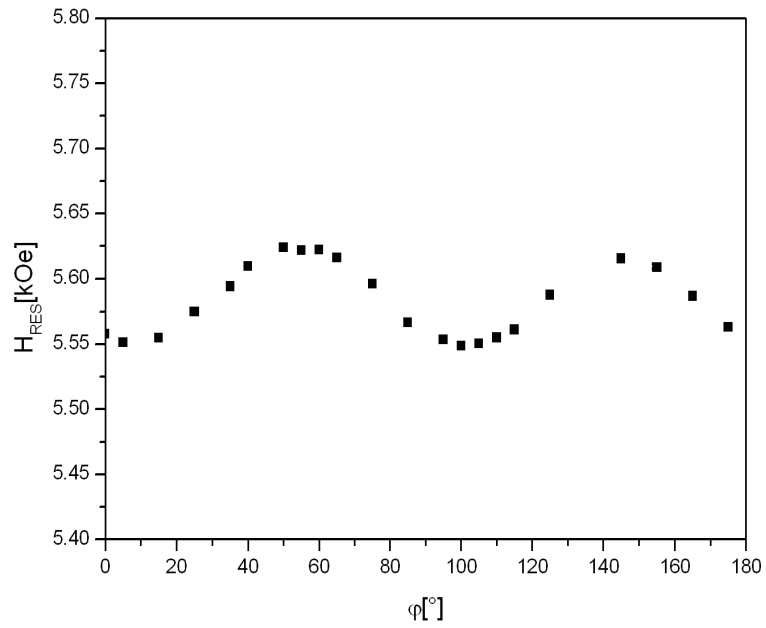


Figure 6.5: The same FMR measurement as in Fig. 6.3 but for a sample with 20 nm NiMnSb.

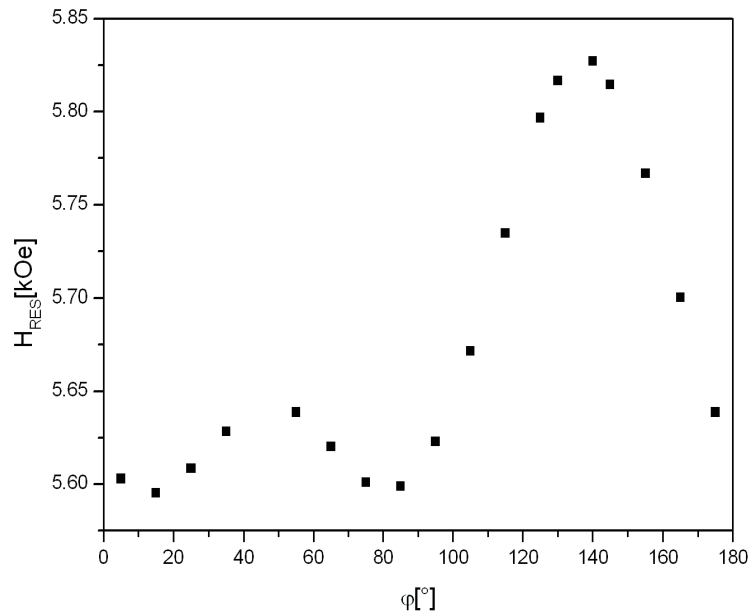


Figure 6.6: The same FMR measurement as in Fig. 6.3 but for a sample with 40 nm NiMnSb.

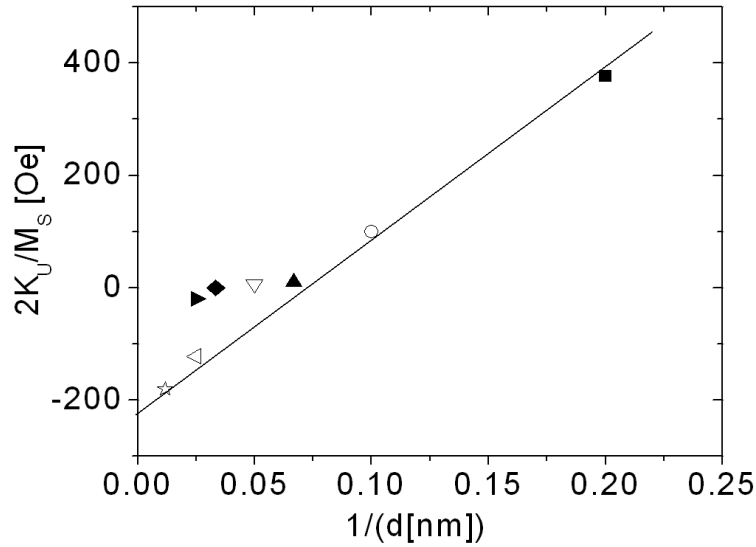


Figure 6.7: The in-plane uniaxial anisotropy field  $2K_U/M_s$  as a function of the inverse NiMnSb film thickness  $1/d$ . The direction of the uniaxial anisotropy axis is along  $[1\bar{1}0]$ . Note that the anisotropy field is nearly zero for samples with intermediate thickness (20 to 35 nm) and changes its sign for the samples thicker than 20 nm ( $1/d = 0.05$  1/nm).

vanishes. This anisotropy is probably caused by crystallographic defects which satisfy the in-plane fourfold symmetry as was observed in bcc Ni/Fe(001) films [Hei88]. Measurements of the  $g$ -factor show a value of 2.03 and 2.02 for the 42 and the 15 nm thick films, respectively. These values are very close to the free-electron  $g$ -factor of 2, indicating the spin orbit interaction in NiMnSb is very weak.

## 6.2 Magnetic Damping

From measurements of the FMR linewidth,  $\Delta H$ , significant information can be obtained. The dependence of  $\Delta H$  on the crystal direction can be divided into three components: the angular independent  $\Delta H_0$ , the fourfold  $\Delta H_4 \cos^2(2\varphi_m)$  and the twofold  $\Delta H_2 \cos^2(\varphi_m)$  contributions. Fig. 6.10 shows the dependence of  $\Delta H$  on the crystal direction. Thin NiMnSb layers (up to 5 nm) show a very low linewidth of 20 Oe at 24 GHz along  $\langle 100 \rangle$ . Additionally the linewidth is nearly independent on the angle  $\varphi_m$  ( $\Delta H_2 = 0$  and  $\Delta H_4 = 0$ ). The FMR linewidth versus the microwave frequency shows a linear behavior, indicating that the magnetic damping with the magnetization along  $\langle 100 \rangle$  is caused by Gilbert damping. The measured Gilbert damping parameter has a remarkably low value of



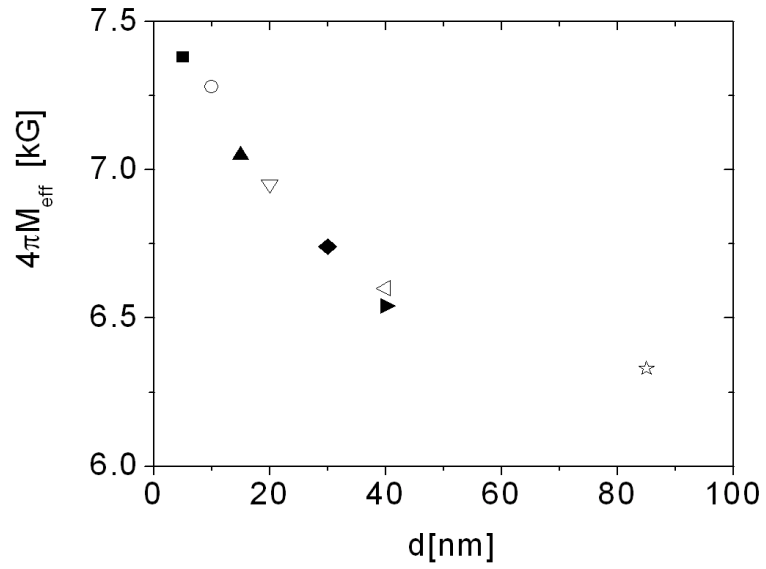


Figure 6.8:  $4\pi M_{\text{eff}}$  as a function of the NiMnSb film thickness  $d$ .

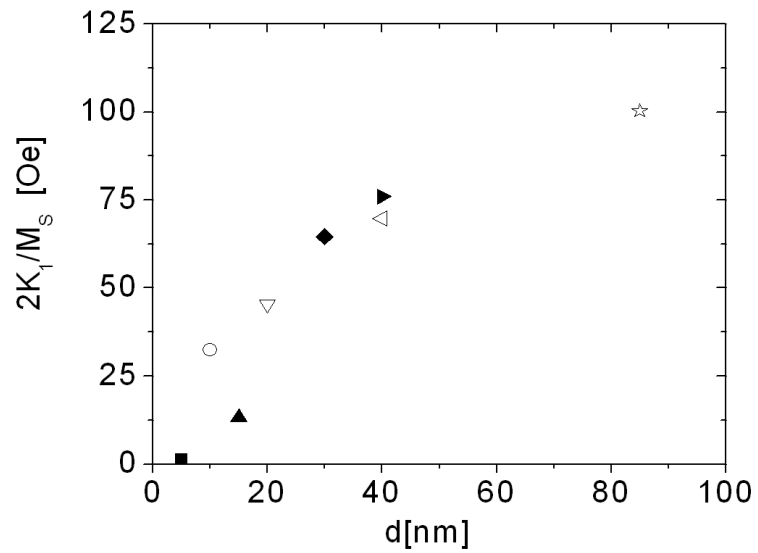


Figure 6.9: The in-plane fourfold anisotropy field  $2K_1/M_s$  as a function of the NiMnSb film thickness  $d$ .

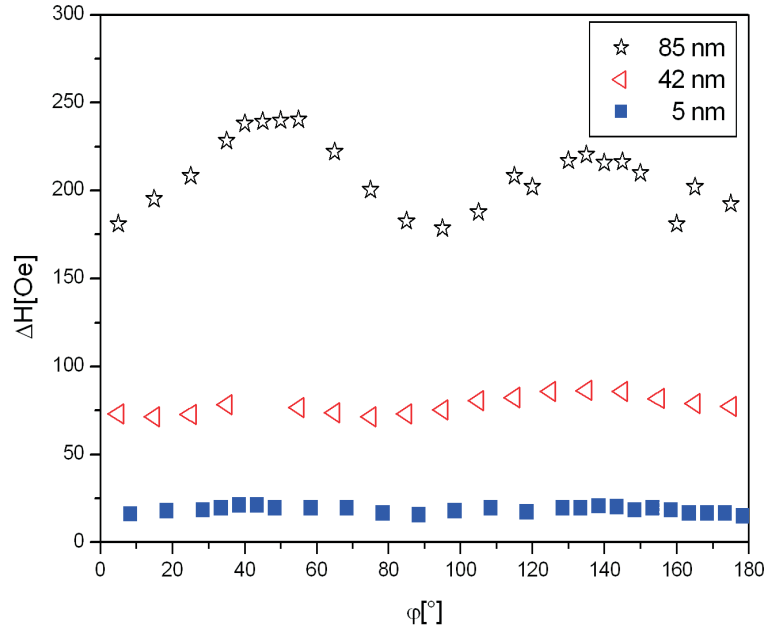


Figure 6.10: The FMR linewidth at 24 GHz versus the angle  $\varphi_m$  between the magnetization and the in-plane [100] crystalline axis. Especially for the thicker layers a pronounced angular dependence is evident.

$G = 3.1 \times 10^7 \text{ s}^{-1}$ . Compared to the lowest value observed for 3d transition element metals, bcc Fe, where  $G = 6 \times 10^7 \text{ s}^{-1}$  [Fra80], the value of NiMnSb is remarkably lower than even that of Fe. Since in metallic samples the Gilbert damping is caused by spin orbit interaction [Hei02], this indicates that the role of spin orbit interaction is quite weak in NiMnSb, which is consistent with the determination of the g-factor in section 6.1.

For thicker samples the situation changes. A large increase in the average  $\Delta H$  of up to 10 times the value of the 5 nm sample was observed for the 85 nm sample. This increase of  $\Delta H$  is most likely due to the extrinsic damping processes caused by magnetic inhomogeneities introduced into the sample by the lattice defects. Out-of-plane measurements of  $\Delta H$  on samples of varying thicknesses show that the FMR linewidth drastically decreases if the direction of the magnetic moment is moved close to the film normal. The end value along the film normal corresponds to the intrinsic Gilbert damping. This behavior can be explained by two magnon scattering [Hei02]. Therefore, the additional FMR line broadening which cannot be explained by Gilbert damping is caused by two magnon scattering relaxation.

### 6.3 Hysteresis Curves

Hysteresis curves measured by Magneto-Optical Kerr Effect (MOKE) show the strong anisotropies (Fig. 6.11 to 6.13). The coercive field of NiMnSb is notably small, a sample with a 5 nm thick NiMnSb layer has a coercive field of 3 Oe along the easy axis which in this case is along  $[1\bar{1}0]$  (Fig. 6.11). With increasing thickness the coercive field increases, an effect which can be attributed to the increased defect density in the thicker layers (Fig. 6.14). The theoretical magnetic moment for NiMnSb is expected to be  $4\mu_B$  [dG83] per unit cell, since 100% spin-polarized electrons result in an integer magnetic moment which in case of the crystal structure of NiMnSb is  $4\mu_B$ . The magnetic moment of NiMnSb can be obtained from hysteresis curves measured by SQUID magnetometry, which resulted in  $3.8\mu_B$  per unit cell. This lower value may be due to the observed lattice defects, which lower the minority spin band to a value close or below the Fermi surface and therefore destroy the 100% spin polarization at the Fermi level.

To measure the Curie temperature, temperature dependent magnetization measurements have been performed using SQUID magnetometry (Fig. 6.15). Due to the experimental setup the highest temperature reachable was 400K. The drop of the magnetization from 4K to 400K is  $\approx 5\%$ , which is consistent with the Curie temperature of 730K found in the literature [Cas55].

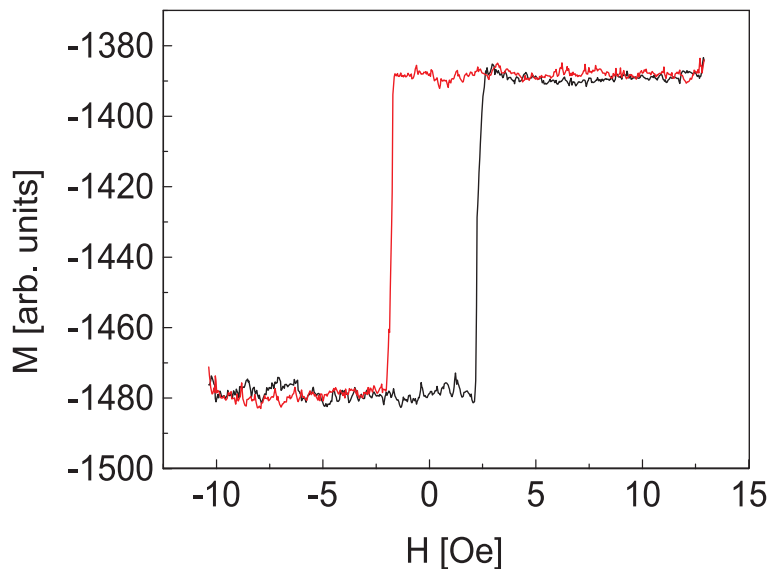


Figure 6.11: Hysteresis curve of a sample with 5 nm NiMnSb along  $[1\bar{1}0]$  measured by MOKE.

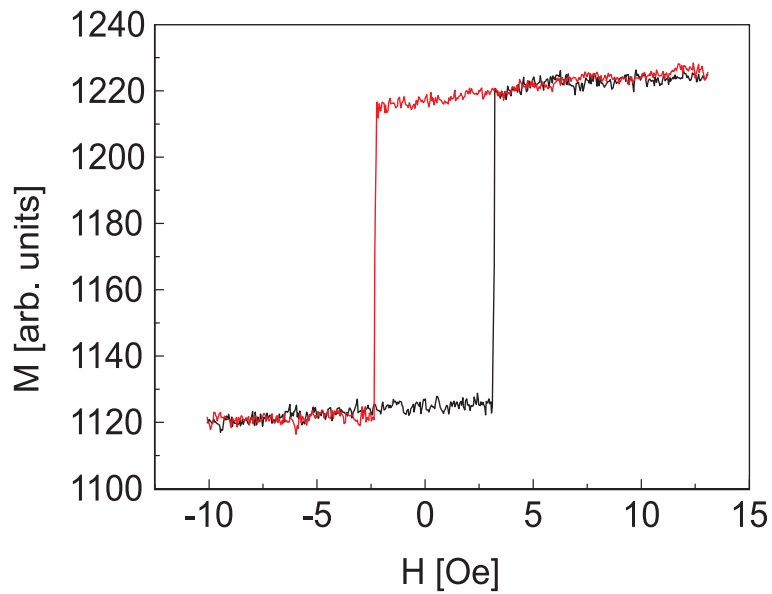


Figure 6.12: Hysteresis curve of a sample with 5 nm NiMnSb along [100] measured by MOKE. Note that at the NiMnSb layer is still not in saturation at the maximum or minimum fields shown.

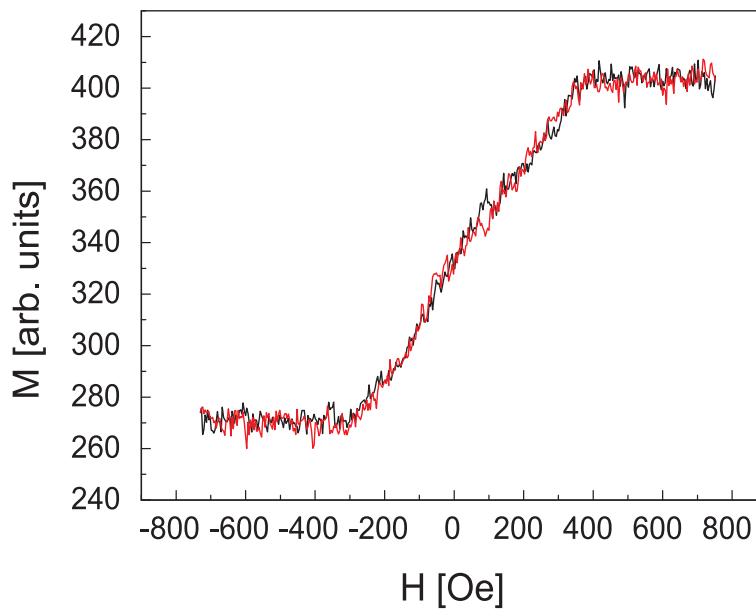


Figure 6.13: Hysteresis curve of a sample with 5 nm NiMnSb along [110] measured by MOKE.

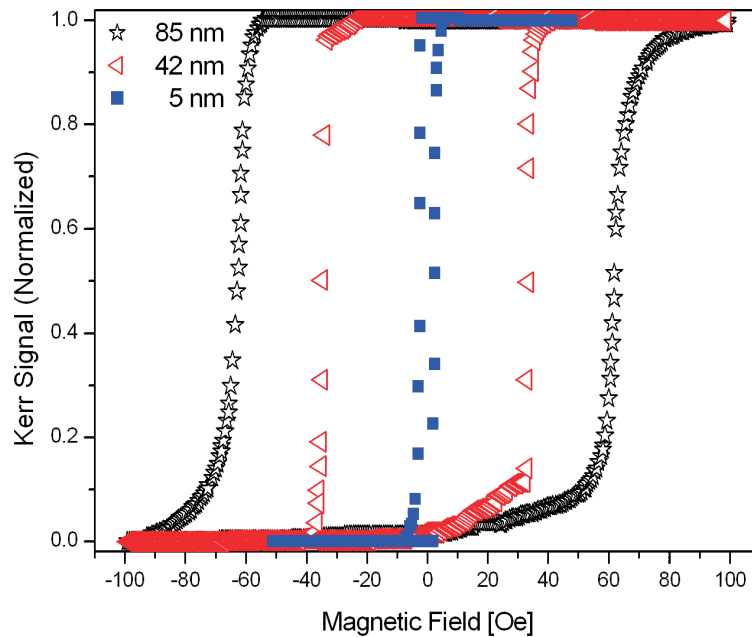


Figure 6.14: Hysteresis curves obtained by SQUID measurements of three samples with different thicknesses of the NiMnSb layer along the easy axis of this layer ( $[1\bar{1}0]$  for 5 nm,  $[110]$  for 42 and 85 nm). Note that the Kerr signal is normalized to the individual maximum of each sample.

## 6.4 Exchange Bias in NiMnSb/NiMn Bilayers

The phenomenon that the hysteresis loop of a ferromagnet coupled with an anti-ferromagnet shifts from the zero field origin was discovered almost half a century ago [Mei56]. A recent review on this phenomenon can be found in an article of Nogues and Schuller [Nog99]. This exchange biasing is used in spin valves based on the GMR or TMR effect to “pin” one of the two ferromagnetic layers and therefore keep the pinned layer’s magnetization unchanged during the operation of the spin valve. It provides an easy possibility to change the coercive field of a ferromagnetic layer. Without the antiferromagnet-ferromagnet coupling a different ferromagnetic material would be needed.

The material system based on the elements Ni, Mn and Sb has a wide variety of materials with unique magnetic properties. While NiMnSb is a half-metallic ferromagnet, the material NiMn shows an antiferromagnetic behavior for certain crystallographic phases. Since equiatomic NiMn grows in a fcc crystal structure which is not antiferromagnetic, the standard procedure involves thermal treatment of the NiMn structures at high temperatures above 400°C to induce the phase change to the fct (face centered tetragonal) structure which shows antifer-

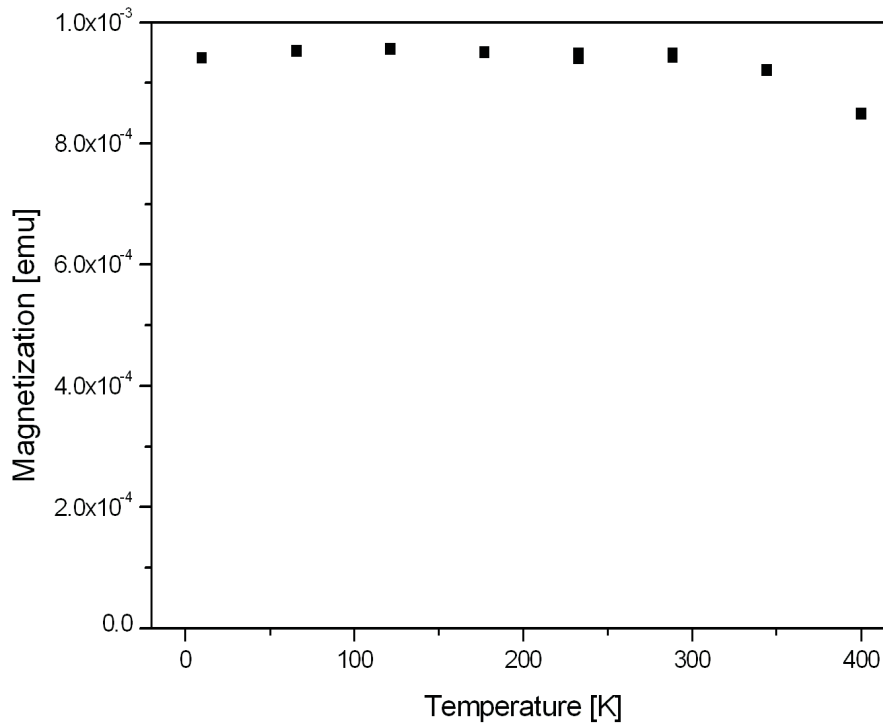


Figure 6.15: Magnetization of a 40 nm thick NiMnSb layer versus temperature. The highest temperature attainable with the SQUID setup was 400K, but the drop of the magnetization from 4K to 400K is  $\approx 5\%$ , which is consistent with an expected Curie temperature of 730K.

romagnetic behavior [Mao98].

The Neel temperature in NiMn furthermore depends on the exact stoichiometry [Sly93]. Neel temperatures of up to 1020 K have been reported so far [Hou00]. However, the maximum temperature where exchange biasing in ferromagnet-antiferromagnet structures can be observed is less than the minimum of the Neel temperature of the antiferromagnet and the Curie temperature of the ferromagnet [Hou00].

To study the exchange biasing of NiMn/NiMnSb structures, samples with a NiMn layers on top of NiMnSb were prepared. After the growth of the NiMnSb layer, the Sb shutter was closed, leaving only the Ni and Mn cell open. Since the sticking coefficient of Ni and Mn are very close to one, a significant deviation from the equiatomic stoichiometry is not expected. Since neither the crystal structure nor the lattice constant of NiMn are matching the properties of NiMnSb, single crystalline growth of NiMn can not be expected. RHEED measurements show at the beginning of the growth the appearance of crystallographic phases differ-

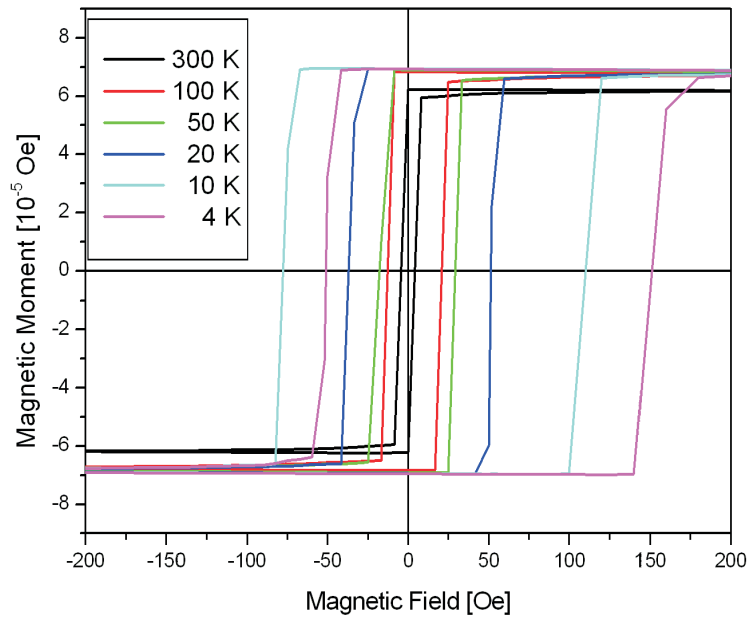


Figure 6.16: Hysteresis curves taken by SQUID of a sample consisting of 5 nm NiMn on top of a 10 nm NiMnSb layer along  $[1\bar{1}0]$  at different temperatures. For temperatures above 20 K, the hysteresis curves are symmetric while for lower temperatures a shift of the origin to higher magnetic fields is observed. Additionally, this measurement shows an increase of the coercive field with decreasing temperature.

ent from the zincblende or half-Heusler phase. In the later stage of the growth a RHEED pattern showing polycrystalline growth is observed. The growth rate of NiMn was estimated to be about 2/3 of the growth rate of NiMnSb.

Due to the temperature instability of the InP substrate, the aggressive NiMn annealing to induce the phase change to the antiferromagnetic fct structure cannot be performed. Since the deposition process itself takes place at an elevated temperature of about 300°C, parts of the NiMn material can crystallize in the desired fct structure. Nevertheless, a drastically reduced Neel temperature is expected. Therefore exchange biasing in these structures is only observable at low temperature.

To study the temperature dependency of the magnetic properties of the NiMn/ NiMnSb structures, a sample with 10 nm thick NiMnSb and 5 nm thick NiMn layers was grown. In the SQUID several hysteresis curves along the easy axis of the sample ( $[1\bar{1}0]$ ) at different temperatures varying from 4 K to room temperature were measured. Fig. 6.16 shows the results of this experiment. For temperatures above 20 K no significant pinning of the ferromagnetic layer by the

antiferromagnet can be observed, whereas for 4 and 10 K a clear asymmetry of the hysteresis curves caused by the exchange biasing effect is shown. The decrease of the coercive field, even for the temperatures where no pinning of the ferromagnet is observed, can be attributed to the increased thermal energy which aids to the magnetic switching process.



# Chapter 7

## NiMnSb/ZnTe/NiMnSb Multilayers

### 7.1 Introduction

The growth of metallic layers on semiconductors is widely used and many material combinations have been found where single crystal epitaxial layers can be produced. The other way round, the growth of semiconductors on metals in an epitaxial process, however, has proved to be a much more demanding task. Especially in cases where the growth of the metal on the semiconductor has been studied in detail, e.g. Fe on GaAs, the growth of the semiconductor on the metal has not been achieved yet. In most cases the crystal structure of the metal is not compatible with the growth of the mostly zincblende semiconductor crystal structure. Nevertheless, metal/semiconductor/metal multilayers would be most interesting since in these cases epitaxial structures can be produced which offer unique opportunities for the experimentalist, like epitaxial TMR stacks. There exist some publications on the growth of e.g. Ge on Au [Oug00]. Nevertheless, this material combination is very special since both metal and semiconductor are elemental which reduce the problems typically occurring during growth like antiphase domains. Furthermore, the growth process used in these experiments is very complex and the growth of Au/Ge/Au multilayers has yet to be reported.

Since the crystal structure of the metal and the semiconductor are essentially the critical parameters for the growth of metal/semiconductor/metal multilayers, materials with a close relationship in their crystal structures are needed. The half-Heusler structure with its 3-atomic basis in a fcc lattice is very closely related to the zincblende 2-atomic basis in the same lattice, therefore the growth of zincblende semiconductor materials on top of a half-Heusler layer, in particular NiMnSb, may be feasible. Experiments show that indeed the epitaxial growth of zincblende semiconductors on NiMnSb and vice versa is possible. Due to the fact that NiMnSb is not only a metal but a halfmetallic ferromagnet (HMF), many ex-

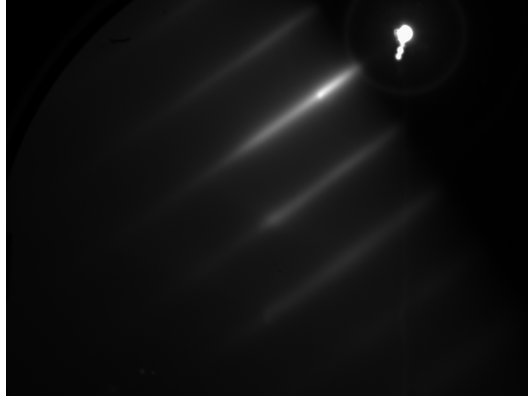


Figure 7.1: RHEED image along the [110] direction of a 1ML thick ZnTe layer on NiMnSb(001). In this direction the surface roughness is low and a clear specular spot is visible.

citing experiments with these epitaxial HMF/SC/HMF structures can be made.

## 7.2 Growth of ZnTe on NiMnSb(001)

Several semiconductor materials have been tried to grow on NiMnSb, the obvious choice is (In,Ga)As. However, since this material needs a growth temperature far above the one of NiMnSb, the growth of (In,Ga)As on NiMnSb does not result in an epitaxial layer. Semiconductor materials which grow at temperatures compatible with NiMnSb are many II-VI semiconductors, like ZnSe or ZnTe. Growth experiments of several II-VI semiconductors have been performed, as will be shown later in section 7.6, but best results were achieved with the growth of ZnTe on NiMnSb(001).

On the InP(001) substrate a (In,Ga)As buffer layer and a NiMnSb layer following the growth process described in sections 4.3 and 4.4 are deposited. Following the growth of the NiMnSb layer, the sample is immediately transferred to the II-VI growth chamber to deposit the ZnTe layer. The growth temperature of the ZnTe layers is set to a temperature between 280 and 300°C, as measured using a thermocouple in thermal contact with the molybdenum-block. This temperature measurement method is different to the method used in the NiMnSb growth chamber, where the thermocouple is not in contact with the molybdenum-block. Therefore, the real temperature of the substrate in the II-VI growth chamber is usually higher than the temperature in the NiMnSb growth chamber with the same reading.

Special care has to be taken to ensure that the NiMnSb surface is exposed to

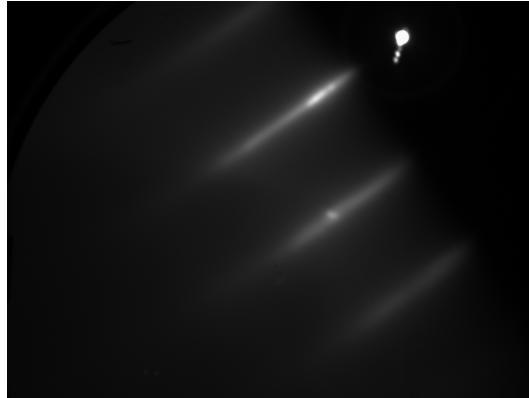


Figure 7.2: RHEED image along the [100] direction of a 1ML thick ZnTe layer on NiMnSb(001). The streaky pattern and the clear specular spot shows the low surface roughness.

a minimum amount of group VI elements like Se and Te. Especially if a large amount of Se was evaporated in a growth process before inserting the NiMnSb sample, surface reactions between the remaining Se and the NiMnSb surface can occur. These reactions result in a pronounced surface roughening which can be observed by RHEED. Successive growth of II-VI material on such a surface results in a drastically reduced quality of the grown material. Also during the growth start group VI contamination of the surface has to be prevented. For that, the sample is exposed to a Zn beam for 40 s before opening the Te shutter. No change in the RHEED pattern is observed during that process. Furthermore, a migration enhanced epitaxy (MEE) growth start is applied. In this case the Te shutter is opened for the time needed to grow exactly 1 ML of ZnTe and then shut again for a few seconds. This method ensures that all Te-atoms impinging on the surface react with a Zn atom already residing there. The MEE growth process is typically used for the first 3 or 4 ML. This thickness is enough to prevent any reactions of the Te-atoms with the NiMnSb surface. After the time needed for this thickness, the normal MBE growth with open Zn and open Te shutters is used. During the MEE growth the RHEED pattern changes to a unreconstructed (1x1) surface (Fig. 7.1 and 7.2).

Since this growth process has an excess of group II atoms, the typical (2x1) reconstructed RHEED pattern characteristic of group VI-rich growth is not observed until the standard MBE growth process is started. The surface roughness during the MEE growth start is quite low, a clear specular spot and a streaky RHEED pattern can be observed at all times. After the growth of  $\approx 8$  ML the surface roughness is getting more pronounced (Fig. 7.3). This is most likely caused by the start of the relaxation process in ZnTe. Note that the thickness at which this

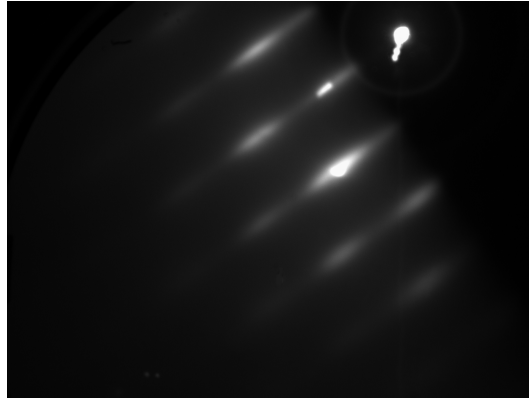


Figure 7.3: RHEED image along the  $[1\bar{1}0]$  direction of a 10 ML thick ZnTe layer on NiMnSb(001). The spotty pattern indicates an increased surface roughness. No signs of  $d/2$  streaks are visible, which would be an indication of Te-rich growth.

roughening is starting is depending on the thickness of the underlying NiMnSb layer. While for 2.5 nm thick NiMnSb the critical thickness is around 8 ML, for 10 nm thick NiMnSb layers this thickness is reduced to about 3 ML.

After some more ML, typically at a thickness of 10 to 12 ML, the typical (2x1) reconstruction of group VI-rich ZnTe is observed.

The lattice constant of ZnTe is 3.9% larger than that of the pseudomorphic NiMnSb. In the literature, the critical thickness of ZnTe on InP has been estimated to be in the 3 nm [Dun91] to 11 nm [Tom96] range. Since both NiMnSb and ZnTe exhibit compressive strain, a critical thickness at the lower end of this range can be expected for epitaxial growth of ZnTe on NiMnSb.

To prevent relaxation, usually ZnTe layers with a thickness of less than 3 nm have been grown for the tri-layer structures. Directly after the growth of the II-VI layer, the sample is transferred back to the NiMnSb growth chamber and the second NiMnSb layer is deposited. The thickness of this second Heusler-layer is limited to values below 20 nm, due to the added strain of the first NiMnSb and the ZnTe layer. The critical thickness of the second NiMnSb layer obviously is also depending on the thicknesses of the first NiMnSb and the ZnTe layer. Also for the second NiMnSb layer, a clear and streaky (2x1) reconstruction appears after the growth of typically 2 ML and remains this way throughout the entire growth.

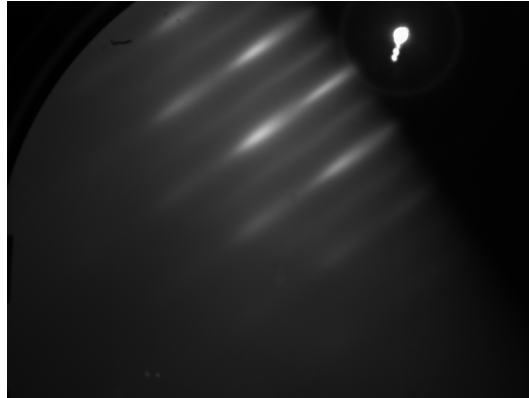


Figure 7.4: RHEED image along the  $[1\bar{1}0]$  direction of a 10 nm thick ZnTe layer on NiMnSb(001). The  $d/2$  streaks are clearly visible, an indication of the Te-rich growth conditions for this layer. The spotty pattern indicates an increased surface roughness, caused by the relaxation of the ZnTe layer which is above its critical thickness at this point.

### 7.3 Structural Properties of NiMnSb/ZnTe/NiMnSb Heterostructures

To check if the growth of ZnTe on NiMnSb is epitaxial and results in single crystalline layers, a special sample for HRXRD measurements was grown. To be able to detect the layers in the diffraction experiments a minimum thickness of 40 nm for pseudomorphic material, which exhibits a low  $\omega$ -FWHM in these experiments, is needed. This minimum thickness is above the critical thickness for ZnTe on InP substrates. The relaxation of the ZnTe layer will also affect the NiMnSb layer, therefore thicker layers which compensate for the increased  $\omega$ -FWHM in relaxed layers are needed. For this reason, the sample consists of 500 nm ZnTe on top of a 200 nm thick NiMnSb layer. Since already the NiMnSb is relaxing during the growth, it is expected that the mosaicity of both layers is quite high. Fig. 7.5 shows the reciprocal space map of the (115) reflection of this sample.

As expected, the thick NiMnSb and ZnTe layers are totally relaxed, while the (In,Ga)As buffer layer is totally strained. This also influences the mosaicity of the layers, both relaxed layers have an increased FWHM in the  $\omega$ -direction, thus exhibiting a large mosaicity. Nevertheless, the whole layer stack is single crystalline.

Diffraction experiments on totally strained NiMnSb/ZnTe/NiMnSb multi-layer structures are not possible since layers of the required thicknesses would create a signal too weak to be detected in the diffraction experiment. Therefore x-ray reflectivity (XRR) measurements have been performed on a typical tri-layer

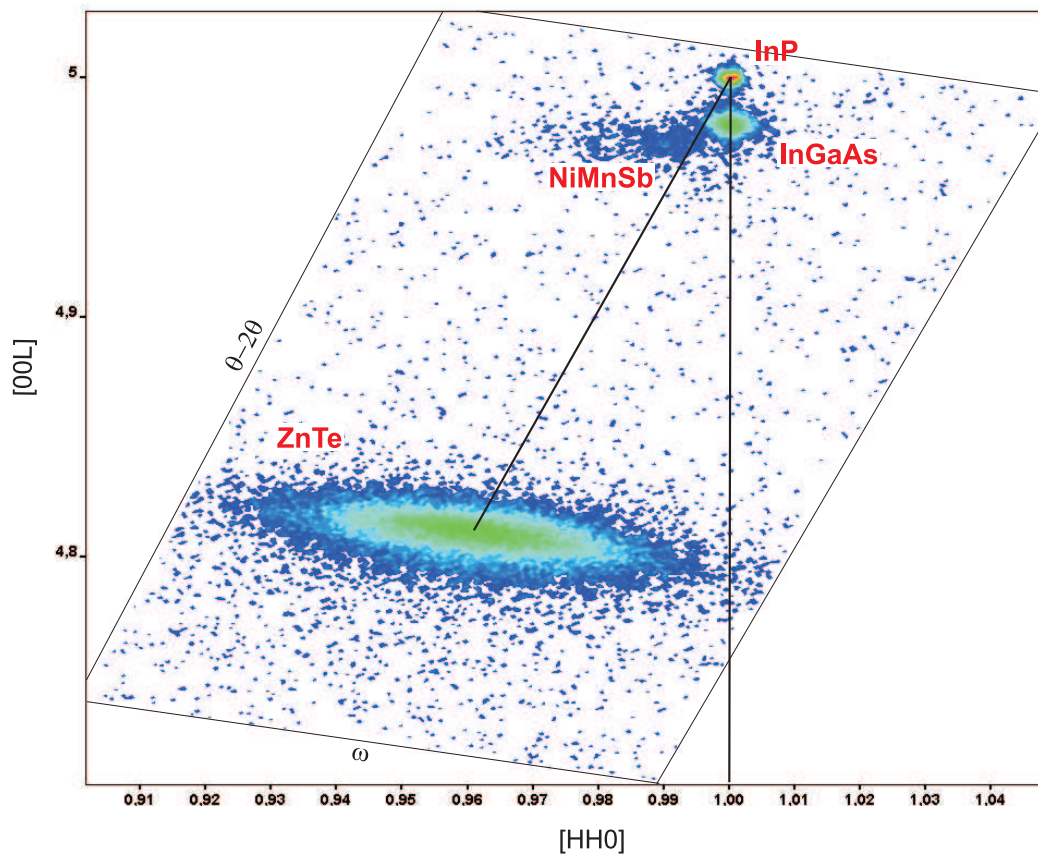


Figure 7.5: HRXRD reciprocal space map of the (115) reflection of a sample consisting of InP substrate, 150 nm (In,Ga)As buffer layer, 200 nm NiMnSb and 500 nm ZnTe. The (In,Ga)As layer is pseudomorphic, identifiable by the  $l$ -value of 1 for its peak (indicated by the vertical line at  $l=1$ ). Both NiMnSb and ZnTe are totally relaxed. Their peaks lie on a straight line along the  $\theta - 2\theta$ -direction. The mosaicity of the NiMnSb and ZnTe layers is high, as can be seen by the increased FWHM of their peaks in the  $\omega$ -direction.

structure at the BW2 beamline of the Hamburger Synchrotron radiation facility by A. Stahl and C. Kumpf of the group of E. Umbach at Würzburg. This technique has the advantage that the x-rays do not have to be diffracted in the different materials, hence there is no minimum thickness of the layers. On the other hand, XRR experiments are not sensitive on the crystal structure. They can only investigate interface roughness, thickness and homogeneity of the layers. The design of a typical NiMnSb/ZnTe/NiMnSb multilayer structure which was examined by XRR is shown in Fig. 7.6. Fig. 7.7 shows the measured data together with our best fit obtained using the FEWFLAY-code [Sti]. The fit reproduces all important

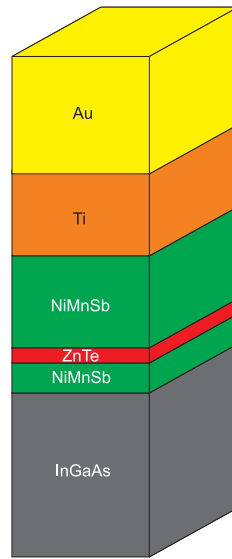


Figure 7.6: Sample design of the NiMnSb/ZnTe/NiMnSb multilayer structure investigated by XRR. The metallic layers on top of the upper NiMnSb layer have been deposited in order to prevent oxidation of the ferromagnets.

features of the experimental data. The obtained fitting parameters are listed in Table 7.1. Layer thicknesses of 10.2 nm, 1.7 nm and 2.6 nm for the upper NiMnSb, the ZnTe and the lower NiMnSb layer, respectively are obtained for this sample. The thickness of the  $\text{In}_{0.53}\text{Ga}_{0.47}\text{As}$  buffer-layer is determined to 168 nm. This actual sample has been covered with protective capping layers, whose thicknesses are also measured in the experiment (10 nm Ti and 30 nm Au), to prevent oxidation during transport to the synchrotron. All RMS-roughnesses as obtained from the fit are small, indicating excellent quality of the epitaxial layers. The largest interface roughness of the NiMnSb and ZnTe layers is 0.6 nm between the ZnTe and the upper NiMnSb layer.

## 7.4 Magnetic Properties of NiMnSb/ZnTe/NiMnSb Heterostructures

One of the goals for NiMnSb/ZnTe/NiMnSb multilayers is their usage for TMR experiments. Therefore, the two ferromagnetic layers have to switch their magnetization at different magnetic fields. As described in section 6.3, NiMnSb(001) shows a strong dependence of its coercive field on the layer thickness. Here, we utilize this observation to induce separate switching of the two magnetic layers in a TMR stack, simply by using two different thicknesses of NiMnSb. In Fig. 7.8

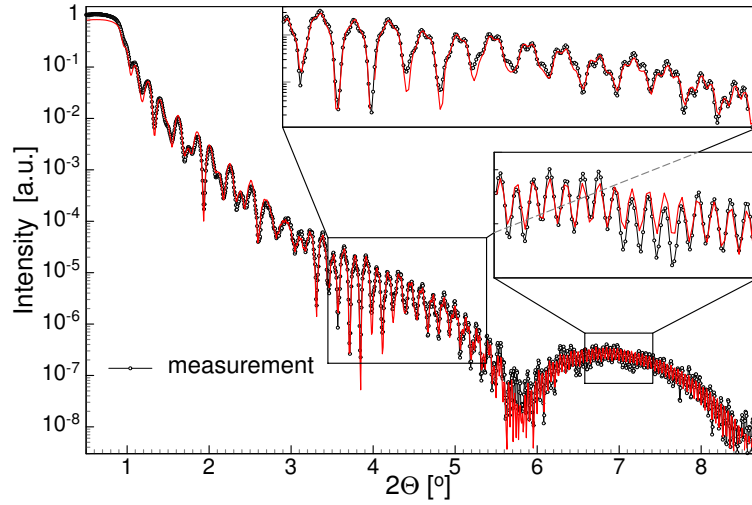


Figure 7.7: Measured XRR data and corresponding best fit. The fit parameters are listed in Table 7.1.

the sample design of a typical structure used for double switching experiments is shown. Fig. 7.9 shows a SQUID measurement of a NiMnSb/ZnTe/NiMnSb structure taken at room temperature, where the upper NiMnSb layer is 4 times thicker than the lower layer (10 nm and 2.5 nm, respectively), while the ZnTe layer is 1.2 nm thick and fully strained. The hysteresis curve clearly shows that the two layers do switch independently, with the thin layer switching at a lower magnetic field than the upper thicker layer. The switching fields differ from those observed by us previously (see section 6.3), pointing at the presence of some magnetic coupling between the two NiMnSb layers. This coupling may also explain the fact that double switching cannot be detected along the easy axis of the two NiMnSb layers, the  $[1\bar{1}0]$  direction. The origin of this coupling is currently still under investigation.

## 7.5 Exchange Bias in NiMnSb/ZnTe/NiMnSb/NiMn Heterostructures

An alternative method to obtain double switching in NiMnSb/ZnTe/NiMnSb multilayers is exchange biasing the top NiMnSb layer with an antiferromagnet. In section 6.4 the exchange biasing of a single NiMnSb layer by a NiMn antiferromagnet has been shown. Therefore it is straight forward to incorporate an additional NiMn layer into the TMR stack. Both NiMnSb layers can now have the same thickness, there is no need to have different coercive fields any more. To



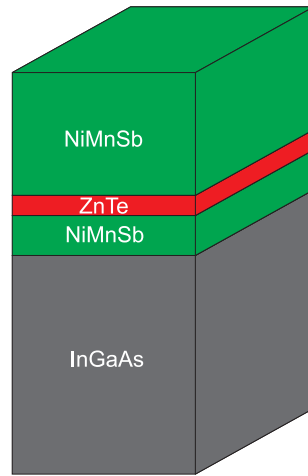


Figure 7.8: Sample design of a tri-layer structure used for double switching experiments. Note the different thicknesses of the two NiMnSb layers which result in different coercive fields of these layers.

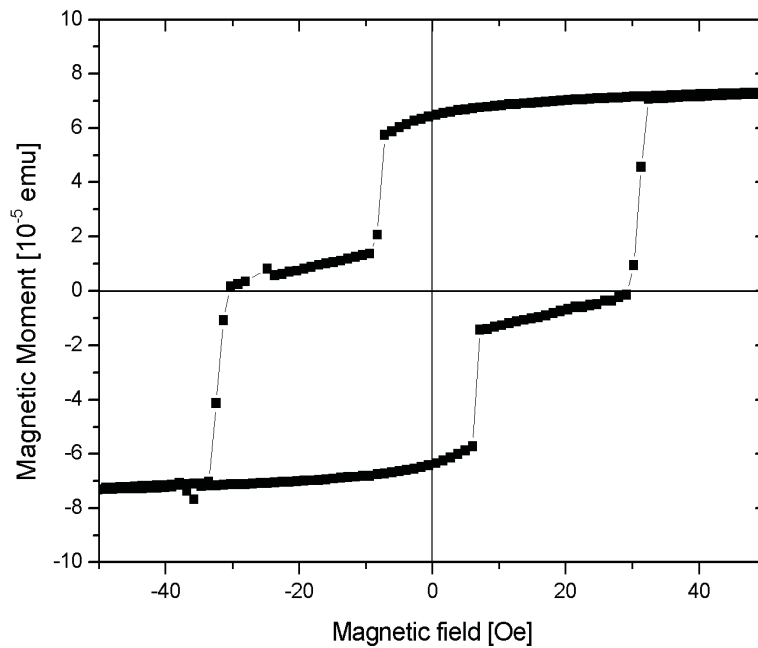


Figure 7.9: SQUID measurement of a sample consisting of a NiMnSb/ZnTe/NiMnSb structure taken at room temperature with the magnetic field aligned along [100]. Thicknesses of the 3 layers are 2.5, 1.2, and 10 nm, respectively.

Table 7.1: Fitting parameters for the x-ray reflectivity data shown in Fig. 7.6. The Au- and Ti capping layers are deposited in order to protect the sample during transport in air. Thickness and roughness at the interface between the listed and subsequent layer is listed in nm, electron density in  $10^{24} \text{ cm}^{-3}$ . Densities missing in the table were fixed to their value calculated from the bulk structure. Errors were estimated from parameter variations during the fitting procedure.

layer	thickness	roughness	electron- density	
			fitted	calc.
Au-cap	30.4(1)	0.62(4)	4.31(5)	4.662
Ti-cap	9.99(5)	0.81(4)	1.25(1)	1.247
NiMnSb	10.24(8)	0.6(1)	1.97(8)	2.022
ZnTe	1.67(5)	0.62(8)	1.44(1)	1.443
NiMnSb	2.58(5)	0.19(2)	2.02(1)	2.022
In <sub>0.53</sub> Ga <sub>0.47</sub> As	168.0(1)	0.22(2)	–	1.400
substrate	–	0.13(4)	–	1.275

test this design, a sample consisting of two NiMnSb layers of identical thickness (5 nm) separated by 1.2 nm ZnTe has been grown. On top of the upper NiMnSb layer a 5 nm thick NiMn film has been deposited. Fig. 7.10 shows the sample design for this experiment. Due to the same coercive field of the two NiMnSb layers double switching can only be observed if the upper ferromagnet is pinned by the NiMn antiferromagnet.

Fig. 7.11 shows a SQUID measurement at 4 K of this sample. The hysteresis loop clearly shows the separate switching of the two layers at high fields, caused by the pinning of the upper NiMnSb layer. That the double switching is absent in the low (down-)field part of the loop points to the presence of residual magnetic coupling across the very thin barrier, as already mentioned in section 7.4.

## 7.6 Alternative Semiconductors

ZnTe has the disadvantage that only very thin pseudomorphic layers are possible on totally strained NiMnSb. Ternary semiconductors like (Zn,Cd)Se or (Zn,Be)Te offer the possibility to adjust the lattice constant of the semiconductor. If the composition is chosen correctly, the ternary semiconductor can be grown lattice matched on NiMnSb. Thus the thickness of both the semiconductor and the second NiMnSb are not subject to that narrow restrictions any more. Additionally, the composition of the ternary compound can be chosen in a way that the semi-

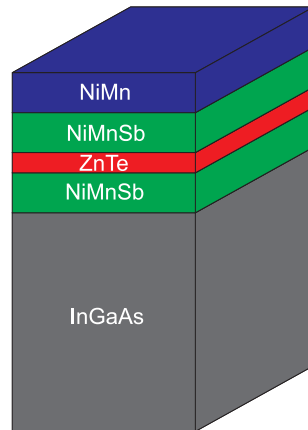


Figure 7.10: Sample design of a TMR stack which utilizes exchange biasing of the top ferromagnetic layer. Note that the two ferromagnetic layers have the same thickness, thus double switching can only occur if the upper NiMnSb layer is pinned by the antiferromagnetic NiMn.

conductor exhibits tensile strain. Thus, the compressive strain of the first NiMnSb layer can be compensated by the ternary semiconductor.

Attempts have been made to grow the ternary compounds (Zn,Be)Te and (Zn,Cd)Se. Although growth of the binary material ZnTe is possible on NiMnSb as has been shown in the previous sections, attempts to achieve lattice matched growth of (Zn,Be)Te on NiMnSb have not been successful so far. This may be partly due to the reason that the optimal growth temperature of Be-containing Tellurides has to be in the range of 350°C [Tou99], a temperature which would already cause damage in the InP substrate and the NiMnSb surface. Lower growth temperatures result in rough surfaces during growth of (Zn,Be)Te. Furthermore, the size of a Be atom is very small compared to Te or the elements of NiMnSb. Diffusion of Be onto the NiMnSb surface is therefore very likely. Experiments with Be atoms impinging directly on a NiMnSb surface have shown the formation of a rough surface which results in polycrystalline growth thereafter. To prevent the diffusion of Be onto the NiMnSb surface attempts to grow ZnTe/BeTe superlattices have been made. The resulting surface quality was quite poor, probably due to the too low growth temperature or the insufficient prevention of Be diffusion onto the NiMnSb surface.

The growth of (Zn,Cd)Se shows similar problems. From the three materials, reactions of both Cd and Se with the NiMnSb form defect centers at the surface. Additionally, even the growth of binary Se containing semiconductors has been unsuccessful due to the formation of defects at the surface.

A third material combination, Zn(Se,Te), has the potential to grow lattice

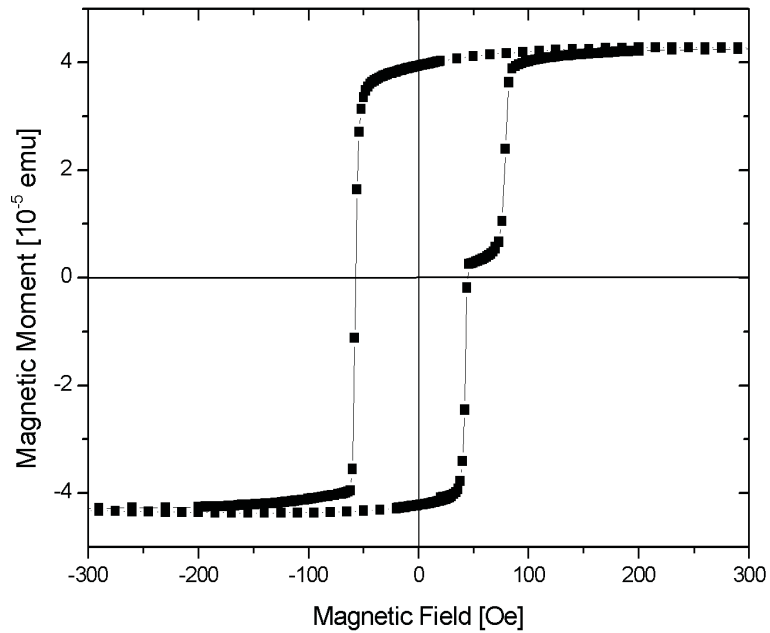


Figure 7.11: SQUID measurement of a sample consisting of a NiMnSb/ZnTe/NiMnSb/NiMn structure taken at 4K with the magnetic field aligned along  $[1\bar{1}0]$ . Thicknesses of the 4 layers are 5, 1.2, 5 and 5 nm, respectively.

matched on NiMnSb. This material is studied intensely at the moment. First results for the growth on NiMnSb are promising.

# Chapter 8

## Growth of NiMnSb on (111) Oriented Materials

### 8.1 Introduction

Zincblende crystals, or in general, crystals with a fcc lattice and a basis consisting of more than one element, have several possible terminations of the (111) surface. Due to the inversion asymmetry of the zincblende crystal through a plane parallel to the (111) surface, different atom configurations at the surface are possible. There are in principal two types of (111) surfaces, the (111)A and the (111)B surface. Multiplied by the number of elements inside the zincblende crystal, which could terminate the crystal, the total number of surface terminations are four.

Figs. 8.1 to 8.4 show the four surface orientations. Note that the two principal surface orientations, the (111)A and (111)B can be transformed into each other by exchanging the elements. The cleaving edges are along the  $(1\bar{1}0)$ ,  $(10\bar{1})$  and  $(01\bar{1})$  planes. These planes are symmetrically identical, an asymmetry between the different cleaving edges as for zincblende crystals with a (001) surface orientation does not exist. The three cleaving edges enclose an angle of  $60^\circ$ . The cleaved pieces therefore have the shape of an equilateral triangle. The symmetry of the cleaving edges will also have its consequences on the RHEED patterns. Different reconstructions along different cleaving edges, an observation which is very common for the (001) oriented crystals (see section 4.4), cannot be expected.

MBE growth on (111) oriented substrates faces additional problems compared to the growth on (001) terminated samples. The number of free bonds on top of a (001) orientation is always two, independent of the terminating element. As shown in Figs. 8.1 to 8.4, for the (111) orientation the dangling bonds are one for the first element and three for the second. An atom impinging on the surface has a greater sticking coefficient if its potential bonding partners have three dangling

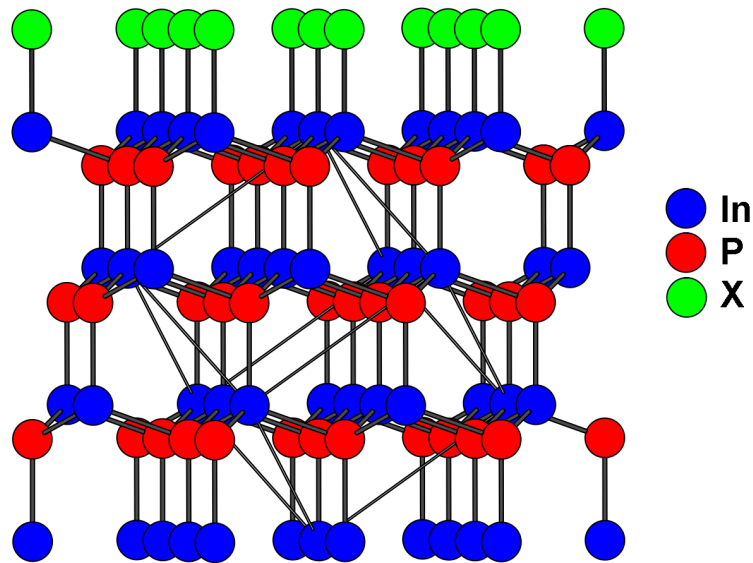


Figure 8.1: Schematic of an InP crystal with a (111)A surface orientation, terminated by In atoms. In atoms are blue, P atoms red and the atoms of the first layer of a different material grown on top of this InP (111)A crystal is green. In this case the surface is terminated with In atoms, which have one remaining bond to attach to the next layer (green). For clarity, the cubic unit cell of the InP crystal is marked with thin borders.

bonds than if they only have one. For example in the case of InP growth on an InP(111)B surface, the sticking probability of P is enhanced, since all In atoms at the surface have three free bonds to attach to the arriving P. Incoming In atoms at the other hand face only one dangling bond from the P atoms at the surface, thus resulting in a reduced sticking probability. In the case of (111)A surfaces, the reduced sticking probability exists for P and the enhanced one for In.

Furthermore, the  $60^\circ$  rotational symmetry can cause a defect type unknown for the growth on (001) surfaces: The fundamental difference between the wurtzite crystal structure and the zincblende structure is merely a  $60^\circ$  rotation along its [0001] or [111] direction respectively. Therefore zincblende crystals can accommodate wurtzite growth easily. A stacking fault during zincblende (111) growth can be described as the insertion of one ML of wurtzite structure in between a two layers of zincblende rotated by  $60^\circ$  along the (111) direction. This type of stacking fault therefore results in a rotation twin defect. Fig. 8.5 shows a schematic of a rotation twin defect. A different problem occurs from the relatively inert (111) surface. Since on a flat (111) surface the probability that an impinging atom is sticking to the surface is low, atoms are likely to attach to existing steps on the surface. On a totally flat (111) surface these steps are formed by an atom

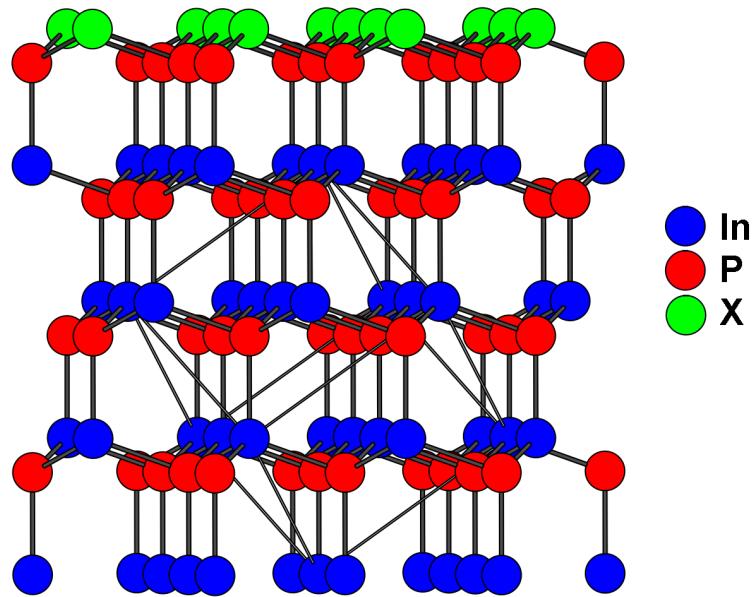


Figure 8.2: Schematic of an InP crystal with a (111)A surface orientation, terminated by P atoms. In atoms are blue, P atoms red and the atoms of the first layer of a different material grown on top of this InP (111)A crystal is green. In this case the surface is terminated with P atoms, which have three remaining bonds to attach to the next layer (green). For clarity, the cubic unit cell of the InP crystal is marked with thin borders.

incorporated at an arbitrary place next to this atom at the surface. Additional atoms are preferably attaching to this atom. In this way other surface planes than the (111) plane are formed which may have a higher sticking probability for the arriving atoms. The growth therefore proceeds in the direction of the planes with the highest sticking probability and thus the highest growth speed. This results in pyramid like facets which add to the surface roughness.

A countermeasure against the formation of rotation twin defects and pyramid like facets at the surface is the usage of substrates with a surface that is not straight (111) oriented, but a few degrees off. By this offset steps at the surface in the direction of the miscut are created, which act as nucleation centers. The atoms are attaching to the step, causing the step to grow in the direction of the miscut, forming the so called “step flow” growth mode. In the real world the above mentioned defects and facets cannot be entirely prevented by using vicinal surfaces, but their density can be reduced drastically.

For the growth studies in the following chapters only vicinal substrates with a miscut of 1 to 2° along  $(1\bar{1}0)$  or  $(11\bar{2})$  have been used.

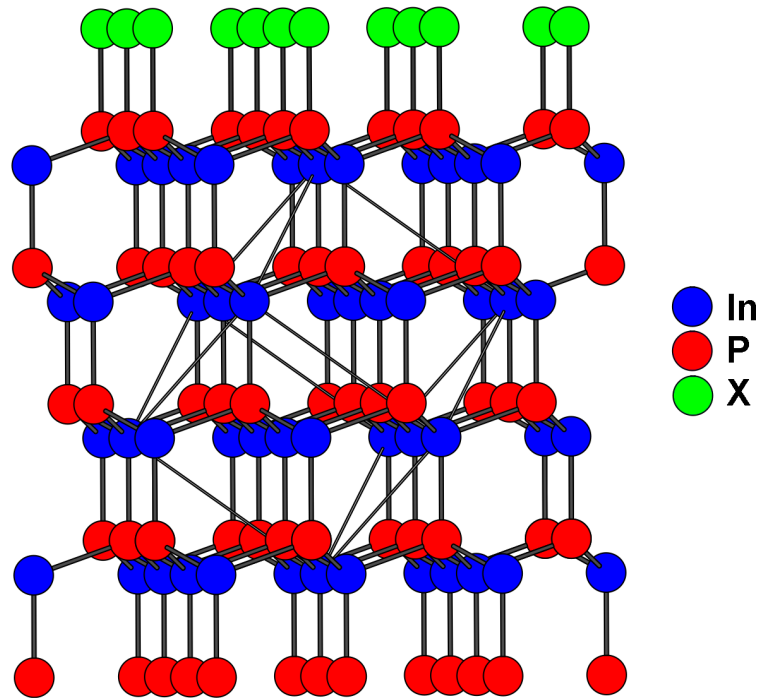


Figure 8.3: Schematic of an InP crystal with a (111)B surface orientation, terminated by P atoms. In atoms are blue, P atoms red and the atoms of the first layer of a different material grown on top of this InP (111)B crystal is green. In this case the surface is terminated with P atoms, which have one remaining bonds to attach to the next layer (green). For clarity, the cubic unit cell of the InP crystal is marked with thin borders.

## 8.2 Growth on InP(111)A

In this section the growth of (In,Ga)As and NiMnSb on InP (111)A (Figs. 8.1 and 8.2) are described. In this surface configuration, a P terminated InP surface has three dangling bonds and an In terminated surface has one dangling bond to receive the impinging atoms.

### 8.2.1 Growth of (In,Ga)As on InP(111)A

As mentioned in section 4.3, the oxide layer on top of epi-ready InP substrates has a crystalline ordering which can be picked up using RHEED measurements. In the case of (111)A substrates, a (1x1) pattern can be observed at room temperature. During the heating of the substrate, the (1x1) pattern changes to a (2x2) reconstruction at  $\approx 490^\circ\text{C}$ . Unfortunately, the RHEED reconstruction of the P terminated InP surface is also a (2x2) reconstruction. The most prominent differ-



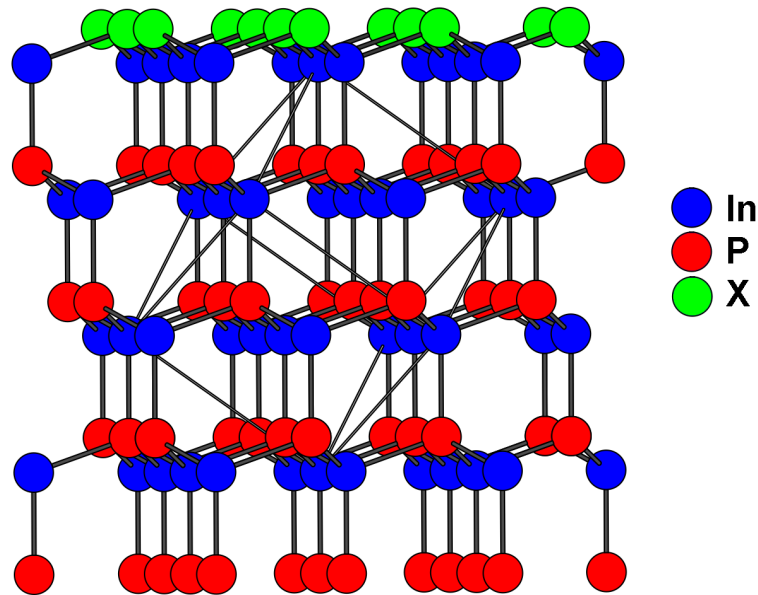


Figure 8.4: Schematic of an InP crystal with a (111)B surface orientation, terminated by In atoms. In atoms are blue, P atoms red and the atoms of the first layer of a different material grown on top of this InP (111)B crystal is green. In this case the surface is terminated with In atoms, which have three remaining bonds to attach to the next layer (green). For clarity, the cubic unit cell of the InP crystal is marked with thin borders.

ence is the appearance of the specular spot. Since the difference between the two (2x2) reconstructions is only marginal, a sudden change in the RHEED pattern to calibrate the substrate temperature during growth, as for the growth on (001) oriented InP substrates, is not possible. The composition of the (In,Ga)As buffer layer critically depends on the exact substrate temperature, therefore the ratio of In to Ga tends to change from growth to growth. To achieve a minimum surface roughness, the density of pyramid like facets has to be reduced as much as possible. These facets are mainly caused by atoms, which are incorporated at the surface far from the steps induced by the miscut. Therefore increasing the migration length of the atoms at the surface reduces the incorporation of atoms away from the steps and thus decreases the density of facets. The migration length in an MBE process depends on several factors, the most dominant is the substrate temperature. The higher the substrate temperature, the longer the path of the atoms on the surface until they are incorporated into the crystal. In the case of (In,Ga)As growth, however, the maximum growth temperature is limited by the sticking probability of In, which decreases drastically for substrate temperatures above 530°C. The optimal growth temperature is therefore close to this value. An-

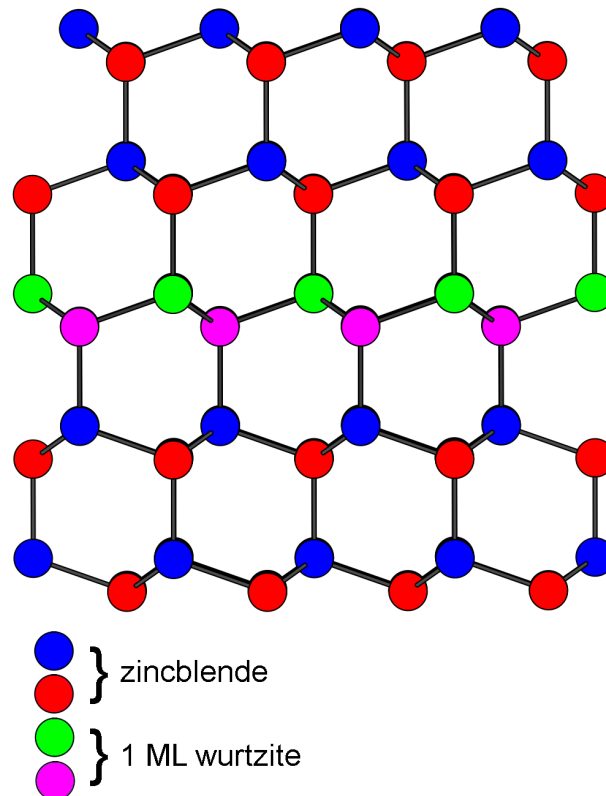


Figure 8.5: Schematic of a rotation twin defect. The ML wurtzite is marked with green and violet atoms. Note that the zincblende crystal above the wurtzite ML is rotated  $60^\circ$  against the zincblende crystal below the wurtzite layer.

other factor influencing the migration length is the III/V ratio. A group III atom moving around at the surface has a very high probability to stick to its place if it reacts with an incoming As atom. Therefore the lesser the As content at the surface, the larger the migration length of the Ga atoms. In the (111)A case the Ga at the surface has only one dangling bond to capture the As, therefore the sticking coefficient of As is very low. Since the growth of (In,Ga)As takes place above the segregation temperature of InP (see section 4.3), a too low As flux leads to In droplets and thus to oval defects which drastically increase the surface roughness of the sample.

Growth of the (In,Ga)As layer has been performed in the following way: To desorb the oxide layer from the InP surface, the sample is heated to the desorption temperature of  $540^\circ\text{C}$ . To achieve a low temperature gradient at the surface, temperature is increased with a rate of  $20\text{K}/\text{min}$ . Above the InP segregation temperature of  $350^\circ\text{C}$  the As valve and shutter are opened. Since the exact desorption temperature is not clearly identifiable, the temperature is ramped up to  $540^\circ\text{C}$  and

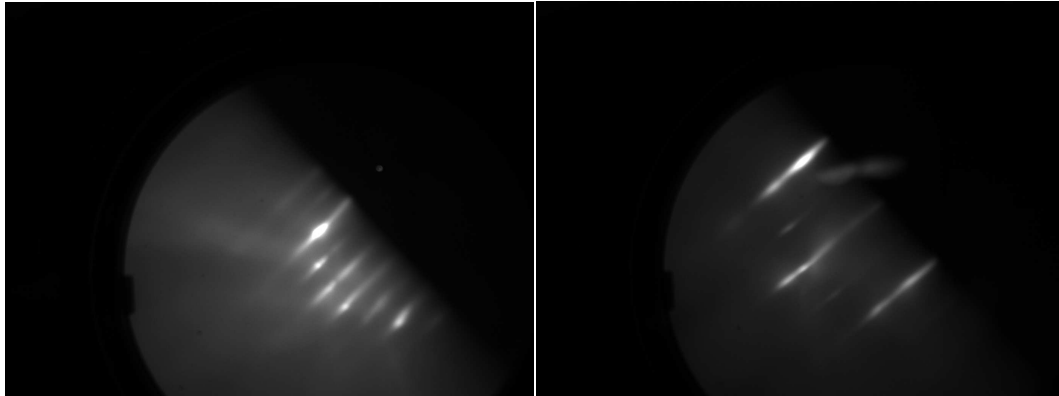


Figure 8.6: RHEED pattern of an (In,Ga)As layer on an InP (111)A surface during growth at 530°C along  $[1\bar{1}0]$ (left) and  $[11\bar{2}]$  right. The  $d/2$  streaks are very clear along  $[1\bar{1}0]$ , as is the sharp specular spot indicating pseudomorphic growth. Along  $[11\bar{2}]$  the  $d/2$  streaks are not as clear as in the  $[1\bar{1}0]$  direction but still identifiable. The surface roughness indicated by the modulated main streaks is caused by the miscut of the substrate in exactly this direction.

left there for one minute until cooling down to the growth temperature of 530°C. To reduce the temperature gradient on the surface, the sample is left for 30 s at the growth temperature before initiating the growth by simultaneously opening the In and Ga shutter. As mentioned above, the clean InP shows a (2x2) RHEED reconstruction. After the growth start, no change of this pattern can be observed.

However, if the In/Ga ratio is off so that the lattice mismatch of the (In,Ga)As to InP causes the buffer layer to relax during growth, this relaxation is indicated by the disappearance of the specular spot. Fig. 8.6 shows the surface reconstructions obtained by RHEED along the  $[1\bar{1}0]$  and the  $[11\bar{2}]$  axis at the beginning of the (In,Ga)As growth. The  $d/2$  streaks are visible in both directions. If the growth is interrupted by closing the As shutter, metal droplets probably consisting of In are forming on the surface, causing a pronounced surface roughening which can be detected by RHEED. A growth interruption by closing the In and Ga shutters has no effect at all on the surface reconstruction, the growth can continue after the interruption without change. After the growth the sample is cooled down to 200°C for transfer into the NiMnSb growth chamber. Above 350°C the cooling process takes place under As flux. The (2x2) reconstruction in both directions gets more pronounced during this process (Fig. 8.7).

The optimum III/V ratio was determined by growing a set of samples with different III/V ratios and measuring the surface roughness of each layer. The three samples are grown with a III/V ratio of 0.07, 0.05 and 0.03. Nomarski microscopy images show the extend of pyramid like facets and oval defects on the

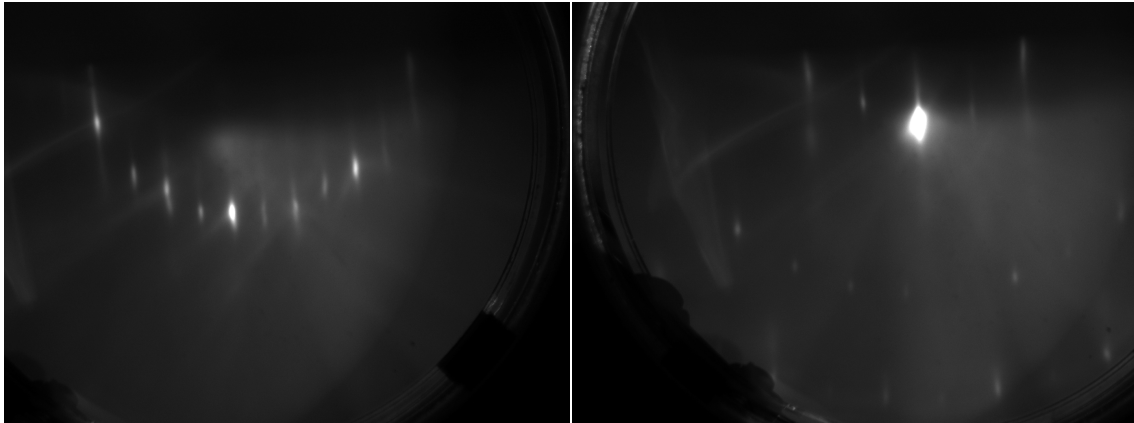


Figure 8.7: RHEED pattern of an (In,Ga)As layer on an InP (111)A surface after growth at 250°C along  $[1\bar{1}0]$ (left) and  $[11\bar{2}]$  right. The  $d/2$  streaks are very clear in both directions. The streaky pattern indicates a flat surface, the sharp and clear specular spot a pseudomorphic (In,Ga)As layer.

surface.

Fig. 8.8 shows an image obtained by Nomarski microscopy of the sample grown with the III/V ratio of 0.07. Large and high pyramids are visible on the surface which are probably caused by overgrowth of In droplets at the surface. The As flux was therefore not high enough to suppress the formation of In droplets at the surface. Furthermore, small pyramid like facets on this surface show that the growth mechanism on this surface is still not optimal. In Fig. 8.9 the image of the (In,Ga)As surface grown with a III/V ratio of 0.03 is shown. Large pyramids indicating In droplets at the InP/(In,Ga)As interface do not exist. Nevertheless, small pyramid like defects can still be found on the surface. This III/V ratio is therefore low enough to suppress the formation of In droplets during desorption of the oxide layer. However, this sample series did not reveal the optimum growth conditions for smooth surfaces of (In,Ga)As on InP(111)A. Even for the samples with the largest III/V ratio the formation of pyramid like facets was not prevented entirely. This ratio is even high enough to allow for the formation of In droplets during the degassing process. Therefore, more experiments are needed to obtain an optimum surface quality. Especially the role of the degassing temperature and the As flux during the degassing process are important to investigate.

### 8.2.2 Growth of NiMnSb on InP(111)A

For the growth of the NiMnSb layer the same principle was used as for the growth on (001) oriented materials (see section 4). Directly after the growth of the

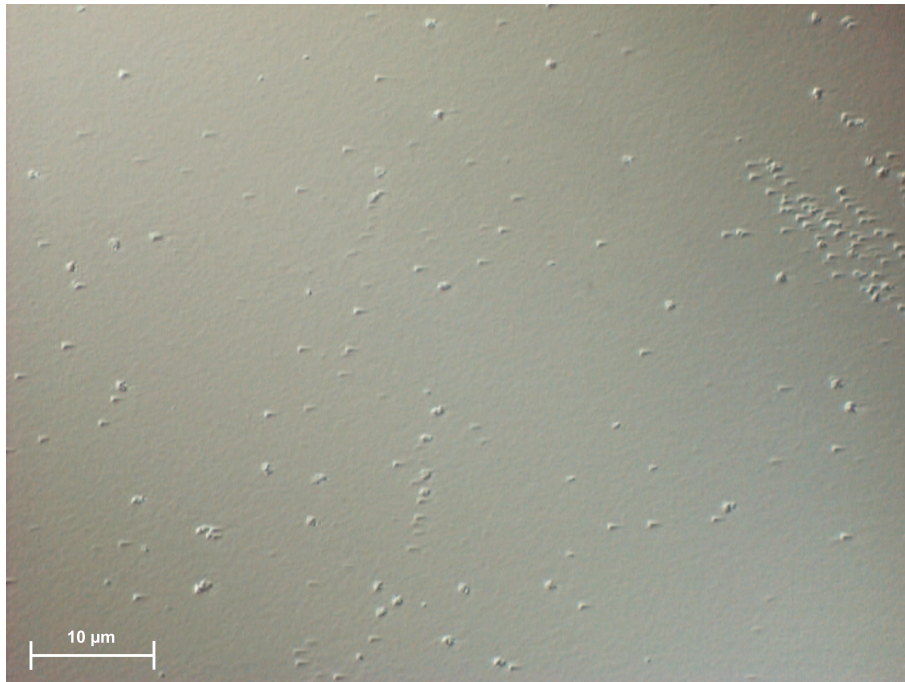


Figure 8.8: Image of an (In,Ga)As buffer on InP(111)A grown with a III/V ratio of 0.07, as obtained by Nomarski microscopy. The surface roughness is dominated by large pyramids, probably caused by overgrowth of In droplets. Additionally, small pyramids are in between the large ones, indicating that the formation of pyramid like facets was not entirely suppressed.

(In,Ga)As buffer the sample was transferred under UHV into the NiMnSb growth chamber. The sample was then heated to the growth temperature of 250°C. As mentioned earlier, to let the fluxes of the three materials stabilize the shutters of their cells were opened three minutes before starting the growth by opening the main shutter. The flux ratios were set to the optimum values determined for the growth on InP(001), Sb/Ni to 10.0 and Mn/Ni to 3.0. The growth starts with an unreconstructed surface but after  $\approx 60$  seconds which corresponds to a thickness of 4 ML, the surface reconstruction changes into a reconstructed pattern. Along  $[1\bar{1}0]$  a (2x2) reconstruction can be observed (Fig.8.10) while along  $[11\bar{2}]$  a (6x6) reconstructed pattern is visible.

During growth the surface reconstruction changes one more time, after the growth of typically 10 nm. At this point the specular spot gets more diffuse, the (2x2) reconstruction changes to a unreconstructed pattern (Fig. 8.11) and the (6x6) reconstruction is reduced to a (3x3) reconstruction. Especially the disappearance of the specular spot indicates that a relaxation process takes place at this stage of the growth. The surface roughness of the NiMnSb layers is mainly influenced by

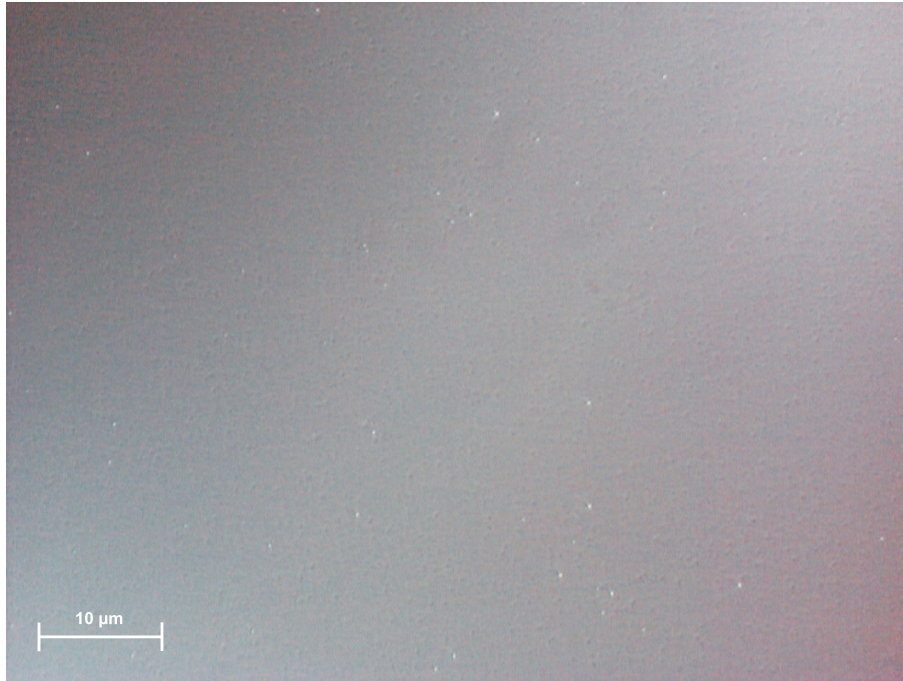


Figure 8.9: Image of an (In,Ga)As buffer on InP(111)A grown with a III/V ratio of 0.03, as obtained by Nomarski microscopy. The high pyramids observed for the samples with higher III/V ratio are missing in this sample. However, the surface still shows a surface roughness caused by small pyramid like facets.

the (In,Ga)As buffer underneath. From Nomarski microscopy no increase of the surface roughness in comparison with the (In,Ga)As buffer can be observed.

### 8.3 Growth on InP(111)B

In this section the growth of (In,Ga)As and NiMnSb on InP (111)B is described. In this surface configuration a P terminated InP surface has one and an In terminated surface three dangling bonds to attach to the arriving atoms.

#### 8.3.1 Growth of (In,Ga)As on InP(111)B

As for the other surface configurations described above, the epi-ready InP(111)B surface also has an oxide layer on top which shows signs of crystalline ordering. To evaporate this oxide layer from the InP substrate, the sample is heated with an increase of 20K/min to a temperature of 540°C and left there for one minute. Above a temperature of 350°C an As flux of is applied to prevent the segregation

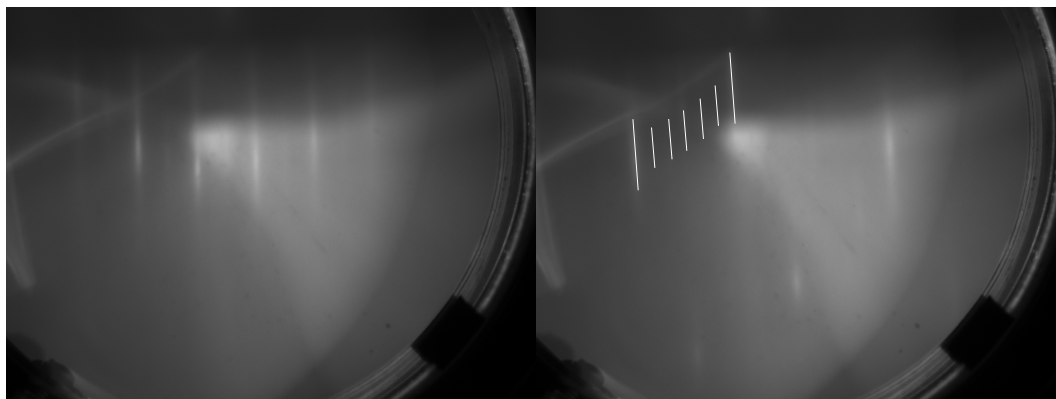


Figure 8.10: RHEED pattern of a NiMnSb surface on InP (111)A during growth at 250°C along  $[1\bar{1}0]$ (left) and  $[11\bar{2}]$ (right). Along  $[1\bar{1}0]$  weak  $d/2$  streaks are visible whereas along  $[11\bar{2}]$  a 6-fold reconstruction is apparent. In this direction the  $d/2$  and their direct neighbors are quite strong. The streaks next to the main streaks, however, are very weak and only visible at optimum conditions. The positions of the streaks are marked for clarity.

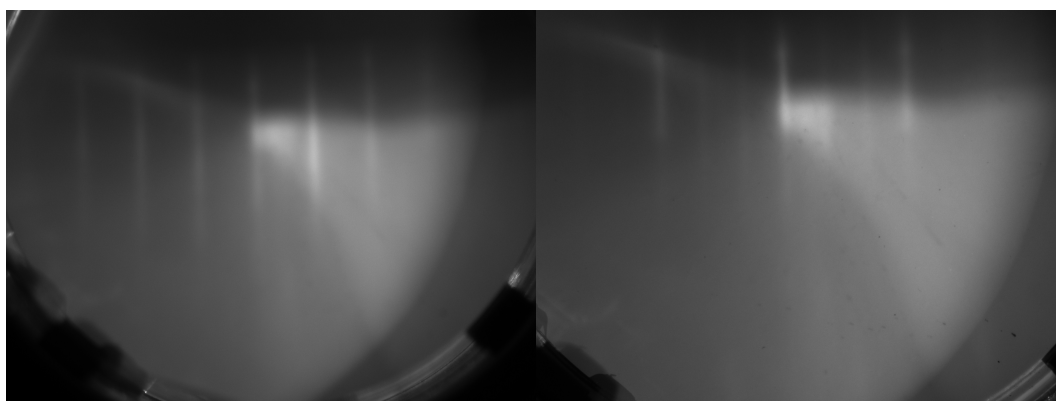


Figure 8.11: RHEED pattern of a NiMnSb surface on InP (111)A during growth at 250°C along  $[1\bar{1}0]$ (left) and  $[11\bar{2}]$ (right) after 120 nm. Whereas along  $[1\bar{1}0]$  no second order streaks are visible, along  $[11\bar{2}]$  the  $d/3$  streaks are clear and easily identifiable. No  $d/2$  streaks can be recognized in contrast to the pattern obtained for thin NiMnSb layers.

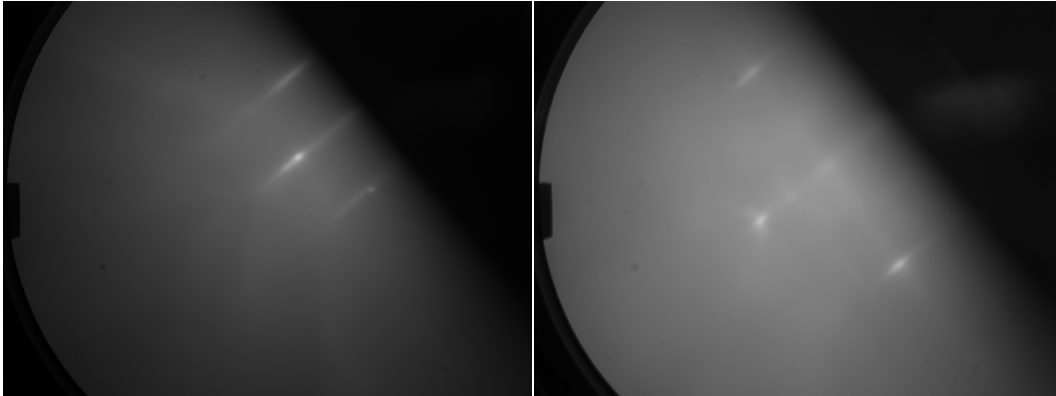


Figure 8.12: RHEED pattern of the epi-ready oxide layer on top of InP(111)B along  $[1\bar{1}0]$ (left) and  $[11\bar{2}]$ (right) at  $400^\circ\text{C}$ . In no direction a reconstruction can be observed.

of InP which would result in In droplets at the surface as already discussed in section 4.1. The RHEED pattern of the oxide layer shows no reconstruction up to  $490^\circ\text{C}$  (Fig. 8.12). From this temperature to  $510^\circ\text{C}$  a  $(2\times 2)$  reconstruction appears (Fig. 8.13), which is then changed into an unreconstructed surface again. During desorption of the oxide layer no change of the RHEED pattern can be observed. As already mentioned for the growth on InP(111)A, calibration of the substrate temperature by observing the desorption point by RHEED is not possible. Therefore the good control over the substrate temperature which is needed for exact adjustment of the In/Ga ratio in the buffer layer is not achieved. Thus variations of the In/Ga ratio and therefore the lattice constant of this layer are expected from growth to growth on InP(111)B. After the desorption process the sample is cooled down to the growth temperature of  $530^\circ\text{C}$ , where it was left for 30 s to achieve a low temperature gradient at the substrate surface. Growth is initiated by simultaneous opening of the In and Ga shutters. No change of the RHEED pattern can be observed during the growth start. Also the (In,Ga)As layer shows an unreconstructed surface during growth (Fig. 8.14). If the growth is interrupted by closing the In and Ga shutters, no change of the RHEED reconstruction can be observed. After the interruption the continued growth shows no change compared to the growth before the interruption. If the growth is interrupted by shutting off the As flux, however, an immediate roughening of the surface is observed, which is probably caused by the formation of In droplets at the surface.

After the growth, the sample is cooled down to  $200^\circ\text{C}$  for transfer into the NiMnSb chamber. Above a temperature of  $350^\circ\text{C}$  the cooling process is done under As-flux. The RHEED pattern changes below  $490^\circ\text{C}$  to a  $(2\times 2)$  pattern along  $[1\bar{1}0]$  combined with a  $(4\times 4)$  pattern along  $[11\bar{2}]$  (Fig. 8.15). This reconstruction



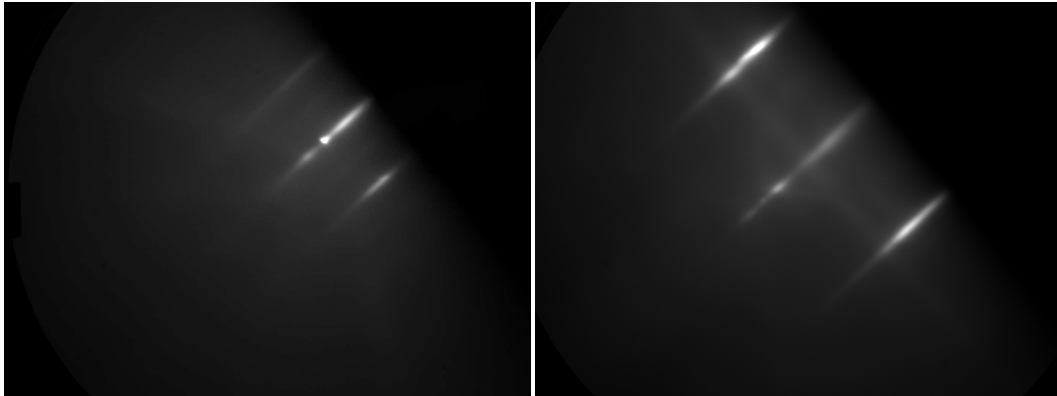


Figure 8.13: RHEED pattern of the epi-ready oxide layer on top of InP(111)B along  $[1\bar{1}0]$ (left) and  $[11\bar{2}]$ (right) at  $500^{\circ}\text{C}$ . In both direction weak  $d/2$  streaks can be observed.

does not change during the rest of the cooling process.

As mentioned earlier, the surface roughness of the (In,Ga)As layer is essentially influenced by the III/V ratio and the substrate temperature. For long migration lengths of the In and Ga atoms at the surface, a high substrate temperature and a high III/V ratio are necessary. Since the In sticking coefficient drops quickly below 1 for temperatures above  $530^{\circ}\text{C}$ , this limit is used as the growth temperature. To obtain the optimum III/V ratio, a set of samples with varying III/V ratios were grown. The ratios used varied from 0.03 to 0.12.

Figs. 8.16 and 8.17 show the Nomarski microscopy images of the samples grown with a III/V ratio of 0.03 and 0.12, respectively. Whereas for the lower ratio a very high density of pyramid like facets is evident, the density is slightly reduced for the larger III/V ratio. The increased migration length of the In and Ga atoms on the surface by the reduced As amount therefore leads to less defects during growth. Nevertheless, the surface quality is still far from being optimal. Since formation of In droplets during desorption plays an important role for the growth of (In,Ga)As, the III/V ratio during desorption was also varied. For the samples mentioned above, the same III/V ratio during desorption and growth was used. Fig. 8.18 shows a Nomarski microscopy image of a sample grown with a III/V flux ratio of 0.03 during desorption to prevent the formation of In droplets and a ratio of 0.12 during growth of the (In,Ga)As to increase the migration length of the In and Ga atoms. As can be seen clearly, the density of pyramid like defects is drastically reduced in comparison to the samples described above.

Experiments trying to evaluate the role of the growth and desorption temperature on the surface roughness were also performed. However, the difference of the surface roughness between two samples grown under nominally identical

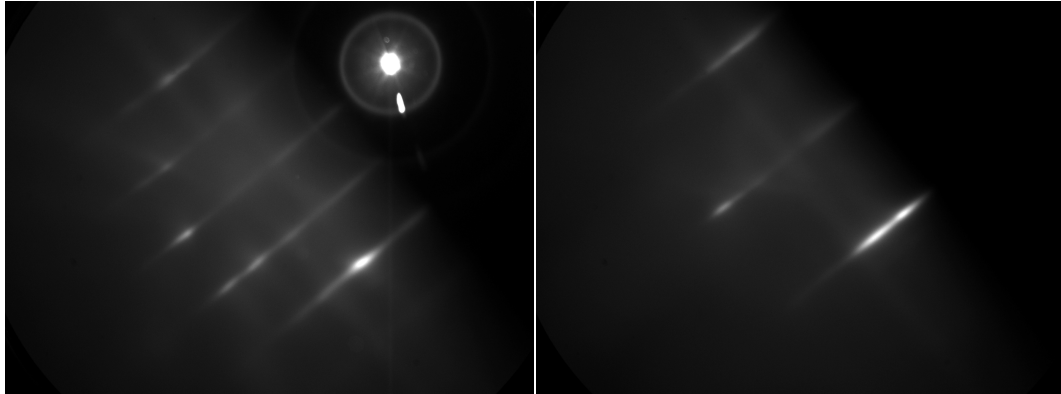


Figure 8.14: RHEED pattern of a 15 nm thick (In,Ga)As on InP(111)B during growth at 530°C. The left picture shows the pattern along  $[1\bar{1}0]$ , the right along  $[11\bar{2}]$ . In no direction a reconstruction can be observed. The specular spot is sharp, indicating a low surface roughness.

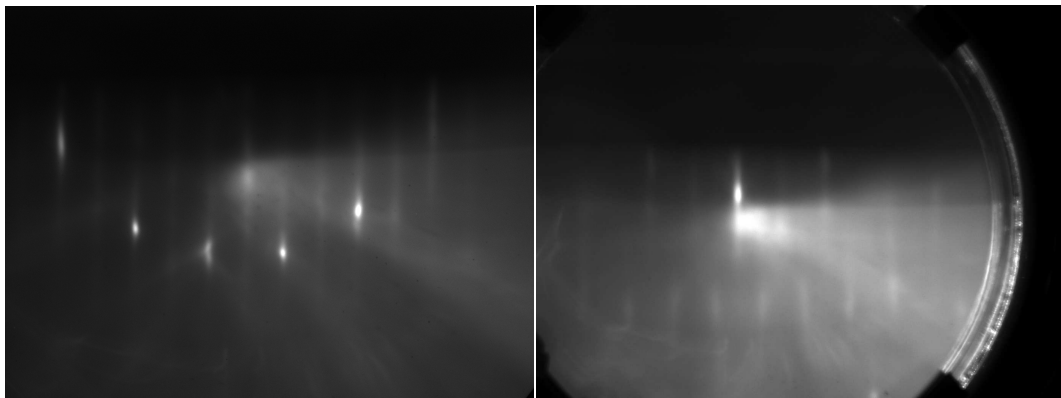


Figure 8.15: RHEED pattern of a 200 nm thick (In,Ga)As layer on InP(111)B at 250°C. Along  $[1\bar{1}0]$  (left) clear  $d/2$  streaks are visible, along  $[11\bar{2}]$  (right) the  $d/4$  streaks are quite hard to identify. The specular spot is sharp and clear in both directions, indicating a low surface roughness of this layer.

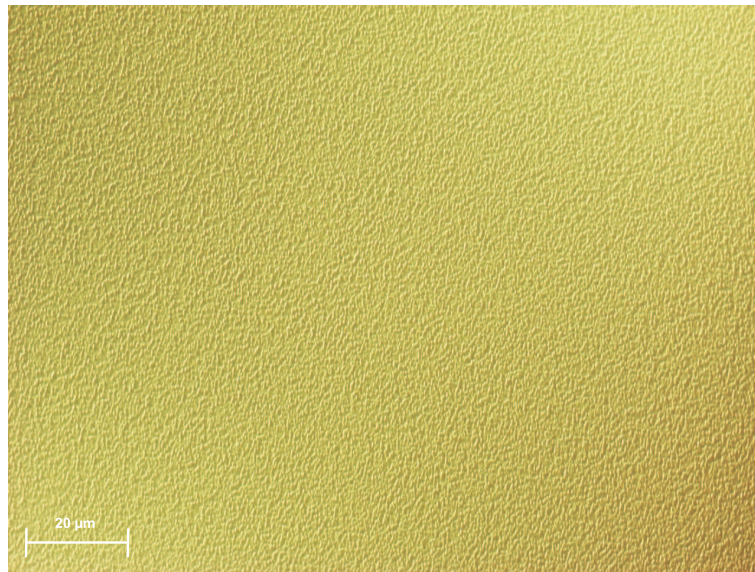


Figure 8.16: Nomarski microscopy image of an (In,Ga)As layer on InP(111)B grown with a III/V ratio of 0.03. A very high surface roughness is evident, the density of the pyramid like facets is that high that they already overlap.

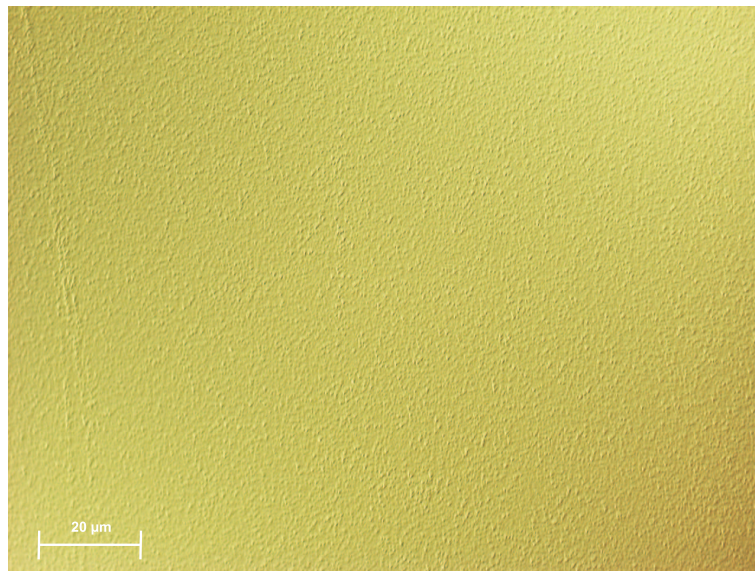


Figure 8.17: Nomarski microscopy image of an (In,Ga)As layer on InP(111)B grown with a III/V ratio of 0.12. The surface roughness caused by pyramid like defects is still visible, but the density of the facets is reduced as compared to Fig. 8.16.

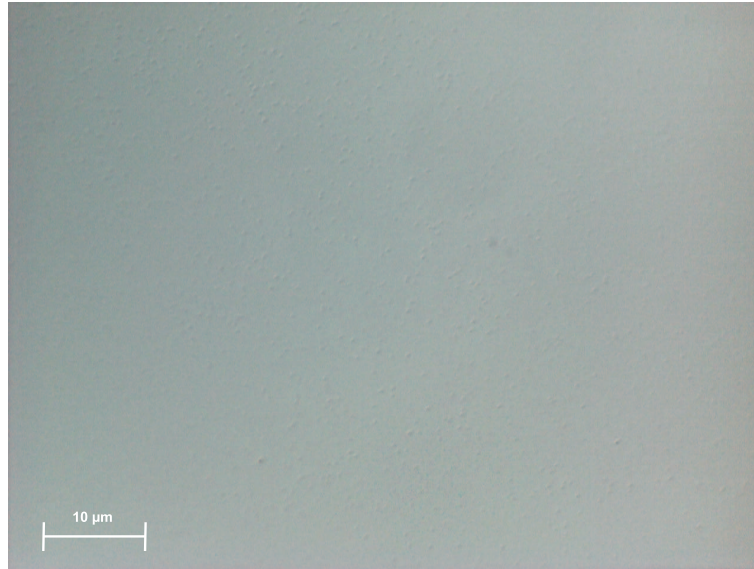


Figure 8.18: Nomarski microscopy image of an (In,Ga)As layer on InP(111)B grown with a III/V ratio of 0.12. Here the III/V flux ratio during degassing was set to 0.03. This sample still shows some pyramid like defects, nevertheless the density is highly reduced in comparison to the images seen above.

conditions is comparable to the difference between two samples with different substrate or desorption temperature. This indicates that a very good control over the substrate temperature is needed, which is not provided by only measuring the thermocouple temperature at the backside of the molybdenum-block. Calibration of the substrate temperature during growth by observation of the desorption point by RHEED as used for the growth on InP(001) is not possible for the growth on InP(111)B. Therefore, without reliable additional substrate temperature measurement techniques the optimization of the substrate and desorption temperature will be a very demanding task.

In comparison to the growth of (In,Ga)As on InP(111)A, the needed III/V ratio for optimal growth conditions is very much reduced. This can be explained by the increased As sticking probability on the (111)B surface due to the increased number of dangling bonds of the terminating In and Ga atoms.

### 8.3.2 Growth of NiMnSb on InP(111)B

The NiMnSb growth on InP(111)B substrates follows the same principles as described in section 8.2.2. Directly after the growth of the (In,Ga)As buffer, the sample is transferred into the NiMnSb chamber and heated to the growth temperature of 250°C as measured by the thermocouple behind the molybdenum-

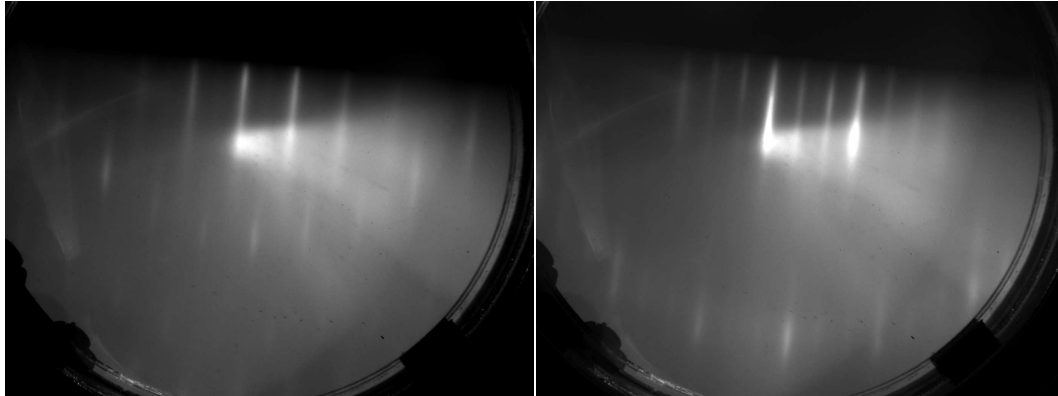


Figure 8.19: RHEED pattern of a 10 nm thick NiMnSb layer on (In,Ga)As/InP(111)B along  $[1\bar{1}0]$ (left) and  $[11\bar{2}]$ (right). The reconstruction shows a flat surface indicated by long main streaks with no sign of transmission RHEED. In both directions the second order streaks are easily to identify. Whereas the  $d/3$  streaks along  $[11\bar{2}]$  are quite strong, the  $d/2$  streaks along the same direction are weaker. The streaks directly next to the main streaks are not visible.

block. As described earlier, to have stable fluxes from the three material cells, the shutters of these cells are opened three minutes in advance before initiating the growth by opening the main shutter. The flux ratios are set to the optimum values determined for the growth on (001) oriented substrates, Sb/Ni to 10.0 and Mn/Ni to 3.0. Directly after the growth start an unreconstructed RHEED pattern is observed which changes after a growth of 4 nm into a (2x2) reconstructed pattern along  $[1\bar{1}0]$  and a (6x6) reconstruction along  $[11\bar{2}]$  (Fig. 8.19).

The specular spot is sharp and clear up to a thickness of 8 nm, then the spot gets more diffuse and an increased surface roughening is observed. This is probably caused by the beginning of the relaxation process. After 20 nm the (2x2) and (6x6) reconstructed surface changes into a (3x3) reconstruction along  $[11\bar{2}]$ . This is the same behavior as observed for the growth of NiMnSb on InP(111)A. This reconstruction does not change for the rest of the growth, as tested for layers up to a thickness of 200 nm. An increased surface roughening as compared to the (In,Ga)As buffer layer cannot be observed, the same behavior as already observed for the growth of NiMnSb on InP(111)A.

## 8.4 Structural Properties

### 8.4.1 Structural Properties of NiMnSb(111)A

As already mentioned in section 8.2.2 indications of relaxation during the growth of NiMnSb on InP(111)A are observed by RHEED measurements. HRXRD experiments confirm this observation.

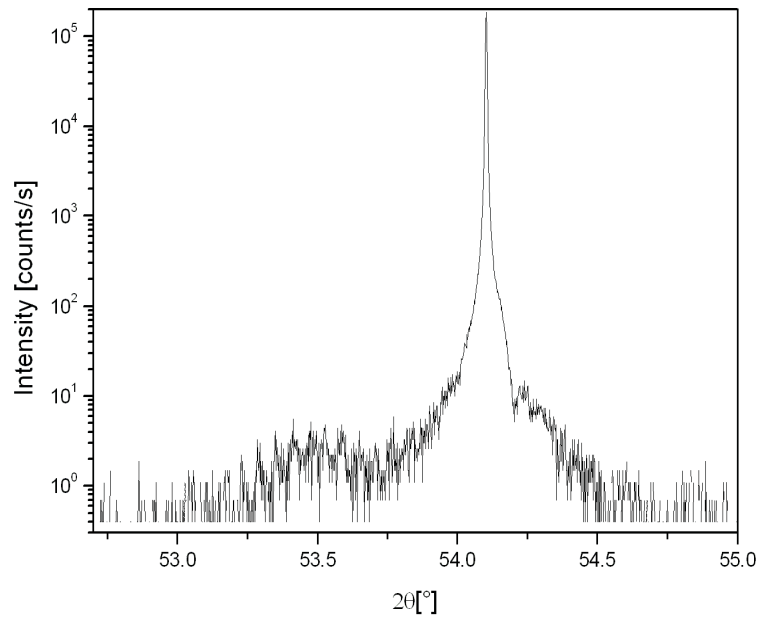


Figure 8.20: HRXRD  $\theta - 2\theta$ -scan of the (222) reflection of a sample consisting of NiMnSb/(In,Ga)As/InP(111)A. The thicknesses of NiMnSb and (In,Ga)As layers are 40 nm and 162 nm, respectively. The (In,Ga)As layer is very good lattice matched to the InP substrate, their peaks cannot be distinguished. Thickness fringes of the (In,Ga)As layer can be easily identified, but not of the NiMnSb layer. This indicates that the NiMnSb layer is at least partly relaxed, whereas the (In,Ga)As layer is totally strained.

Fig. 8.20 shows a HRXRD  $\theta - 2\theta$ -scan of the (222) reflection of a sample with a 40 nm NiMnSb layer on top of a 162 nm (In,Ga)As buffer. Thickness fringes with the spacing corresponding to a thickness of  $\approx 160$  nm indicate that the (In,Ga)As buffer layer is totally strained and shows no relaxation. Thickness fringes which would correspond to the NiMnSb layer, on the other hand, can not be identified. One might argue that the intensity expected from such fringes would be very low, so that thickness fringes of the NiMnSb layer would be very hard to measure. Therefore the absence of thickness fringes for the NiMnSb layer is not

sufficient to identify relaxation in this layer. Here the  $\omega$ -FWHM of the three different materials give more insight on this subject. Whereas the  $\omega$ -FWHM of the (222) reflection of the substrate is in the range of 10 to 15 arcsec, the  $\omega$ -FWHM of the NiMnSb is at least an order of magnitude higher. The FWHM of the (In,Ga)As layer cannot be determined due to the close lattice matching to InP. This shows an increased mosaicity in the NiMnSb layer, pointing to the fact that indeed relaxation occurred during the growth of this layer. To be absolutely certain, a reciprocal space map of an asymmetric reflection would have to be measured. Since the alignment of an asymmetric reflection of a miscut substrate in the diffractometer is a very daunting task, measurements of reciprocal space maps on (111) oriented substrates were not successful so far.

#### 8.4.2 Structural Properties of NiMnSb(111)B

For the samples grown on (111)B oriented substrates the same principles as for the samples on (111)A oriented substrates apply. Also in this case RHEED observations indicate relaxation occurring during the growth of the NiMnSb layer. HRXRD measurements of the (222) reflection of a 40 nm thick NiMnSb layer on top of a 160 nm thick (In,Ga)As buffer confirm this observation (Fig. 8.21). Whereas the (In,Ga)As layer shows thickness fringes indicating that this layer is totally strained, the fringes are missing for the NiMnSb. Together with the fact, that the  $\omega$ -FWHM of the NiMnSb is drastically larger than the one of the InP substrate, this is a strong sign that the NiMnSb layer is at least partly relaxed, whereas the (In,Ga)As layer is totally strained.

The growth of NiMnSb on InP(111) substrates also provides the opportunity to check for binary inclusions of for example NiSb or MnSb inside the NiMnSb layer. The binary compounds of this type typically crystallize in a hexagonal crystal structure with their [0001] axis along the [111] axis of NiMnSb [Roy02]. Therefore an XRD scan of a symmetric reflection is able to pick up signals caused by these inclusions. The lattice constants of MnSb are  $a=4.13 \text{ \AA}$  and  $c=5.79 \text{ \AA}$ . The constants of NiSb are  $a=3.93 \text{ \AA}$  and  $c=5.13 \text{ \AA}$ . To test the basic experiment principle, a sample with intentionally off-stoichiometric composition was grown. The Sb content is increased by 25% in comparison to the stoichiometric samples.

Fig. 8.22 shows the  $\theta - 2\theta$ -scan ranging from the (111) to the (222) InP reflection of a sample with  $\approx 200 \text{ nm}$  thick off-stoichiometric NiMnSb. Apart from the expected InP and NiMnSb signals an additional signal, which can be attributed to MnSb inclusions, is visible. The same measurement performed on a sample with stoichiometric NiMnSb did not show the MnSb signal, indicating that these inclusions are absent in our stoichiometric samples (Fig. 8.23).

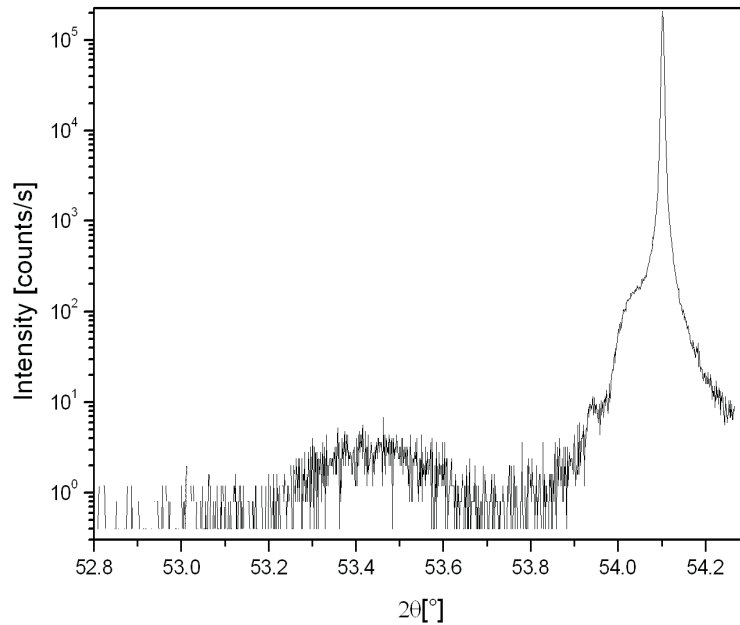


Figure 8.21: HRXRD  $\theta - 2\theta$ -scan of the (222) reflection of a sample consisting of NiMnSb/(In,Ga)As/InP(111)B. The thickness of NiMnSb is 40 nm, of the (In,Ga)As layer 170 nm. The (In,Ga)As layer shows close lattice matching to the InP substrate, the peak of the (In,Ga)As layer lies almost in the one of the InP substrate. Thickness fringes of the (In,Ga)As layer can be identified, but are not as clear as for the growth on InP(111)A. Thickness fringes of the NiMnSb layer cannot be detected. This indicates that the NiMnSb layer is at least partly relaxed, whereas the (In,Ga)As layer is totally strained.

## 8.5 Magnetic Properties

In contrast to the symmetries occurring in (001) oriented NiMnSb layers, (111) oriented layers have a  $120^\circ$  rotational symmetry. Furthermore, the cleaving edges of these crystals are only the symmetrically equivalent  $[10\bar{1}]$ ,  $[1\bar{1}0]$  and  $[01\bar{1}]$ . The symmetrically different  $\langle 110 \rangle$  planes, which are cleaving edges for the (001) oriented crystals, do not lie perpendicular to the surface of the (111) oriented samples. However, since for growth reasons the substrates have a slight misalignment of the surface in the  $[1\bar{1}0]$  or  $[11\bar{2}]$  direction, the rotational symmetry of these layers is broken and a preferential direction along the miscut of the sample is introduced.



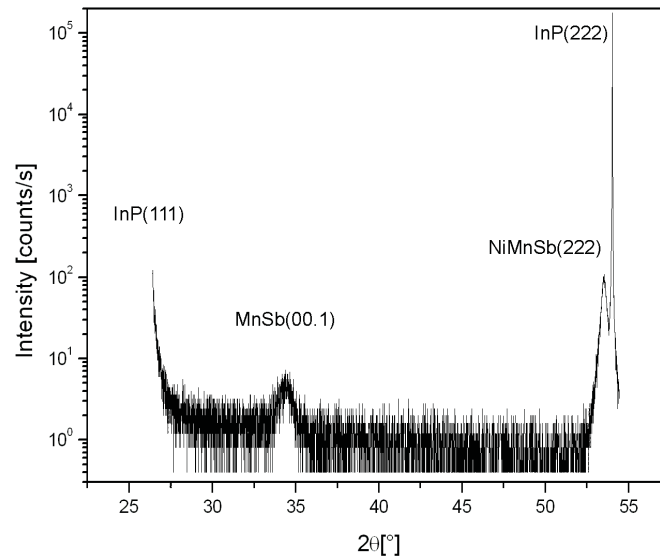


Figure 8.22: HRXRD  $\theta - 2\theta$ -scan of a 200 nm thick off-stoichiometric sample ranging from the InP(111) to the (222) reflection. The different peaks are marked in the figure. Apart from the InP and NiMnSb peaks, an additional MnSb peak can be identified, which was produced by the excess of Sb during growth.

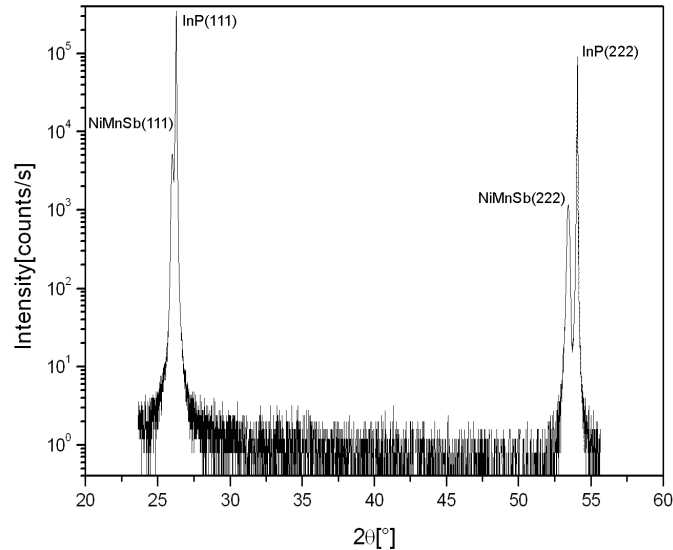


Figure 8.23: HRXRD  $\theta - 2\theta$ -scan of a 200 nm thick stoichiometric sample ranging from the NiMnSb(111) to the InP(222) reflection. The different peaks are marked in the figure. Apart from the InP and NiMnSb peaks, no additional peaks can be identified in contrast to Fig. 8.22, indicating the absence of MnSb inclusions in these layers.

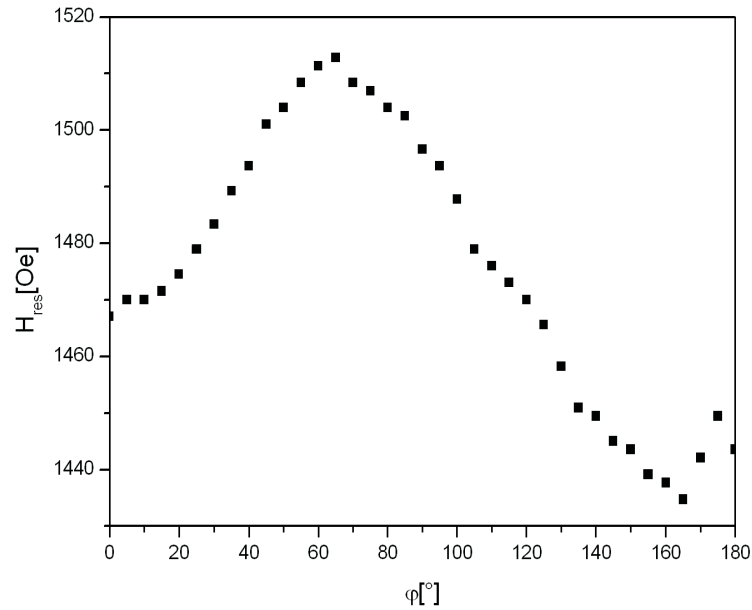


Figure 8.24: Angular dependence of the FMR line position at 10.368 GHz for a sample with 40 nm NiMnSb grown on InP(111)A. The angle  $\varphi$  is in direction of the applied field with respect to the  $[1\bar{1}0]$  axis of NiMnSb.

### 8.5.1 Magnetic Properties of NiMnSb(111)A

The magnetic anisotropy of NiMnSb grown on InP(111)A was determined by FMR measurements. Fig. 8.24 shows the data obtained for a 40 nm thick NiMnSb layer grown on an InP(111)A oriented sample with a  $2^\circ$  miscut along  $[11\bar{2}]$ . The FMR measurement shows a clear uniaxial anisotropy with the easy axis along  $\varphi = 150^\circ$ , which corresponds to the  $[11\bar{2}]$  axis. No three-fold anisotropy can be determined which would be caused by the  $120^\circ$  symmetry of the crystal lattice. Apparently the miscut of the substrate causes one crystallographic axis to be preferred by the magnetic field.

### 8.5.2 Magnetic Properties of NiMnSb(111)B

To obtain the magnetic anisotropies of NiMnSb grown on InP(111)B FMR measurements were performed. Figs. 8.25 and 8.26 show the FMR data of samples with 40 nm thick NiMnSb layers. For both samples a clear uniaxial anisotropy can be determined. The NiMnSb layers of both samples have the same thickness and the same underlying (In,Ga)As layer, however, the easy axis for the first sample is along  $\varphi = 60^\circ$ , which corresponds to the  $[1\bar{1}0]$  direction, whereas the easy axis for the second sample is along  $\varphi = 150^\circ$  which corresponds to the  $[11\bar{2}]$  di-

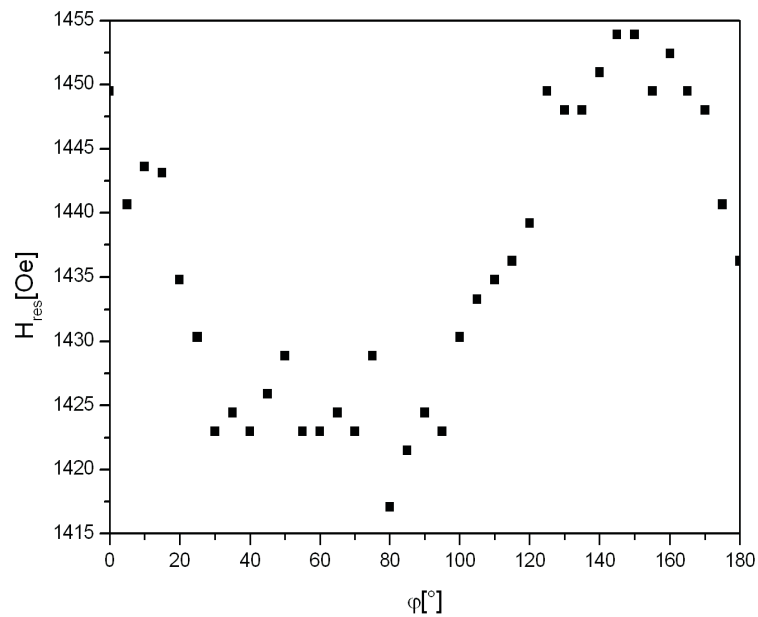


Figure 8.25: Angular dependence of the FMR line position at 10.368 GHz for a sample with 40 nm NiMnSb grown on InP(111)B. The InP substrate was miscut by  $1^\circ$  along  $[1\bar{1}0]$ . The angle  $\varphi$  is in direction of the applied field with respect to the  $[1\bar{1}0]$  axis of NiMnSb.

rection. The easy axis of the two NiMnSb films are exactly perpendicular to each other. Whereas both samples have exactly the same composition, the substrates used for these samples show a characteristic difference. The substrate used for the sample shown in Fig. 8.25 has a miscut along of  $1^\circ$  along  $[1\bar{1}0]$ , whereas the sample shown in Fig. 8.26 has a miscut of  $2^\circ$  along  $[11\bar{2}]$ . The two samples only differ in the miscut of the substrates used for the growth and the miscut of the substrate is in both cases exactly parallel to the observed easy axis. Also in the case of NiMnSb grown on InP(111)A, the easy axis of a 40 nm thick layer is exactly parallel to the miscut of the substrate (see section 8.5.1). Therefore the magnetic anisotropy is dominated by the symmetry breaking of the miscut and hence by the formation of a preferential direction in these samples.

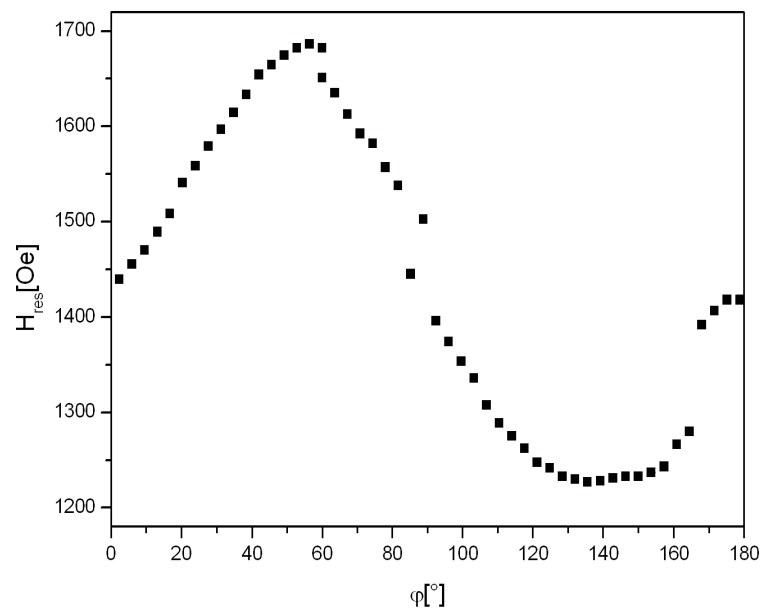


Figure 8.26: Angular dependence of the FMR line position at 10.368 GHz for a sample with 40 nm NiMnSb grown on InP(111)B. The InP substrate was miscut by  $2^\circ$  along  $[11\bar{2}]$ . The angle  $\varphi$  is in direction of the applied field with respect to the  $[1\bar{1}0]$  axis of NiMnSb.

# Summary

In this work heterostructures based on the half-Heusler alloy NiMnSb have been fabricated and characterized. NiMnSb is a member of the half-metallic ferromagnets, which exhibit an electron spin-polarization of 100% at the Fermi-level.

For fabrication of these structures InP substrates with surface orientations of (001), (111)A and (111)B have been used. The small lattice mismatch of NiMnSb to InP allows for pseudomorphic layers, the (111) orientation additionally makes the formation of a half-metallic interface possible.

For the growth on InP(001), procedures for the substrate preparation, growth of the lattice matched (In,Ga)As buffer layer and of the NiMnSb layer have been developed. The effect of flux-ratios and substrate temperatures on the MBE-growth of the buffer as well as of the NiMnSb layer have been investigated and the optimum conditions have been pointed out. NiMnSb grows in the layer-by-layer Frank-van der Merwe growth mode, which can be seen by the intensity oscillations of the RHEED specular spot during growth. RHEED and LEED measurements show a flat surface and a well-defined surface reconstruction. High resolution x-ray measurements support this statement, additionally they show a high crystalline quality.

Measurements of the lateral and the vertical lattice constant of NiMnSb films on (001) oriented substrates show that layers above a thickness of 20 nm exhibit a pseudomorphic as well as a relaxed part in the same layer. Whereas layers around 40 nm show partly relaxed partitions, these partitions are totally relaxed for layers above 100 nm. However, even these layers still have a pseudomorphic part. Depth-dependent x-ray diffraction experiments prove that the relaxed part of the samples is always on top of the pseudomorphic part.

The formation and propagation of defects in these layers has been investigated by TEM. The defects nucleate early during growth and spread until they form a defect network at a thickness of about 40 nm. These defects are not typical misfit dislocations but rather antiphase boundaries which evolve in the Mn/Sb sublattice of the NiMnSb system.

Dependent on the thickness of the NiMnSb films different magnetic anisotropies can be found. For layers up to 15 nm and above 25 nm a clear uni-

axial anisotropy can be determined, while the layers with thicknesses in between show a fourfold anisotropy. Notably the easy axis for the thin layers is perpendicular to the easy axis observed for the thick layers. Thin NiMnSb layers show a very good magnetic homogeneity, as can be seen by the very small FMR linewidth of 20 Oe at 24 GHz. However, the increase of the linewidth with increasing thickness shows that the extrinsic damping gets larger for thicker samples which is a clear indication for magnetic inhomogeneities introduced by crystalline defects. Also, the magnetic moment of thick NiMnSb is reduced compared to the theoretically expected value. If an antiferromagnetic material is deposited on top of the NiMnSb, a clear exchange biasing of the NiMnSb layer can be observed.

In a further step the epitaxial layers of the semiconductor ZnTe have been grown on these NiMnSb layers, which enables the fabrication of NiMnSb/ZnTe/NiMnSb TMR structures. These heterostructures are single-crystalline and exhibit a low surface and interface roughness as measured by x-ray reflectivity. Magnetic measurements of the hysteresis curves prove that both NiMnSb layers in these heterostructures can switch separately, which is a necessary requirement for TMR applications. If a NiMn antiferromagnet is deposited on top of this structure, the upper NiMnSb layer is exchange biased by the antiferromagnet, while the lower one is left unaffected.

Furthermore the growth of NiMnSb on (111) oriented substrates has been investigated. For these experiments, InP substrates with a surface orientation of (111)A and (111)B were used, which were miscut by 1 to 2° from the exact orientation to allow for smoother surfaces during growth. Both the (In,Ga)As buffer as well as the NiMnSb layer show well defined surface reconstructions during growth. X-ray diffraction experiments prove the single crystalline structure of the samples. However, neither for the growth on (111)A nor on (111)B a perfectly smooth surface could be obtained during growth, which can be attributed to the formation of pyramid-like facets evolving as a result of the atomic configuration at the surface. A similar relaxation behavior as NiMnSb layers on (001) oriented InP could not be observed. RHEED and x-ray diffraction measurements show that above a thickness of about 10 nm the NiMnSb layer begins to relax, but remnants of pseudomorphic parts could not be found.

Magnetic measurements show that the misorientation of the substrate crystal has a strong influence on the magnetic anisotropies of NiMnSb(111) samples. In all cases a uniaxial anisotropy could be observed. The easy axis is always aligned parallel to the direction of the miscut of the substrate.

# Zusammenfassung

Im Rahmen dieser Arbeit wurden Heterostrukturen basierend auf dem Halb-Heusler Material NiMnSb hergestellt und charakterisiert. NiMnSb ist ein Mitglied der halbmetallischen Ferromagnete, die sich durch eine 100% Spinpolarisation an der Fermikante auszeichnen.

Zur Herstellung der Strukturen wurden InP Substrate der Orientierungen (001), (111)A und (111) B verwendet. Die geringe Gitterfehlانpassung von NiMnSb an InP erlaubt pseudomorphe Strukturen, die (111) Orientierung ermöglicht zusätzlich die Entstehung eines halb-metallischen Interfaces.

Für das Wachstum auf InP(001) wurden Prozeduren für die Substratvorbereitung, die Herstellung des gitterangepassten (In,Ga)As und des NiMnSb entwickelt. Sowohl der Einfluss der Flussverhältnisse als auch der Substrattemperatur wurden erforscht und die optimalen Parameter ermittelt. NiMnSb wächst im Frank-van der Merwe Modus, der sich durch Oszillationen des Spekularreflexes bei RHEED Messungen auszeichnet.

Untersuchungen der Oberfläche mittels LEED zeigen eine wohldefinierte Rekonstruktion sowie eine niedrige Oberflächenrauigkeit. Hochauflösende Röntgenbeugungsexperimente unterstützen diese Aussage, zusätzliche zeigen sie eine hohe kristalline Qualität der Schichten.

Messungen der NiMnSb Gitterkonstante in lateraler sowie vertikaler Richtung zeigen, dass in allen Schichten dicker als 20 nm sowohl pseudomorphe als auch relaxierte Teilbereiche existieren. Während Schichten um 40 nm teilrelaxierte Bereiche aufweisen, sind diese Bereiche bei Schichten über 100 nm vollständig relaxiert. Tiefenabhängige Röntgenbeugungsexperimente beweisen, dass der relaxierte Teil der NiMnSb Schicht immer über dem pseudomorphen Teil liegt.

Die Ausbreitung von Kristalldefekten wurde durch TEM untersucht. Dabei zeigte sich, dass diese Defekte schon sehr bald während des Wachstums entstehen und sich immer weiter ausbreiten, bis sie bei einer Dicke von etwa 40 nm überlappen. Bei diesen Defekten handelt es sich nicht um typische Versetzungen, die aufgrund der Gitterfehlانpassung entstehen, sondern sehr wahrscheinlich um Antiphasen Grenzen die sich im Mn/Sb Untergitter des NiMnSb ausbilden.

Zusätzlich zur hohen kristallinen Qualität der NiMnSb Schichten zeigen auch

magnetische Messungen eine hohe Homogenität. Die Curie-Temperatur liegt erwartungsgemäß weit über Raumtemperatur. Die Schichten zeigen verschiedene Anisotropien abhängig von der Dicke der Schicht, uniaxiale Anisotropien wurden für Schichten dünner als 15 bzw. dicker als 25 nm beobachtet, dazwischen bildet sich eine Vierfach-Anisotropie aus. Mit steigender Dicke konnte auch eine Abnahme der magnetischen Homogenität beobachtet werden, was auf die Zunahme der Defektdichte bei dickeren Schichten zurückgeführt werden kann. Scheidet man auf dem NiMnSb-Ferromagneten einen Antiferromagneten bestehend aus NiMn ab, so kann der „Exchange Bias“ Effekt beobachtet werden.

Auf diese NiMnSb Schichten wurde in einem weiteren Schritt der Halbleiter ZnTe epitaktisch gewachsen, wodurch die Herstellung von NiMnSb/ZnTe/NiMnSb TMR Strukturen ermöglicht wurde. Diese Schichten sind einkristallin und zeichnen sich durch kleine Oberflächen- und Grenzflächenrauhigkeiten aus. Magnetische Messungen dieser Heterostrukturen zeigen, dass beide ferromagnetische Schichten separat schalten können, eine der Grundvoraussetzung für die Beobachtung des TMR Effekts. Bringt man auf diese Strukturen einen Antiferromagneten auf, so kann eine „Exchange Bias“ Wechselwirkung mit der oberen NiMnSb-Schicht beobachtet werden, während die untere unbeeinträchtigt bleibt.

In einem weiteren Teil der Arbeit wurde das Wachstum von NiMnSb auf (111) orientierten Substraten untersucht. Dazu wurden InP Kristalle der Orientierung (111)A und (111)B verwendet, die um 1-2° von der exakten Orientierung abweichen, um ein glatteres Wachstum zu ermöglichen. Sowohl die (In,Ga)As als auch NiMnSb-Schichten zeigen wohldefinierte Rekonstruktionen während des Wachstums. Röntgenbeugungsexperimente zeigen die einkristalline Struktur der Proben. Weder für das Wachstum auf InP(111)A noch auf InP(111)B konnte jedoch perfekt glatte Oberflächen während des Wachstums erzielt werden, was auf die Entstehung von pyramidenartigen Facetten aufgrund der Atomkonfiguration an der (111) Oberfläche zurückgeführt werden kann. Ein ähnliches Relaxationsverhalten wie für NiMnSb Schichten auf InP(001) konnte nicht beobachtet werden. Schichten oberhalb einer Dicke von ca. 10 nm beginnen während des Wachstums komplett zu relaxieren, was durch RHEED und Röntgenbeugungsexperimente belegt wurde.

Magnetische Messungen ergaben, dass sich die Fehlorientierung der Substratkristalle stark auf das Anisotropieverhalten der NiMnSb(111) Proben auswirkt. In allen Fällen konnte eine uniaxiale Anisotropie beobachtet werden, die sich jeweils senkrecht zur Richtung der Fehlorientierung befindet.



# Appendix A

## Material Constants

### A.1 Atomic Scattering Factors

Material	$f_1$	$f_2$
Ga	29.712	0.80186
In	49.137	4.95604
P	15.303	0.43624
As	32.054	1.04595
Ni	25.003	0.52402
Mn	24.462	2.83205
Sb	50.985	5.66370

Table A.1: Atomic scattering factors  $f = f_1 + if_2$  for the Cu- $K_\alpha$ -wavelength (1.54056 Å) for the elements used in this work (from [Hen93])

## A.2 Lattice Constants

Material	$a_0/\text{\AA}$
GaAs	5.65325
InP	5.8687
InAs	6.0584
ZnSe	5.668
CdSe	6.052
BeTe	5.6269
ZnTe	6.100
NiMnSb	5.903

Table A.2: Lattice constants of the materials used in this work.

# Bibliography

- [Bar97] V.G. Bar'yakhtar, P.E. Wigen, and N.A. Lesnik, editors. *Frontiers in Magnetism of Reduced Dimension Systems*. NATO ASI Series. Kluwer Academic Publishers, Dodrecht, The Netherlands, 1997. Chapter V.
- [Ben01] L.A. Bendersky and F.W. Gayle. *J. Res. Natl. Inst. Stand. Technol.*, 106:997–1012, 2001.
- [Blu01] Stephen Blundell. *Magnetism in Condensed Matter*. Oxford Master Series in Condensed Matter Physics. Oxford University Press, New York, USA, 2001.
- [Bon85] G.L. Bona, F. Meier, M. Taborelli, E. Bucher, and P.H. Schmidt. *Solid State Commun.*, 56:391, 1985.
- [Bra99] W. Braun. *Applied RHEED, Reflection High-Energy Diffraction During Crystal Growth*, volume 154 of *Springer Tracts in Modern Physics*. Springer-Verlag, Berlin, 1999.
- [Cab97] J.A. Caballero, P.D. Park, A. Cabbibo, J.R. Childress, F. Petroff, and R. Morel. *J. Appl. Phys.*, 81:2740, 1997.
- [Cas55] L. Castelliz. *Z. Metallkd.*, 46:201, 1955.
- [Coh02] D. Cohen and C. B. Carter. *J. Microscopy*, 208:84, 2002.
- [Cra95] D. Craik. *Magnetism: Principles and Applications*. John Wiley & Sons Ltd., West Sussex, England, 1995.
- [dG83] R.A. de Groot, F.M. Mueller, P.G. van Engen, and K.H.J. Buschow. *Phys. Rev. Lett.*, 50:2024, 1983.
- [dG03] Marc de Graef. *Introduction to Conventional Transmission Electron Microscopy*. Cambridge University Press, Cambridge, UK, 2003.
- [Dow90] P.A. Dowben and A. Miller, editors. *Surface Segregation Phenomena*. CRC Press, Boston, USA, 1990.

- [Dun91] D.J. Dunstan, S. Young, and R.H. Dixon. *J. Appl. Phys.*, 70:3038–3045, 1991.
- [dW01] G.A. de Wijs and R.A. de Groot. *Phys. Rev. B*, 64:020402(R), 2001.
- [Few87] P.F. Fewster and C.J. Curling. *J. Appl. Phys.*, 62:4154–4158, 1987.
- [Fra80] Z. Frait and D. Fraitova. *J. Magn. Magn. Mater.*, 15-18:1081, 1980.
- [Gil55] T.L. Gilbert. *Phys. Rev.*, 100:1243, 1955.
- [Gol98] R. S. Goldman, K.L. Kavanagh, H.H. Wieder, S.N. Ehrlich, and R.M. Feenstra. *J. Appl. Phys.*, 83:5137, 1998.
- [Han86] K.E.H.M. Hanssen and P.E. Mijnaarend. *Phys. Rev. B*, 34:5009, 1986.
- [Han90] K.E.H.M. Hanssen, P.E. Mijnaarends, L.P.L.M. Rabou, and K.H.J. Buschow. *Phys. Rev. B*, 42:1533, 1990.
- [Hei88] B. Heinrich, S. Purcell, J. Dutcher, K. B. Urquhart, J. F. Cochran, and A. S. Arrott. *Phys. Rev. B*, 38:12879, 1988.
- [Hei93] B. Heinrich and J. F. Jochain. *Advances in Physics*, 42:523, 1993.
- [Hei02] B. Heinrich, R. Urban, and G. Woltersdorf. *J. Appl. Phys.*, 91:7523, 2002.
- [Hen93] B.L. Henke, E.M. Gullikson, and J.C. Davis. *Atomic Data and Nuclear Data Tables*, 54:181–342, 1993.
- [Her96] M. A. Herman and H. Sitter. *Molecular Beam Epitaxy, fundamentals and current status*, volume 7 of *Springer series in material science*. Springer-Verlag, Berlin, 1996.
- [Her03] J. Herfort, H. Schönherr, and K. H. Ploog. *Appl. Phys. Lett.*, 83:3912, 2003.
- [Hir77] P. Hirsch, A. Howie, R. Nicholson, D. W. Pashley, and M. J. Whelan. *Electron Microscopy of Thin Films*. 2nd Ed. R. E. Krieger Publishing Co., Florida, US, 1977.
- [Hol99] V. Holý, U. Pietsch, and T. Baumbach. *High resolution x-ray scattering from thin films and multilayers*. Springer-Verlag, Berlin, 1999.
- [Hor96] C. Hordequin, J. Pierre, and R. Currat. *J. Magn. Magn. Mater.*, 162:75–84, 1996.
- [Hor99] M. Horn von Hoegen. *Z. Kristallogr.*, 214(11):684–721, 1999.

- [Hou00] C. Hou, H. Fujiwara, K. Zhang, A. Tanaka, and Y. Shimizu. *Phys. Rev. B*, 63:024411, 2000.
- [Kit96] Ch. Kittel. *Einführung in die Festkörperphysik*. 11. Auflage. Oldenbourg Verlag, München, 1996.
- [Kom94] Ph. Komninou, J. Stoemenos, G. P. Dimitrakopoulos, and Th. Karakostas. *J. Appl. Phys.*, 75:143, 1994.
- [Man99] F. B. Mancoff, B. M. Clemens, E. J. Singley, and D. N. Basov. *Phys. Rev. B*, 60:R12565, 1999.
- [Mao98] S. Mao, N. Amin, and E. Murdock. *J. Appl. Phys.*, 83:6807–6809, 1998.
- [Mat74] J. W. Matthews and A. E. Blakeslee. *J. Cryst. Growth*, 27:118, 1974.
- [Mei56] W. H. Meiklejohn and C. P. Bean. *Phys. Rev.*, 102:1413, 1956.
- [Neu97] H. Neureiter, S. Spranger, M. Schneider, U. Winkler, M. Sokolowski, and E. Umbach. *Surface Science*, 388:186, 1997.
- [Nog99] J. Nogue´s and I. K. Schuller. *J. Magn. Magn. Mater.*, 192:203, 1999.
- [Ott89] M.J. Otto, R.A.M. van Woerden, P.J. van der Valk, J. Wijngaard, C.F. van Bruggen, C. Haas, and K.H.J. Buschow. *J. Phys. Condens. Matter*, 1:2341, 1989.
- [Oug00] H. Oughaddou, S. Sawaya, J. Goniakowski, B. Aufray, G. Le Lay, J.M. Gay, G. Trégliá, J.P. Bibérian, N. Barret, C. Guillot, A. Mayne, and G. Du-jardin. *Phys. Rev. B*, 62:166533, 2000.
- [Reß98] H. Reß. *Dissertation, Uni Würzburg*, 1998.
- [Ris00] D. Ristoiu, J.P. Nozieres, C.N. Borca, B. Borca, and P.A. Dowben. *Appl. Phys. Lett.*, 76:2349, 2000.
- [Roy00] W. Van Roy, J. De Boeck, B. Brijs, and G. Borghs. *Appl. Phys. Lett.*, 77:4190, 2000.
- [Roy02] W. Van Roy, G. Borghs, and J. De Boeck. *J. Mag. Mag. Mat.*, 242:489, 2002.
- [Sch00] G. Schmidt, L.W. Molenkamp, A. T. Filip, and B. J. van Wees. *Phys. Rev. B*, 62:R4790, 2000.
- [Sly93] E.E. Slyadnikov. *Phys. Solid State*, 35:530–532, 1993.

- [Sou98] R.J. Soulen, Jr., J.M. Byers, M.S. Osofsky, B. Nadgorny, T. Ambrose, S.F. Cheng, P.R. Broussard, C.T. Tanaka, J. Nowak, J.S. Moodera, A. Barry, and J.M.D. Coey. *Science*, 282:85, 1998.
- [Sti] A. Stierle. The FEWLAY code can be obtained from A. Stierle (e-mail address: stierle@mf.mpg.de).
- [Tan99] C.T. Tanaka, J. Nowak, and J.S. Moodera. *J. Appl. Phys.*, 86:6239, 1999.
- [Tho03] O. Thomas, Q. Shen, O. Schieffer, , and P. Lepine. *Phys. Rev. Lett.*, 90:017205, 2003.
- [Tom96] P. Tomasini, A. Haidoux, M. Maurin, and J.C. Tedenac. *J. Cryst. Growth*, 166:590, 1996.
- [Tou99] E. Tournie, V. Bousquet, and J.-P. Faurie. *J. Cryst. Growth*, 201/202:494, 1999.
- [Tur02] P. Turban, S. Andrieu, , B. Kierren, E. Snoeck, C. Teodorescu, and A. Traverse. *Phys. Rev. B*, 65:134417, 2002.
- [vD81] T. van Duzer and C.W. Turner. *Principles of superconductive devices and circuits*. Elsevier, New York, USA, 1981.
- [VEE96] VEECO. Application note 2/96, 1996.
- [Von49] S.V. Vonsovskii and N.V. Sokolov. *J. Exper. Theor. Phys. USSR*, 19:703, 1949.
- [Xu00] Y.B. Xu, J. Freeland, M. Tselepi, and J. A. C. Bland. *Phys. Rev. Lett.*, 62:1167, 2000.
- [Zha87] J. Zhang, J. Neave, P.J. Dobson, and B.A. Joyce. *Appl. Phys. A*, 42:317, 1987.

# Liste eigener Veröffentlichungen

- [1] J. Liu, E. Girgis, P. Bach, C. Rüster, C. Gould, G. Schmidt and L. W. Molenkamp, *Tunneling magnetoresistance in devices based on epitaxial NiMnSb with uniaxial anisotropy*, J. Appl. Phys., **99**, 036110 (2006).
- [2] A. Koveshnikov, G. Woltersdorf, J. Q. Liu, B. Kardasz, O. Mosendz, B. Heinrich, K. L. Kavanagh, P. Bach, A. S. Bader, C. Schumacher, C. Rüster, C. Gould, G. Schmidt, L. W. Molenkamp and C. Kumpf, *Structural and magnetic properties of NiMnSb/InGaAs/InP(001)*, J. Appl. Phys., **97**, 073906 (2005).
- [3] E. Girgis, P. Bach, C. Rüster, C. Gould, G. Schmidt and L.W. Molenkamp, *Giant magnetoresistance in an epitaxial NiMnSb/Cu/CoFe multilayer*, Appl. Phys. Lett., **86**, 142503 (2005).
- [4] L. Nowicki, A.M. Abdul-Kader, P. Bach, G. Schmidt, L.W. Molenkamp, A. Turos and G. Karczewski, *Structural characterization of half-metallic Heusler compound NiMnSb* Nucl. Instr. and Meth. B, **219**, 666 (2004).
- [5] B. Heinrich, G. Woltersdorf, R. Urban, O. Mosendz, G. Schmidt, P. Bach, L.W. Molenkamp and E. Rozenberg, *Magnetic properties of NiMnSb(001) films grown on InGaAs/InP(001)*, J. Appl. Phys., **95**, 7462 (2004).
- [6] W. Weigand, A. Müller, L. Kilian, T. Schallenberg, P. Bach, G. Schmidt, L.W. Molenkamp, O. Bunk, R.L. Johnson, C. Kumpf and E. Umbach, *Structural investigation of the ZnSe(001)-c(2x2) surface*, Phys. Rev. B, **68**, 241314 (2003).
- [7] P. Bach, A.S. Bader, C. Rüster, C. Gould, C.R. Becker, G. Schmidt, L.W. Molenkamp, W. Weigand, C. Kumpf, E. Umbach, R. Urban, G. Woltersdorf and B. Heinrich, *Molecular-beam epitaxy of the half-Heusler alloy NiMnSb on (In,Ga)As/InP (001)*, Appl. Phys. Lett., **83**, 521 (2003).
- [8] P. Bach, C. Rüster, C. Gould, C.R. Becker, G. Schmidt and L.W. Molenkamp, *Growth of the half-Heusler alloy NiMnSb on (In,Ga)As/InP by molecular beam epitaxy*, J. Cryst. Growth, **251**, 323 (2003).





# Lebenslauf

Name	Peter Bach
Geburtsdatum	10.05.1976 in Tauberbischofsheim
Schulausbildung	1982 - 1986 Grundschule Großrinderfeld 1986 - 1995 Matthias-Grünwald-Gymnasium Tauberbischofsheim
Grundwehrdienst	1995 - 1996 PzBtl 363 in Kilsheim
Studium	1996 - 1999 Studium der Physik an der Bayerischen Julius-Maximilians-Universität 1999 - 2000 Studium der Physik an der University of Texas at Austin
Promotion	2001 - 2005 Bayerische Julius-Maximilians-Universität Würzburg, Physikalisches Institut, Lehrstuhl Experimentelle Physik 3, Professor Molenkamp
Berufstätigkeit	Seit Nov. 2005 Angestellt als Physiker bei der Robert Bosch GmbH Reutlingen



# Danksagung

An erster Stelle möchte ich mich bei Prof. Dr. L.W. Molenkamp bedanken, der es mir ermöglichte, diese Dissertation an seinem Lehrstuhl anzufertigen.

Ein besonderer Dank geht an PD Dr. Georg Schmidt, der nicht nur erste Anlaufstelle bei vielen Problemen war, sondern auch maßgeblich die Richtung dieser Arbeit beeinflusst hat.

Vielen Dank auch an die Leute, die bei vielen in dieser Arbeit beschriebenen Ergebnissen ihre Finger im Spiel hatten: Dr. Charles Gould, Andreas Riegler und Christian Rüster für die magnetischen Untersuchungen meiner Proben sowie Dr. Christian Kumpf, Andreas Stahl und Wolfgang Weigand für GIXRD und SPA-LEED Messungen. Ein besonderes Dankeschön auch an Prof. Dr. Reinhard Neder, der immer wieder bei kristallographischen Fragen bereitwillig geholfen hat.

Bei meinen Kollegen an der MBE, Peter Grabs, Florian Lochner, Taras Slobodskyy, Idris Chado, Manuel Schmidt, Martina Weiß, Lars Hansen, Suddho Mahapatra, Timo Schallenberg und Claus Schumacher möchte ich mich nicht nur für die fachliche Unterstützung sondern auch für die spaßige Arbeit während so mancher schweißtreibenden Stunde im Reinraumanzug bedanken.

Ein großes Dankeschön geht auch an Alfred Schönteich, Rainer Brauner und Volkmar Hock für ihre tatkräftige Unterstützung bei der Wartung und Pflege der MBE, an die Heinzelmännchen der MBE, Anita Gebhard und Petra Wolf-Müller, die Proben schneller präparieren als man sie sich ausdenken kann sowie an Anja Brück-Poirier, die immer wieder durch das bürokratische Dickicht geholfen hat.

Außerdem sei all denen gedankt, die ihren Beitrag dafür geleistet haben, dass das Arbeiten bei EPIII immer viel Spaß gemacht hat: Alena Astakhova, Georgy Astakhov, Armin Bader, Utz Bass, Charlie Becker, Andreas Benkert, Tanja Borzenko, Karl Brunner, Hartmut Buhmann, Bastian Büttner, Volker Daumer, Wolfgang Faschinger, Roland Fiederling, Michael Gbordzoe, Jean Geurts, Ehmat Girgis, Dieter Groß, Greg Karczewski, Dirk Keller, Tobias Kießling, Markus König, Frank Lehmann, Michael Lentze, Michael Leufgen, Jian Liu, Markus

Michelfeit, Tobias Muck, Kai Ortner, Wolfgang Ossau, Katrin Pappert, Georg Richter, Matthias Schäfer, Ralf Scheibner, Gisela Schott, Anatolij Slobodskyy, Rasa Staskunaite, Daniel Supp, Joachim Wagner, Veit Wagner, Jan Wenisch.

Ein ganz besonderer Dank geht an meine Familie und Andrea für ihre beständige Unterstützung während meines Studiums und meiner Promotion.

# Erklärung an Eides statt

*gemäß §5 Abs. 2 Ziff. 2 und 5  
der Promotionsordnung der Fakultät für Physik und Astronomie  
der Julius-Maximilians-Universität Würzburg  
vom 22. September 2003*

Hiermit versichere ich an Eides statt, dass ich die Dissertation eigenständig, d.h. selbständig und ohne Hilfe eines Promotionsberaters angefertigt und keine anderen als die angegebenen Quellen und Hilfsmittel benutzt habe und dass die Dissertationsschrift bisher weder in gleicher noch in anderer Form in einem anderen Prüfungsfach vorgelegen hat.

Würzburg, den 23.02.2006

Peter Bach